2013 (Heisei 25)

Doctoral Thesis

Study on Harmonic Structure Design and Deformation Mechanism in SUS304L Austenitic Stainless Steel

Ritsumeikan University

Graduate School of Science and Engineering

Doctoral Program in Integrated Science and Engineering

ZHANG Zhe

Study on Harmonic Structure Design and Deformation Mechanism in SUS304L Austenitic Stainless Steel

December, 2013

Doctor of Philosophy

Zhe ZHANG

Committee in charge:

Professor Kei AMEYAMA, Chair

Professor Masao SAKANE

Professor Akira UENO

Doctoral Program in Integrated Science and Engineering

Graduate School of Science and Engineering

Ritsumeikan University

Abstract

Study on Harmonic Structure Design and Deformation Mechanism in SUS304L Austenitic Stainless Steel

by

Zhe ZHANG

Doctoral Program in Integrated Science and Engineering

Graduate School of Science and Engineering

Ritsumeikan University

Academic Advisor: Professor Kei AMEYAMA

Owing to the excellent corrosion resistance and oxidation resistance, austenitic stainless steels have been widely used in the chemical and petrochemical industry. However, low yield strength is the major drawback of austenitic stainless steel. Grain refinement is a well known and attractive method of strengthening structural metallic materials. However, ultrafine-grained (UFG) materials are characterized by low tensile ductility at room temperature because of plastic strain instability in the early stage of deformation. Both strength and ductility are the important mechanical properties for industrial applications. Bimodal grain size distribution is a useful strategy to enhance ductility. However, the outcome properties span a relatively wide range depending on the microstructural variations.

Recently, professor Ameyama and co-workers proposed a powder metallurgy (PM) based approach to create a novel bimodal microstructure design called “harmonic structure”. Effectively, harmonic structure is a periodic “nano and heterogeneous bimodal structure” consisting of coarse-grained (CG) areas (or “cores”) enclosed in a three-dimensional continuously connected network of UFG structure (or “shell”). The concept of harmonic structure design has been successfully applied in a variety of pure metals and metallic alloys by mechanical milling (MM) and subsequent powder metallurgy (PM) process. All these materials demonstrate a winning combination of improved strength and ductility as compared to their coarse-grained as well as ultrafine-grained counterparts.

The present dissertation describes the work that has been carried out to obtain a better understanding of the manufacture, mechanical properties, deformation and fracture mechanism of harmonic-structured austenitic stainless steel. Plasma rotating electrode process (PREP) powders, which are characterized by low oxygen content and spherical powder shape, are applied in present work. The harmonic structure has been synthesized in SUS304L stainless steels produced by mechanical milling (MM) and subsequent spark plasma sintering (SPS) process. Martensite transformation and subsequent austenite reversion plays an important role on grain refinement in the SUS304L steels. The volume fraction of UFG can be adjusted by controlling mechanical milling conditions.

Compared to the conventional homogeneous CG and UFG bulks, the harmonic-structured SUS304L steels demonstrate a superior combination of high

strength, large uniform elongation, and large total elongation. Also, the harmonic-structured SUS304L steels exhibit good reproducibility, higher average strength and ductility simultaneously as compared to the steels having same grain size and volume fraction but irregular CG and UFG spatial distribution.

Through comparing the tensile deformation of the specimens having different bimodal structure heterogeneity and topology, it is concluded that the three-dimensional continuous connected network of UFG structure is conducive to restraining strain localization during mechanical loading. The suppressed strain localization leads to postpone the plastic strain instability and delay the neck formation. Therefore, the ductility, in particular uniform elongation in tension of harmonic bimodal structured SUS304L steels is superior to the value of heterogeneous bimodal structured ones. The ductility of bimodal structured materials can be improved by controlling the CG and UFG spatial distribution. “Harmonic structure design” is proposed to be an effective strategy to achieve outstanding mechanical properties.

Since water-atomization is the most common technique for producing low-cost metal powders, water-atomized steel powders have been widely used in industry. Therefore, “harmonic structure design” is also attempted to synthesize in water-atomized SUS304L powder steels. However, owing to the high oxygen content in water-atomized powders, a large amount of SiO_2 particles precipitate in the UFG region of sintered compacts. SiO_2 particles tend to impair the inter-particle bonding and result in poor ductility. Therefore, in order to improve mechanical properties, it is necessary to reduce oxidized contaminations in the PM steels.

Acknowledgements

I would like to take this opportunity to express my most sincere gratitude to Professor Kei Ameyama, who taught and gave me invaluable advice and generous help through these six years at Ritsumeikan University. Although I cannot study in the university at work time, he still helped me apply for doctoral program, gave me supervision in his spare time. I would like to remember his inculcation for clarify the critical logical relation in the research forever. His guidance and encouragement enabled me to become stronger and wiser, in both academic matters and personal growth.

I am grateful to the company, Dainippon Screen MFG. Co., Ltd., who gave me scholarship for the study of master program and provided me the work opportunity in Japan. Special thanks to Mr. Yoshiyuki Nakazawa and Mr. Kazuhiko Asada for their patient guidance for my work in the company and the convenience for my study.

Special thanks to Associate Professor Hiroshi Fujiwara (now in Doshisha University, Kyoto) for his selfless support in texture and microstructural analysis and his constant encouragement and fruitful suggestions. I also wish to thank Professor Akira Ueno (Ritsumeikan University) for his kind support and useful suggestions in fractographical analysis on fracture mechanism of harmonic-structured stainless steels.

I would like to express my deep sense of gratitude to Dr. Octav Paul Ciuca, Dr.

Dmitry Orlov and Dr. Sanjay Kumar Vajpai (Global Innovation Research Organization, Ritsumeikan University) for excellent advices to use EBSD and TEM equipments and useful comments and advice on my research and journal paper preparation.

I am also heartily thankful to Professor Masao Sakane (Ritsumeian University) and Professor Xu Chen (Tianjin University), who gave me this opportunity to study in Japan and encouragement during my study.

I owe my most sincere gratitude to all of members in Ameyama laboratory, such as Dr. Eji Ota, Dr. Tatsuya Sekiguchi, Kouryu Kawadani, Masashi Nakatani, and so on, who have gave me many useful advice on my research and usual life in Japan. Special thanks to Bo Tong for his wonderful assistance.

My heartfelt thanks to all my friends, their encouragement and company kept my spirits high and joyful. Many thanks to all the other people not mentioned, but to whom I am grateful for their kind assistance in one way or another during the past six years.

Finally, I express my profound gratitude to my parents for their sacrifices, constant support, understanding and encouragement extended during my life in Japan.

December 2013

Kyoto, Japan

Zhe ZHANG

Table of Contents

Chapter 1 Introduction

1.1 Background

Austenitic stainless steels are the most common and familiar types of stainless steels. Due to their extremely corrosion resistance and oxidation resistance, these materials can be successfully used for chemical processing equipment, for food, dairy, and beverage industries, for heat exchangers, and for the milder chemicals.

However, austenitic stainless steels are in general of rather low yield strength. In order to remain the material of choice for these component manufacturers, the strength of stainless steels should be improved. It is well-known that strengthening arising from grain refinement is usually governed by the Hall-Petch relation, which projects a continuous rise of strength with decreasing grain size. Therefore, in order to enhance the strength of materials, the past decade has witnessed a surge in research and development worldwide to drive the grain sizes of bulk metals and alloys down into the so-called ultrafine-grained (UFG) and nanocrystalline (NC) regime. UFG/NC steels demonstrated superior strength and hardness compared to their coarse-grained (CG) counterparts. Besides strength, wear resistance, pitting resistance and resistance to cavitation and cavitation-erosion can also be improved by reducing grain size. Furthermore, damage/intergranular precipitation and segregation caused by irradiation is believed to be reduced in UFG/NC stainless steels, because the copious amounts of grain boundaries enable irradiation-generated point defects to annihilate.

However, for some applications, an appreciable uniform elongation under tensile stresses is required, but is rarely available in traditional homogeneous UFG/NC materials. The limited ductility of UFG/NC materials is a major barrier to their widespread commercial usage. Briefly, the reason for the inadequate ductility is prone to instabilities on plastic deformation, which leads to early strain localization and failure and also due to a reduced ability of the materials to accommodate the progression of cracks by extensive plastic deformation.

Therefore, it is imperative to achieve the improvement of both the mechanical properties, i.e. a combination of high strength and good ductility, in the UFG/NC steels to make them really attractive for the aforementioned applications. A key to meeting the ductility challenge is to use stabilizing mechanisms to overcome the instabilities that threaten the tensile elongation of UFG/NC metals and alloys. Bimodal (or multi-modal) grain size distribution is a useful strategy to enhance ductility, which could achieve simultaneously good yield strength and fairly large uniform (and total) elongation. The UFG/NC matrix in the bimodal microstructure provides the high strength, while the relatively large coarse grains contribute to the ductility. However, the exact distributions of the grain size, grain shape, and spatial locations depend on many processing parameters and may be difficult to reproduce. The outcome properties therefore span a relatively wide range depending on the microstructural variations. The overall of material response is tricky to predict and model.

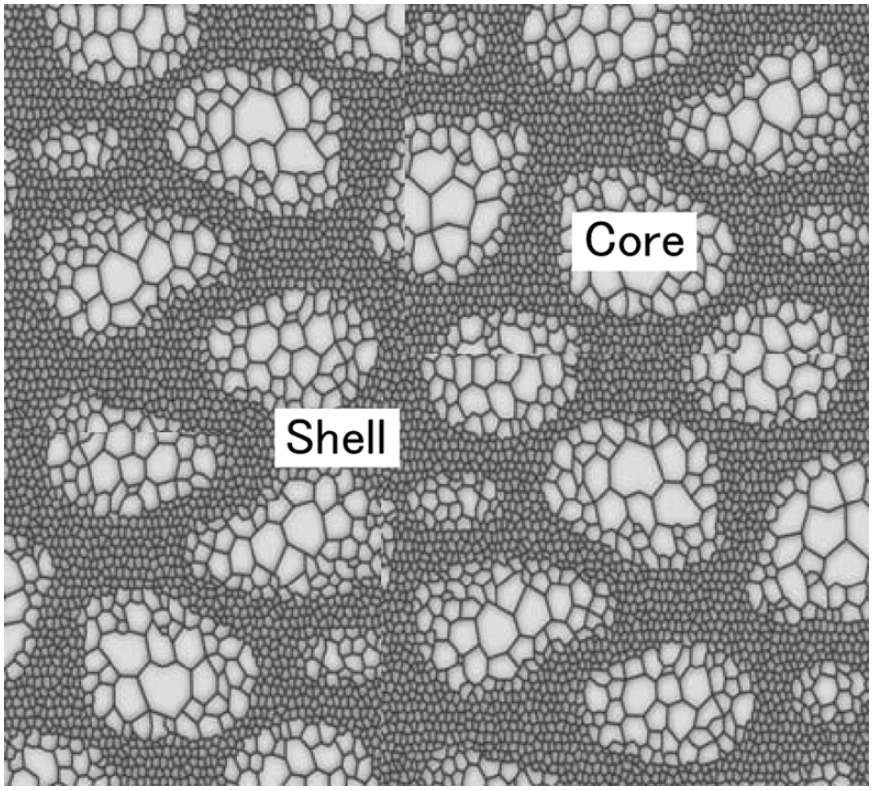

Figure 1.1 Schematic of a harmonic-structured material.

Recently, professor Ameyama and co-workers proposed another powder metallurgy (PM) based approach to create a novel bimodal microstructure design called “harmonic structure”. Effectively, this is a regular “nano and heterogeneous bimodal structure” consisting of CG areas (or “cores”) enclosed in a three-dimensional continuously connected network of UFG structure (or “shell”), see Fig.1.1. The concept of harmonic structure design has been successfully applied in a variety of materials, such as pure Ti, Cu, alloy Ti-6Al-4V, and two-phase steel SUS329J1. All these materials demonstrated a winning combination of improved strength and ductility as compared to their CG as well as UFG counterparts. However, there is still no investigation of harmonic-structured austenitic stainless steel. The effect of the three-dimensional continuously connected network of UFG structure on improved ductility has not been revealed yet.

1.2 Objective of Dissertation

This dissertation describes the work that has been carried out to obtain a better understanding of the manufacture, mechanical properties, deformation and fracture mechanism of austenitic stainless steel having “harmonic structure”. The fabrication and characterization of harmonic structure in SUS304L stainless steel by the PM approach, which involves the mechanical milling of the steel powder followed by its consolidation using conventional sintering process, such as spark plasma sintering (SPS) and hot isostatic pressing (HIP).

In the present dissertation, the follow contents will be discussed:

(i) Fabrication of harmonic-structured SUS304L steels and microstructural evolution during mechanical milling and sintering process.

(ii) Relationship between microstructure and mechanical properties and superiorities of the harmonic-structured SUS304L steels when compared to those of “homogeneous” CG and UFG steels and conventional “heterogeneous bimodal structured” steels.

(iii) Role of the three-dimensional continuous network of UFG structure in improving the ductility, in particular uniform elongation in tension.

(iv) Deformation and fracture mechanism of harmonic-structured SUS304L steels.

(v) Mechanical properties, deformation and fracture mechanism of mechanical milled SUS304L water-atomized powder steels.

1.3 Outlet of Dissertation

The present dissertation consists of seven chapters as follows:

Chapter 2 presents a brief review on characteristics of austenitic stainless steels and powder metallurgy including fabrication processes of the metal powders, since austenitic stainless steel powders and powder metallurgy method are applied to fabricate the harmonic-structured steels in present thesis. Subsequently, a brief overview of the recent progress of bulk nanostructured materials including synthesis methods and mechanism of UFG/NC structure, the mechanical properties and limitation of bulk UFG/NC metals, the possible strategies to enhance tensile ductility of UFG/NC metals are illustrated. Finally, the research progress of "harmonic structure designed" materials is introduced.

The experimental procedure in the present study is described in Chapter 3. The fabrication of harmonic-structured SUS304L steels by mechanical milling and consolidating process, samples preparation for microstructural observations as well as mechanical properties tests are introduced in detail.

Chapter 4 presents the synthesis method of "harmonic structure" in SUS304L steels by MM-SPS method using the "clean and spherical" PREP powders. The microstructure evolution and mechanical properties of harmonic-structured SUS304L steels comparing with conventional CG and UFG bulk are discussed.

A general discussion is presented in Chapter 5 which focuses on the role of the three-dimensional continuous network of UFG structure in improving the ductility, in particular uniform elongation in tension. The tensile property of the bimodal structured SUS304L steels having different spatial distribution of CG and UFG components is

compared. The superiorities of “harmonic structure designed” materials on mechanical property are revealed. The deformation and fracture mechanism of harmonic-structured SUS304L steels are also illustrated.

Due to the high volume production and low-cost, water-atomized steel powders are common applied in industry. Therefore, SUS304L water-atomized powders are also attempted to synthesize “harmonic structure designed” SUS304L steel in Chapter 6. However, owing to high oxygen content in water-atomized powders, a large amount of SiO_2 particles tend to precipitate in the UFG region of sintered compacts. The effects of SiO_2 particles on deformation and fracture behavior of SUS304L water-atomized powder steels are discussed. SiO_2 particles are harmful to the inter-particle bonding which results in poor ductility during mechanical loading. In order to obtain enhanced mechanical properties, the surface silicon oxide particles should be reduced.

Chapter 7 summarizes the main findings and conclusions in this study. It also proposes some future work that should be carried out in order to obtain further understanding in this research area.

Chapter 2 Literature Review

2.1 Austenitic Stainless Steels

Stainless steels are an important class of alloys widely used in many fields, from low-end applications, like cooking utensils and furniture, to very sophisticated ones, such as space vehicles, the use of stainless steels is indispensable.

Chromium	Oxidation Resistance
Nickel	Austenite former - Increases resistance to mineral acids Produces tightly adhering high temperature oxides
Molybdenum	Increases resistance to chlorides
Copper	Provides resistance to sulfuric acid Precipitation hardener together with titanium and aluminum
Manganese	Austenite former - Combines with sulfur Increases the solubility of nitrogen
Sulfur	Austenite former - Improves resistance to chlorides Improves weldability of certain austenitic stainless steels Improves the machinability of certain austenitic stainless steels
Titanium	Stabilizes carbides to prevent formation of chromium carbide Precipitation hardener
Niobium	Carbide stabilizer - Precipitation hardener
Aluminum	Deoxidizer - Precipitation hardener
Carbon	Carbide former and strengthener

Figure 2.1 Stainless steel alloying elements and their purpose [3]

Stainless steel is an alloy of iron, wherein chromium imparts a special property to the iron that makes it corrosion resistant. As the chromium content is in excess of 10.5%, the corrosion barrier changes from an active film to a passive film. While the active film continues to grow over time in the corroding solution until the base metal is consumed,

the passive film will form and stop growing. This passive layer is extremely thin, in the order of 10-100 atoms thick, and is composed mainly of chromium oxide which prevents further diffusion of oxygen into the base metal. Other elements, as illustrated in Fig.2.1, may be added for special purposes. [1-3]

There are five classes of stainless steel: austenitic, ferritic, martensitic, duplex and precipitation hardening. Austenitic grades are those alloys which are commonly in use for stainless applications. The austenitic grades are not magnetic. The most common austenitic alloys are iron-chromium-nickel steels and are widely known as the 300 series, as shown in Fig.2.2.

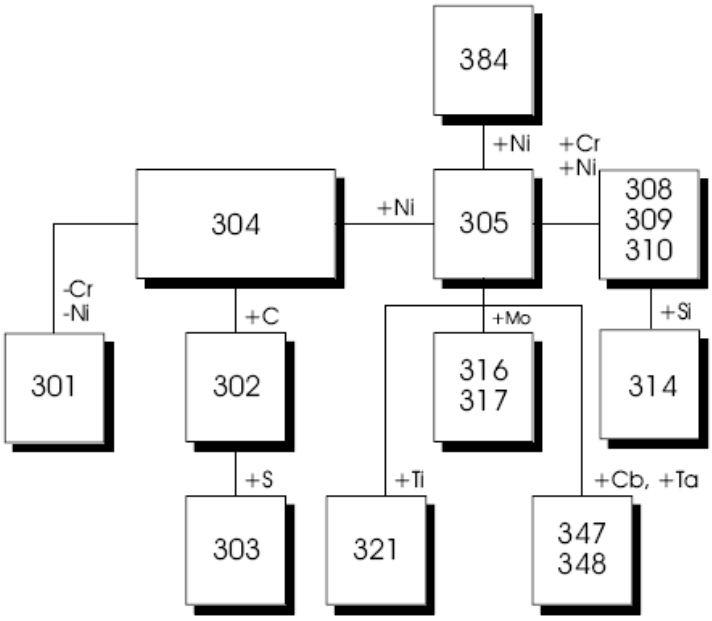

Figure 2.2 Austenitic group summaries [4]

The straight grades of austenitic stainless steel contain a maximum of 0.08% carbon. There is a misconception that straight grades contain a minimum of 0.03% carbon. The "L" grades are used to provide extra corrosion resistance after welding. The letter "L" after a stainless steel type indicates low carbon (as in SUS304L). The carbon is kept to 0.03% or under to avoid carbide precipitation. The "L" grades are more expensive.

Whereas, the “H” grades, which contain a minimum of 0.04% carbon and a maximum of 0.10% carbon, are designated by the letter “H” after the alloy. Since carbon imparts great physical strength at high temperatures, so people ask for “H” grades primarily when the material will be used at extreme temperatures as the higher carbon helps the material retain strength at extreme temperatures.

Comprehensively, the austenitic stainless steels, because of their high chromium and nickel content, are the most corrosion resistant of the stainless group providing unusually fine mechanical properties. It is used for chemical processing equipment, for food, dairy, and beverage industries, for heat exchangers, and for the milder chemicals. They cannot be hardened by heat treatment, but can be hardened significantly by cold-working. The major drawback of austenitic stainless steels is the low yield strength. In order to increase the safety of equipment, it is necessary to strength the austenitic stainless steel. [4-6]

2.2 Powder Metallurgy

Powder Metallurgy (PM) is a continually and rapidly evolving technology embracing most metallic and alloy materials, and a wide variety of shapes. PM is a highly developed method of manufacturing reliable ferrous and nonferrous parts. The subsequent rapid development of PM is due to many reasons, which including:

(i) Reduction of machining;

(ii) High raw material utilization;

(iii) Low energy requirements;

(iv) Large variety of geometrical shapes combined with narrow tolerances;

(v) Good reproducibility of geometrical and mechanical-physical properties;

(vi) Outstanding suitability for mass production.

Thus these advantages lead to a favorable cost situation in the mass production of mechanically stressed geometrically complex structural parts with narrow tolerances. The powder metallurgical route is often more economical in terms of cost, precision, and productivity than other processes such as casting and forging. [7]

2.2.1 Manufacture and Characteristics of Metal Powders

Techniques such as water atomization, gas atomization, centrifugal atomization, plasma atomization, mechanical attrition and alloying, melt spinning, plasma rotating electrode process (PREP), and a variety of chemical processes are applied to produce metal powders. Processes for producing fine metal powders are listed in Fig.2.3. Chemical and electrolytic methods are used to produce high purity powders. Mechanical milling is widely used for the production of hard metals and oxides. [8] Since the water-atomization, gas-atomization and plasma rotating electrode process (PREP) are the common processes for fabrication of metal powders, thus the production processes and characteristics of these powders are introduced in detail here.

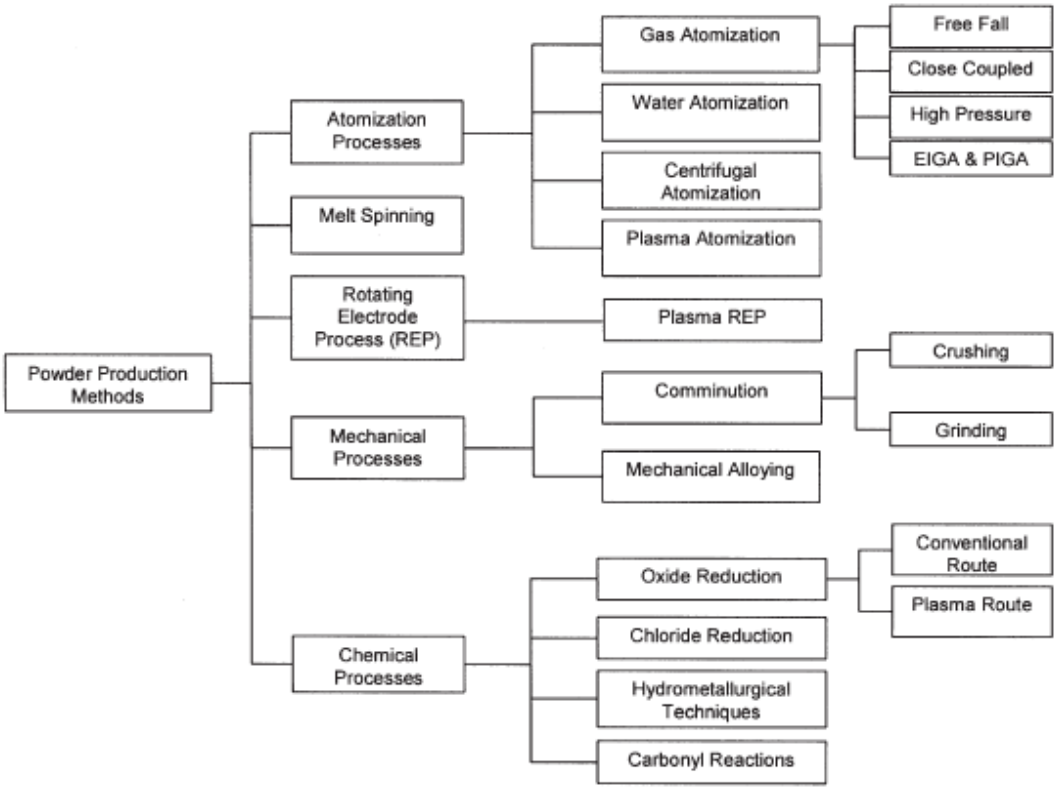

Figure 2.3 Different processes for powder production. [8]

(I) Water Atomization

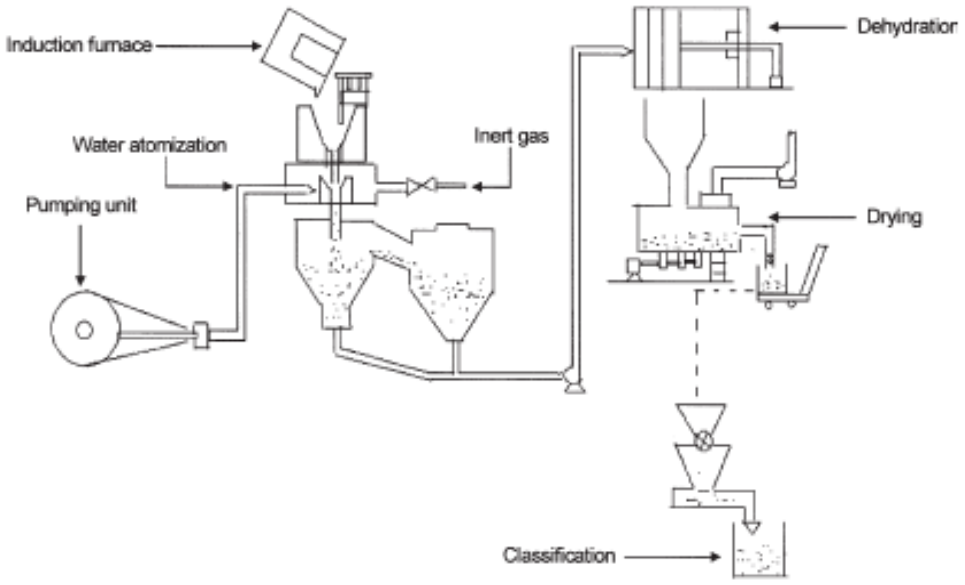

Figure 2.4 A schematic sketch of water-atomization process. [8]

The most common technique for producing metal powder is water atomization. This technique uses water jets to atomize the molten metal (Fig.2.4). The material is first melted in an induction furnace and poured into a tundish. The resulting metal stream is blown out in a fine jet while water from a high-pressure pump is blown until the metal becomes atomized. The resulting powder is dried and classified for particle size depending on its intended usage. This process makes use of the superior atomization ability of the V-jet nozzle, which was developed by Kobe Steel. Oxidation of the melt stream can be prevented by carrying out the atomization in an inert atmosphere or sealing the area around the water jet nozzle with a chamber filled with inert gas. At greater water jet pressures, the final products are more irregular. Below a certain water jet pressure, atomization is impeded. Thus, an optimum level of pressure is required to carry out the atomization. [8, 9]

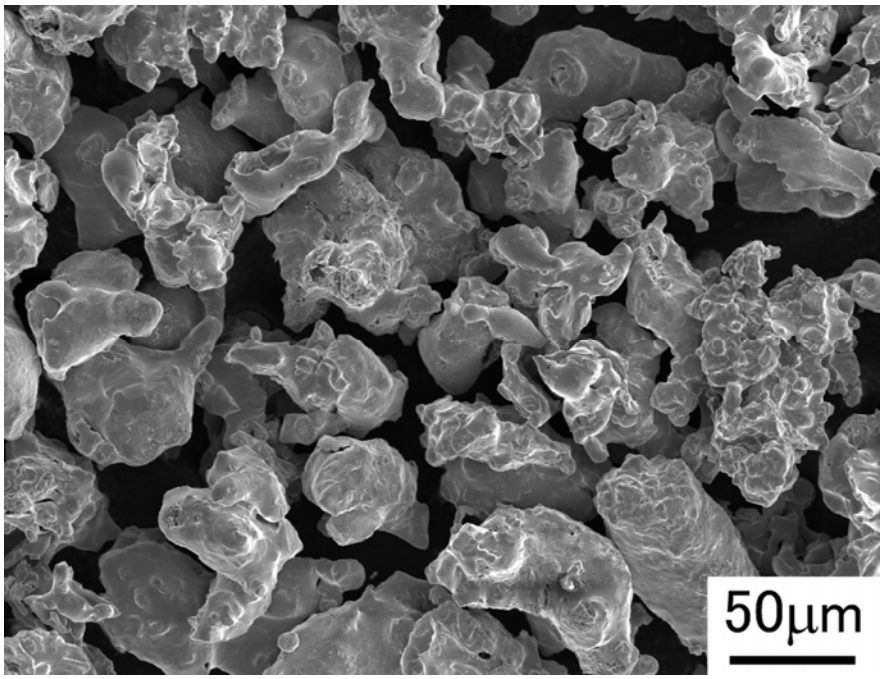

Figure 2.5 Morphology of water-atomized SUS304L powders.

(The average powder size is approximately 80μm)

Due to the great water pressure and rapid cooling rate, the water atomization

processes provide a substantially larger variation in particle shape, particle-sized distribution and possible alloy states. The particle size can be reduced to less than 40μm. [10-12] Morphology of water-atomized SUS304L powders is given in Fig.2.5.

Water-atomization is the dominant method for producing metal and pre-alloyed powders from aluminum, brass, iron, low alloy steel, stainless steel, tool steel, super alloy, titanium alloy and other alloys. It is the most common technique for high volume production of steel powder at low cost. An important advantage of water-atomized steel powder, besides cost benefits, is the irregular powder shape, which facilitates good green body strength and makes the powder highly suitable for net shaping of components by means of die pressing. However, since stainless steel contains strong oxide-forming elements such as Cr, Si and Mn, atomization and sintering procedures must be carefully controlled in order to limit the oxygen content of the sintered material. Otherwise, the bonding between the metal particles and thus the mechanical properties of the sintered material should be significantly impaired. [13-16]

(II) Gas Atomization

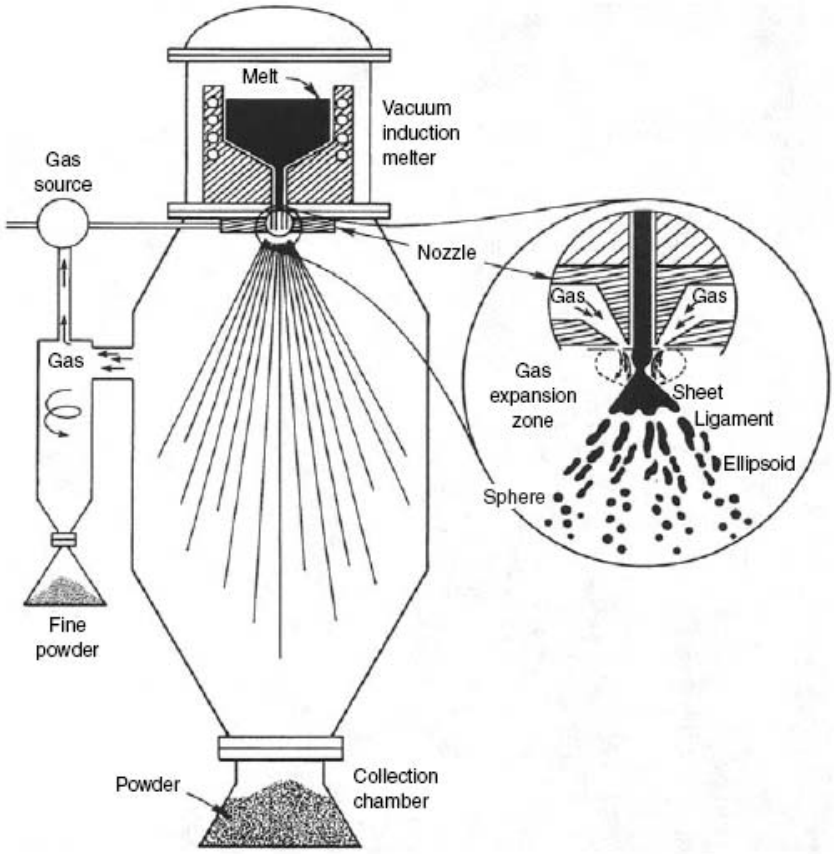

Figure 2.6 A schematic sketch of gas-atomization process. [9]

Water atomization is limited with respect to special powder quality criteria, such as particle geometry, particle morphology and chemical purity. Therefore, production of high-quality metal powders is becoming important to meet the increasing demand for manufacturing advanced materials. Gas atomization is a process to manufacture high quality metal powders. This technique uses air, steam, or an inert gas to produce powders from molten metal. Metal ingot or metal materials are melted in an induction furnace or gas furnace (Fig.2.6). The molten metal prepared in a furnace is transferred to the ladle and then to the tundish to make a molten metal stream. It is disintegrated to powder by the impact of gas jets from the nozzles. Because of problems with this technique, such as contamination of final powders resulting from molten metal reacting

with the ceramic linings of the tundish, ceramic free-melting techniques with inert-gas atomization were developed. The two inert-gas atomization processes are electrode-induction melting in combination with inert-gas atomization (EIGA) and plasma melting in combination with inert-gas atomization (PIGA). [8, 9, 17-20]

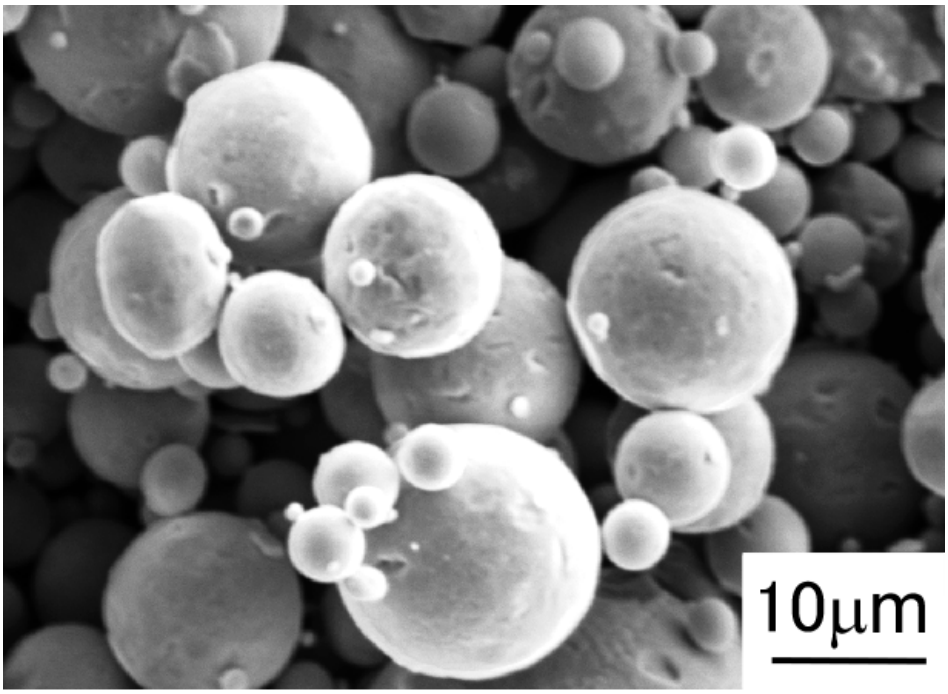

Figure 2.7 Morphology of gas-atomized SUS316L powders.

(The average powder size is approximately 10μm)

Gas-atomized stainless steel powders have spherical particle shape (Fig.2.7) and superior packing densities. Median particle size, dependant on the atomization parameters and melting properties, ranges from 10-100μm. Gas-atomization is the leading powder making process for the production of high-grade metal powders, such as aluminum, nickel, brass, titanium, high speed steel, stainless steel and other alloys. The gas-atomized powders have specific quality criteria such as spherical shape, high flow rate, high cleanliness, and low oxygen content and rapid solidification structures. [21-24]

(III) Plasma Rotating Electrode Process (PREP)

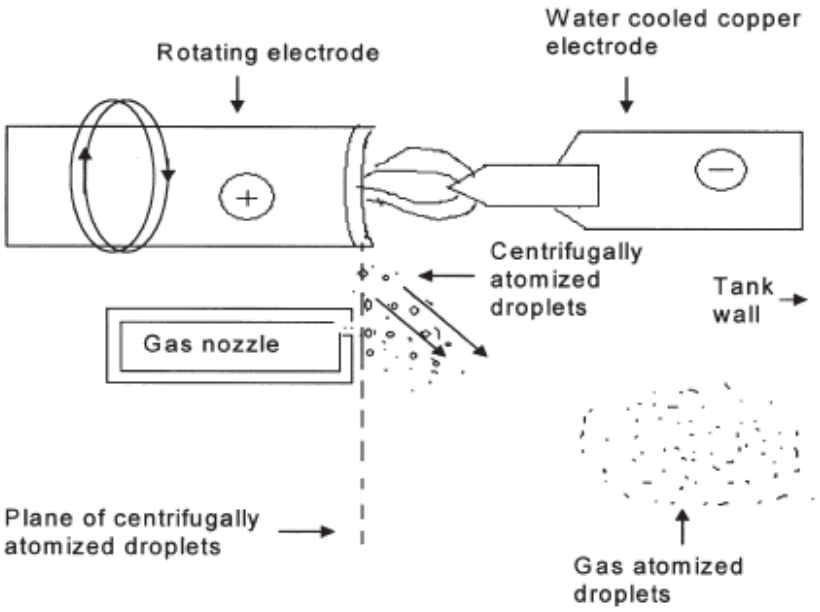

Figure 2.8 A schematic sketch of plasma rotating electrode process. [8]

Plasma rotating electrode processes to produce high purity metal powders. The rotating electrode process (REP) was invented and commercialized by Nuclear Metals in the early 1960s. In the early 1970s, the REP process was upgraded by replacing the electric arc as a heat source with plasma, and is now called the plasma rotating electrode process (PREP). In a REP process, the bar surface or the rotating electrode is melted either by using an electric arc or with high-temperature plasma. The molten droplets are ejected from the surface of the electrode by the centrifugal forces and intersect the gas jet, which is arrayed around the perimeter of the electrode. Upon impact and entrainment in the jet, the droplets are shattered a second time by the aerodynamic drag imposed on them by the gas jet. A schematic sketch of PREP process is shown in Fig.2.8. [8, 25, 26]

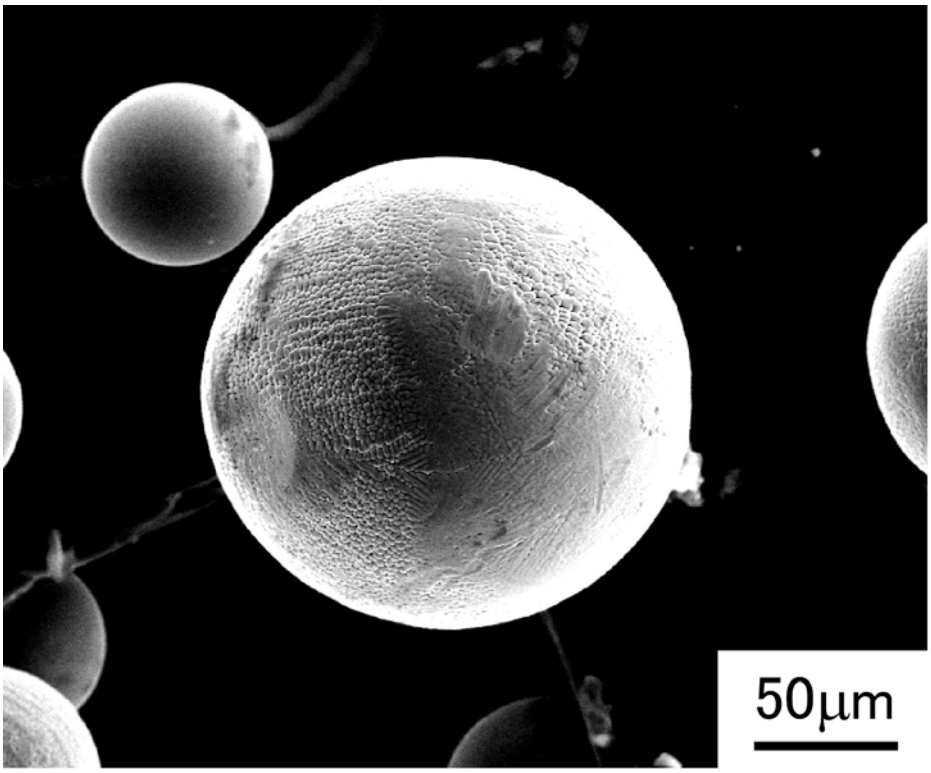

Figure 2.9 Morphology of PREPed SUS304L powders.

(The average powder size is approximately 120μm)

Compared to gas-atomized powder, PREP powder is relatively coarse and almost more than 100μm. The SUS304L powders fabricated using PREP method is shown in Fig.2.9. The PREP has several inherent characteristics that make it uniquely suitable for the fabrication of specific alloy powders to provide manufacturing and product advantages. First, PREP is a means of contactless melting and atomization to make powder with the highest level of cleanliness possible. This is a critical feature for reactive, high-melting-temperature alloys that are aggressively corrosive in their molten state and attack conventional ceramic crucibles. Such alloys are routinely atomized by PREP without incurring contamination. Examples are titanium, zirconium, molybdenum, and vanadium alloys. Second, PREP powder is almost perfectly spherical and practically satellite free. Because the atomized droplets are dispersed and

move radially away from each other there is little opportunity for collisions between droplets and particles and the resulting coalescence of the two into irregularly shaped clusters. This single-particle nature of the powder spheres results in PREP powder being very free flowing and having a high packing density, approximately 65%. Also, PREP powder has both a tighter size distribution and a larger median size than can be produced by gas atomization. Finally, Since PREP atomization is produced by centrifugal forces rather than by aerodynamic drag, the powder is essentially porosity free when compared to gas-atomized powder. However, electricity represents proportionately higher costs for the metal powder producer. Summarily, PREPed powders are characterized by higher purity, higher cost metal powders. [27-30]

2.2.2 Limitations of Powder Metallurgy

In conventional steelmaking process for bulk stainless steel, since oxygen is blown through molten pig iron, silicon and phosphorus become oxidized easily and enters the oxide slag phase of the slag/steel equilibrium, whereas chromium predominantly remains unoxidized in the steel phase. Any chromium that has become oxidized and has entered the slag phase is recovered by subsequent deoxidation with silicon. After refining, impurities such as silicon, phosphorus, and excess carbon are removed from the raw iron, and alloying elements such as manganese, nickel, chromium and vanadium are added to produce different grades of steels.

The main difference between conventional steelmaking bulk and PM compact is that, in the former, the undesirable silicon dioxide is removed by the slag, whereas in PM it remains in the product unless it is removed or reduced during sintering. Therefore, the

surface segregation and oxidation state of steel powders have been investigated. Nyborg et.al. illustrated the surface product formation of a series of steel powders fabricating by various processes using electron spectroscopy for chemical analysis (ESCA) and Auger electron spectroscopy (AES). Also the mechanical properties of sintered compacts have been studied. [13-15, 31-33] It is reported that segregation formed near the powder surface due to the inhomogeneous cooling rate. Investigations of austenitic stainless steel powder and sintered components showed a strong correlation between the characteristics of surface oxide and solidification structure. [34-37] It is also reported that since stainless steel contained strong oxide-forming elements such as Cr, Si and Mn, even cooling in the inert gas atmosphere, slight oxide layer and surface segregation were still existed near the stainless steel powder surface. After refining, impurities such as silicon oxide, chrome oxide cannot be removed from sintered compacts completely. The residual oxides, sometimes termed acid insolubles, can reduce the mechanical properties of a sintered part. In order for mechanical properties to develop properly and in a reasonable amount of time, it is critical that the formed oxide impurities are unpopular and necessary for reduction. Moreover, lower the amount of oxygen (oxides) clearly and significantly improves the dynamic mechanical properties of sintered stainless steels, that is, fatigue and impact strength.

2.3 Ultrafine-grained (UFG)/ Nanocrystalline (NC) Metals

2.3.1 Manufacture Processes of UFG/NC Metals

Since the pioneering work of Hall [38] and Petch [39], a finer grain size increases the

strength and the fracture toughness of the materials. Material scientists and engineers have been attracted by materials with small grain sizes. Fig.2.10 shows various processes to produce UFG/NC materials of respective grain size ranges. In steel industry, thermo-mechanical control processing (TMCP), which consists of controlled hot rolling and accelerated cooling, has been developed to produce fine-grained materials with grain size down to around 5μm. In order to obtain the finer grains up to 1μm extended TMCP processes have been developed. In such processes, diffusional transformation and/or recrystallization are mainly utilized to refine grains. In the conventional deformation processes such as rolling, drawing, extrusion, further refinement of grains to less than 1μm is quite difficult since the final product size limits the maximum amount of strain introduced. To eliminate the strain limit arising from the materials size reduction, severe plastic deformation (SPD) have been developed. [40, 41]

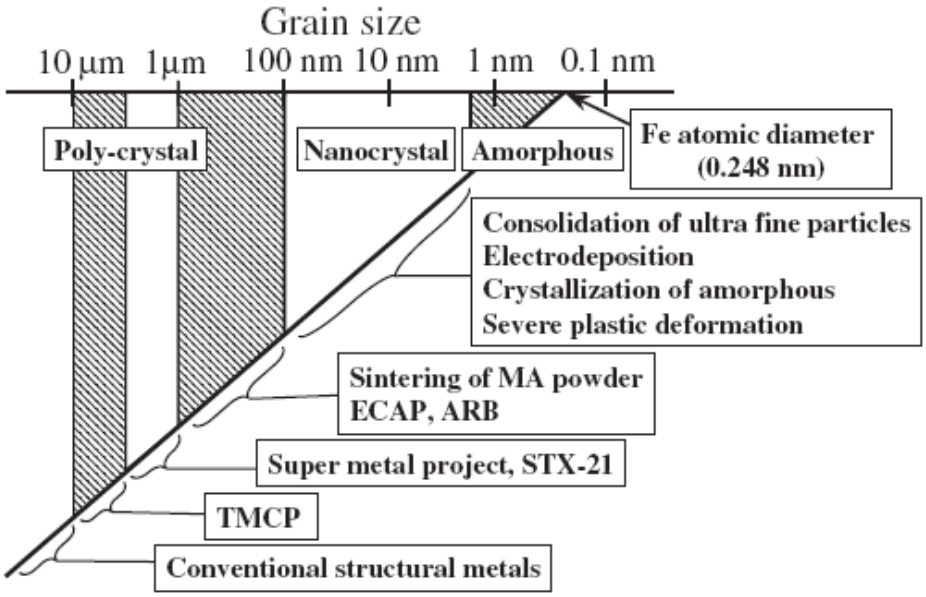

Figure 2.10 Production methods of UFG materials for respective grain size range. [40]

Processing of bulk UFG/NC materials in principle are accomplished by either the "bottom-up" assembly of atoms or molecules into UFG/NC clusters that require

subsequent consolidation into bulk material, or the "top-down" methods that start with a bulk solid and obtain a UFG/NC structure by structural decomposition. The bottom-up methods include the inert-gas condensation, electrodeposition, chemical/physical deposition, ball milling with subsequent consolidation and cryomilling with hot isostatic pressing. In the top-down synthesis approaches, coarse-grained (CG) materials are refined into UFG/NC materials through heavy straining or shock loading. [42, 43] One of widely used top-down methods is severe plastic deformation (SPD), which breaks down the microstructure into finer grains. The term SPD was firstly introduced by Valiev and his cooperators. In the last decade, this process established itself very well as an effective method for the production of bulk UFG/NC materials [44].

As shown in Fig.2.11, several methods of SPD are now available for refining the microstructure in order to achieve superior strength and other properties. Equal channel angular pressing (ECAP) is the most studied SPD processing technique. The ECAP method allows for the deformation of bulk samples by pure shear. By now nanostructures have been obtained in a number of pure metals, alloys, steels and intermetallic compounds using application of ECAP method by Valiev et al. [45-48] and Estrin et al. [49-52] Austenitic stainless steel is also processed for nanostructures at elevated temperatures by Zhang et al. [53, 54].

In the case of high pressure torsion (HPT), a disk-shaped sample is compressed to pressures of about 2~6GPa and then one of the dies is moved with respect to the other. With enough rotation very large values of strain can be achieved, well into the 100s. Horita et al. [55-59] make great contributions to the field of grain refinement of pure metals and alloys by HPT.

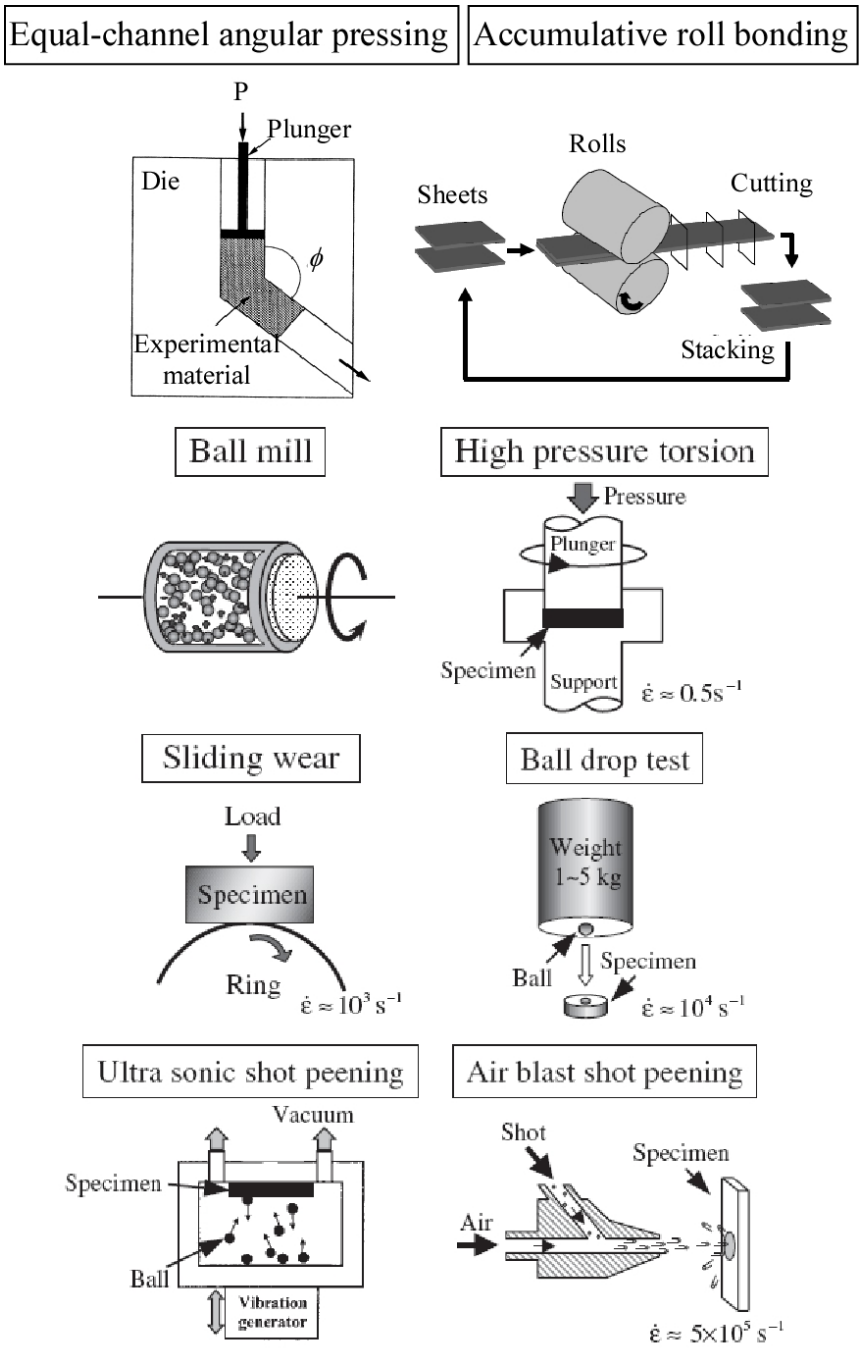

Figure 2.11 Schematic concepts of severe plastic deformation (SPD) methods

Tsuji et al. [60-65] get remarkable achievements in UFG/NC bulk producing by accumulative roll bonding (ARB) process. In this process, thin sheets of metal/alloy are taken and stacked together for roll bonding. The surfaces to be joined are roughened and cleaned; the two parts are stacked and roll bonded with approximately 50% reduction in

thickness. The bonded sheet is cut into two halves and again stacked after proper surface cleaning and rolled.

Mechanical attrition, the ball milling of powders, has also been found to refine the grain size to the nanoscale of all solid elements studied. [66-68] Creation of UFG/NC bulk materials is a two-step process wherein the nanosized powders are attrited and milled powders must be consolidated to give a bulk part subsequently. [69, 70] Lavernia et al. [71-75] make with great effort to produce UFG/NC pure metals and metallic alloys by cryomilling.

Additionally, sliding wear, a ball drop test, ultrasonic shot peening and air blast shot peening have also been applied to fabricate the UFG/NC bulk successfully. [40]

2.3.2 Grain Refining Mechanisms of Metals by SPD

Grain refinement by SPD implies the creation of new high angle grain boundaries (HABs). This can be accomplished by three mechanisms: (i) Elongation of existing grains during plastic deformation, causing an increase in high angle boundary area. (ii) Creation of high angle boundaries by grain subdivision mechanisms. (iii) Elongated grain can be split up by a localization phenomenon such as a shear band.

The evolution of microstructure during low temperature (<0.5Tm (melting temperature)) severe plastic deformation has been the subject of many investigators. The mechanisms of nanostructure formation during SPD are described briefly as follow. In the deformation at ambient temperature recrystallization during deformation will not take place and recovery is slow. Thus work-hardening continues up to large strains and grains are refined to nanometer range. A general microstructural evolution at various

stages of deformation is as follows. At small strains, original grains are subdivided into cells bounded by dislocation walls (called incident dislocation boundaries (IDBs)) with small misorientation. With increasing strain, cell size and cell wall width decrease and geometrically necessary boundaries (GNBs) develop. GNBs are boundaries which separate a group of neighboring cells with same slip system (called a cell block) from those with different slip systems. With further increase in strain, the density of GNBs and the misorientation of GNBs increase. Since the deformation induced high angle boundaries thus produce contain high density of dislocations and are distorted elastically, they are called non-equilibrium grain boundaries. The dislocation density inside grains is low in spite of the large strain imposed. When the grains are refined to 10nm range, the microstructure reaches a steady state since further strains are mainly accommodated by grain boundary sliding. By annealing, the nanostructures produce by severe plastic deformation does not recrystallize and show substantially slow grain growth. [40, 76]

2.3.3 Mechanical Properties of UFG/NC Metals

The great interest in the mechanical behavior of UFG/NC materials originates from the unique mechanical properties observed by many researchers of this field. Among these early observations, the mechanical behavior of UFG/NC metals and alloys are given in the following section.

(I) Strength

In a polycrystalline metal, grain size has a tremendous influence on the mechanical properties. Because grains usually have varying crystallographic orientations, grain

boundaries arise. While undergoing deformation, slip motion will take place. Grain boundaries act as an impediment to dislocation motion for the following two reasons: (i) Dislocation must change its direction of motion due to the differing orientation of grains. (ii) Discontinuity of slip planes from one grain another. The stress required to move a dislocation from one grain to another in order to plastically deform a material depends on the grain size. The average number of dislocations per grain decreases with average grain size (see Fig.2.12). A material with larger grain size is able to have more dislocation to pile up leading to a bigger driving force for dislocations to move from one grain to another. Thus you will have to apply less force to move a dislocation from a larger than from a smaller grain, leading materials with smaller grains to exhibit higher yield stress.

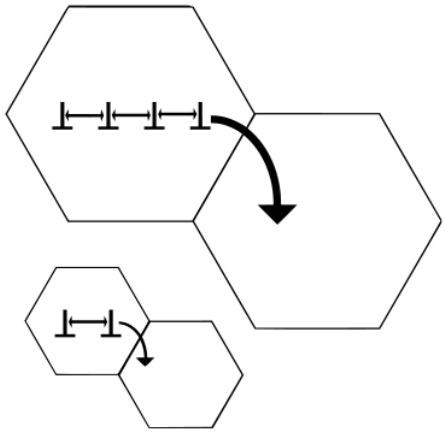

Figure 2.12 A schematic roughly illustrating the concept of dislocation pile up and how it effects the strength of the material.

It is well-known that strengthening arising from grain refinement is usually governed by the Hall-Petch relation. The conventional Hall-Petch relation is:

$$\sigma_y = \sigma_0 + k\sqrt{d} \tag{2.1}$$

where σ_y is the yield stress, σ_0 is the lattice friction stress, k is a quantity that

characterizes the transfer of slips through the grain boundaries and *d* is the mean grain size. Hall-Petch relationship projects a continuous rise of strength with decreasing grain size, in particular the yield stress. A physical basis for this behavior is associated with the difficulty of dislocation movement across grain boundaries and stress concentration due to dislocation pile-up. [42, 44] The Vickers hardness is also increasing with decreased grain size. Hardness values for nanocrystalline pure metals (~10nm grain size) that are 2~10 or more times higher than those of larger grained (≥1μm) metals. The mentioned researchers in Section 2.3.1 have shown the outstanding strength of UFG/NC pure metals, alloys, steels and intermetallic compounds. The remarkable Hall-Petch relationship of gain-refined SUS316L was observed in Fig.2.13. [62, 63, 77, 78]

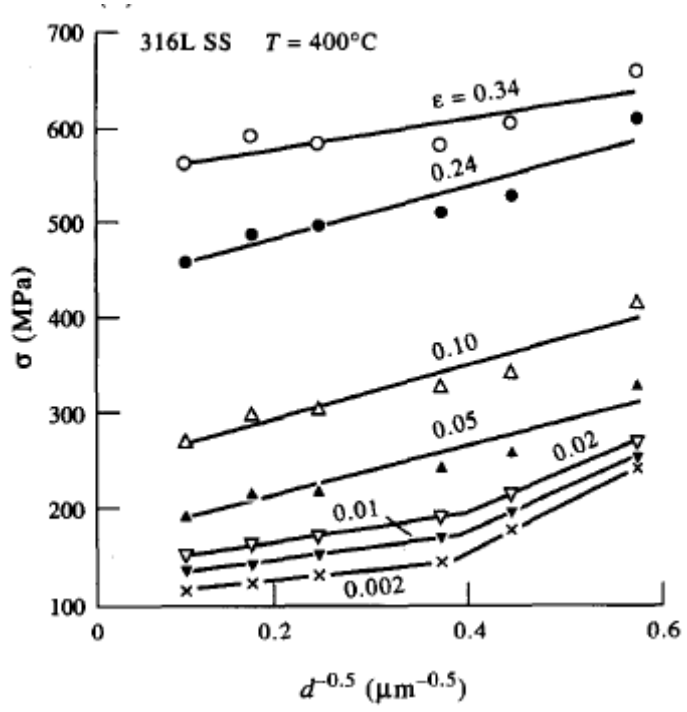

Figure 2.13 Hall-Petch of UFG/NC SUS304316L pots at different strains in the range 0.002-0.34 at 400°C. At any small strain <0.05, the plots exhibit two H-P lines. [77]

(II) Ductility

In the conventional grain size regime, usually a reduction in grain size leads to an increase in ductility. Thus one should expect a ductility increase as the grain size is reduced to nanoscale. However, the ductility is small for most grain sizes <25nm for metals that in the conventional grain size have tensile ductility of 40-60% elongation. UFG/NC bulk materials always show limited tensile ductility, especially limited uniform elongation, as shown in Fig.2.14. [79]

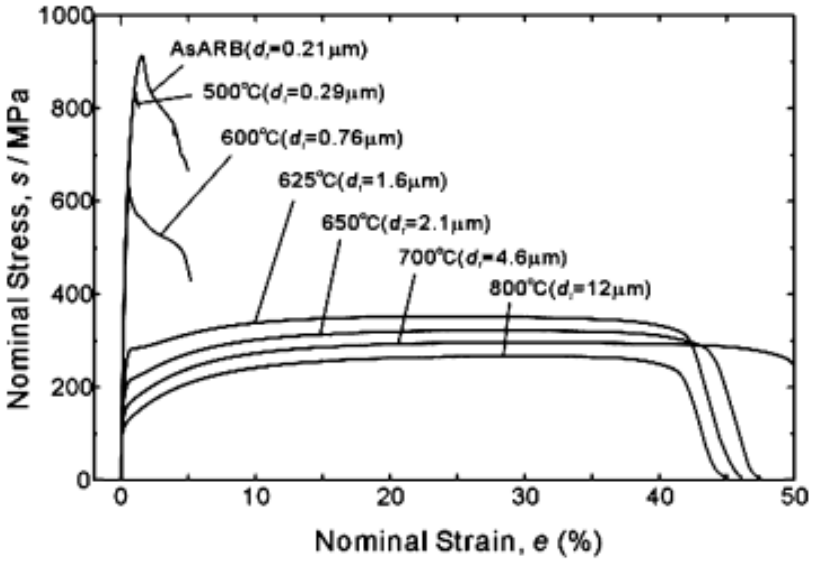

Figure 2.14 Engineering stress–strain curves of the IF steel ARB processed by 7 cycles at RT without lubrication and then annealed at various temperatures for 1.8ks. The annealing temperature and resulted mean grain size of each specimen are also indicated. [79]

Koch identified three major sources of limited ductility in nanocrystalline materials, namely: (i) Artifacts from processing (e.g., pores); (ii) Tensile instability; (iii) Crack nucleation or shear instability. It is difficult to process nanostructured materials free from the artifacts that mask the inherent mechanical properties. [42] Plastic instability

corresponds to necking propagation during tensile testing, so that it determines the uniform elongation of the materials. The simplest equation for the plastic instability condition of strain-rate insensitive materials (typical metals) is known as,

$$\sigma \geq \left(\frac{d\sigma}{d\varepsilon}\right) \tag{2.2}$$

where σ is flow stress (true stress) and dσ /dε is strain hardening. The condition can be schematically illustrated in Fig. 2.15.

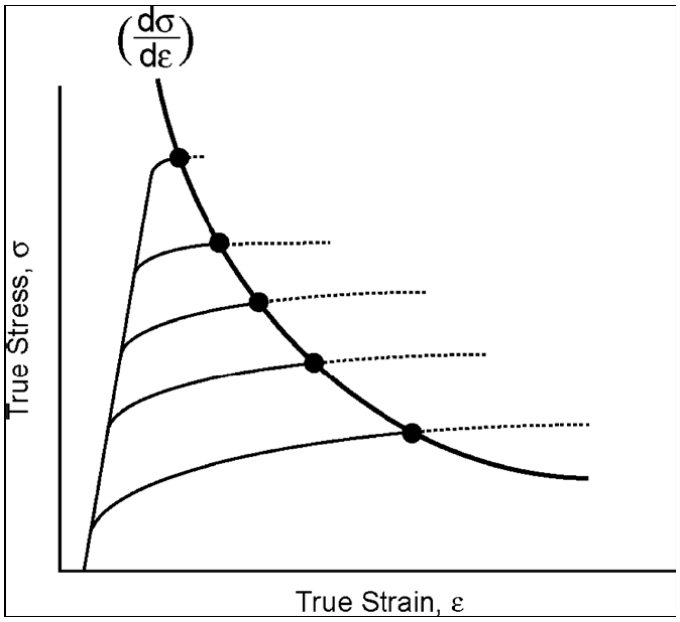

Figure 2.15 Schematic illustration showing the change in plastic instability points as yield strength increases. It is assumed that the strain-hardening rate is constant. [79]

In the figure, yield strength of a material increases by any strengthening mechanisms such as grain refinement strengthening. Here it is assumed for simplicity that the strain-hardening rate does not change even if the material is strengthened. According to Eq. (2.2), the position at which two curves (flow stress (σ) and strain-hardening rate (dσ/dε)) meet is the plastic instability point. The figure clearly shows that the plastic

instability condition is achieved at earlier stages of tensile deformation as the yield strength increases. Grain refinement raises the strength of metallic materials, and especially yield strength is significantly increased by fine grain structure. On the other hand, strain-hardening after macroscopic yielding is not enhanced by grain refinement. Rather a decrease in strain-hardening has been found in the UFG metal. Consequently, early plastic instability occurs in the UFG metals, resulting in limited uniform elongation in tensile tests. [79]

(III) Strain Rate Sensitivity

The engineering parameter measuring strain-rate sensitivity, *m*, is commonly defined as:

$$m = \left\{\frac{\partial \log \sigma}{\partial \log \dot{\varepsilon}}\right\}_{\varepsilon,T} \tag{2.3}$$

where σ is the follow stress, and $\dot{\varepsilon}$ is the corresponding strain rate. This engineering parameter is linked with the activation volume, V, through

$$m = \frac{\sqrt{3}kT}{\sigma V} \tag{2.4}$$

Here, *k* is the Boltzmann constant, *T* is the absolute temperature, and *V* is the activation volume of the flow stress. The strain-rate sensitivity is an indicator of the strain-rate response of the flow stress and is useful for technological comparisons and applications. For UFG/NC materials having large enough sample sizes and at least several percent tensile strain, the magnitude of the strain-rate sensitivity *m* can be routinely determined (using Eq. (2.3)) through jump tests.

Recent experimental evidence suggests that the strain-rate sensitivity in UFG/NC

metals is a function of grain size. It appears that all the FCC nanostructured materials show increasing strain-rate sensitivity with decreasing grain size. In contrast, BCC nanostructured metals exhibit decreasing strain-rate sensitivity as the grain size is reduced to the nanostructured regime. This trend is believed to preserve at least in the grain-size regime where the Hall-Petch relationship apparently holds. [80]

(IV) Fatigue

Discussing fatigue life, the classical Wöhler (S-N) plot is used most commonly, in which the fatigue life is plotted with regard to the stress amplitude. As UFG/NC materials generally show a significantly higher monotonic strength, which is due to a much higher athermal stress component σ_G, the fatigue lives are also superior compared to that of the CG counterparts. This statement holds for the low cycle-fatigue (LCF) regime as well as for the high cycle-fatigue (HCF) regime and for all UFG/NC materials investigated so far. Most recently, it was found for UFG copper that in the very high cycle-fatigue (VHCF) regime the fatigue lives are also superior to that of the CG counterpart. Fig.2.16 shows, as examples, the S-N diagrams for copper, aluminum and α-brass. Fig.2.16 (d) shows schematically the changes in the S-N plot when changing the microstructure from conventional to ultrafine grain size. Due to the significantly enhanced ultimate tensile strength (UTS) of UFG materials compared to the CG counterparts, the sustainable stress level at a given fatigue life is markedly increased in the LCF regime. As the stress amplitude decreases, the plastics train amplitude decreases and work hardening as an additional hardening mechanism is reduced. Hence, in the HCF regime the sustainable stress levels of the UFG materials at a given fatigue life are still superior to those of the CG condition, but the differences are not as high as

in the LCF regime. [81]

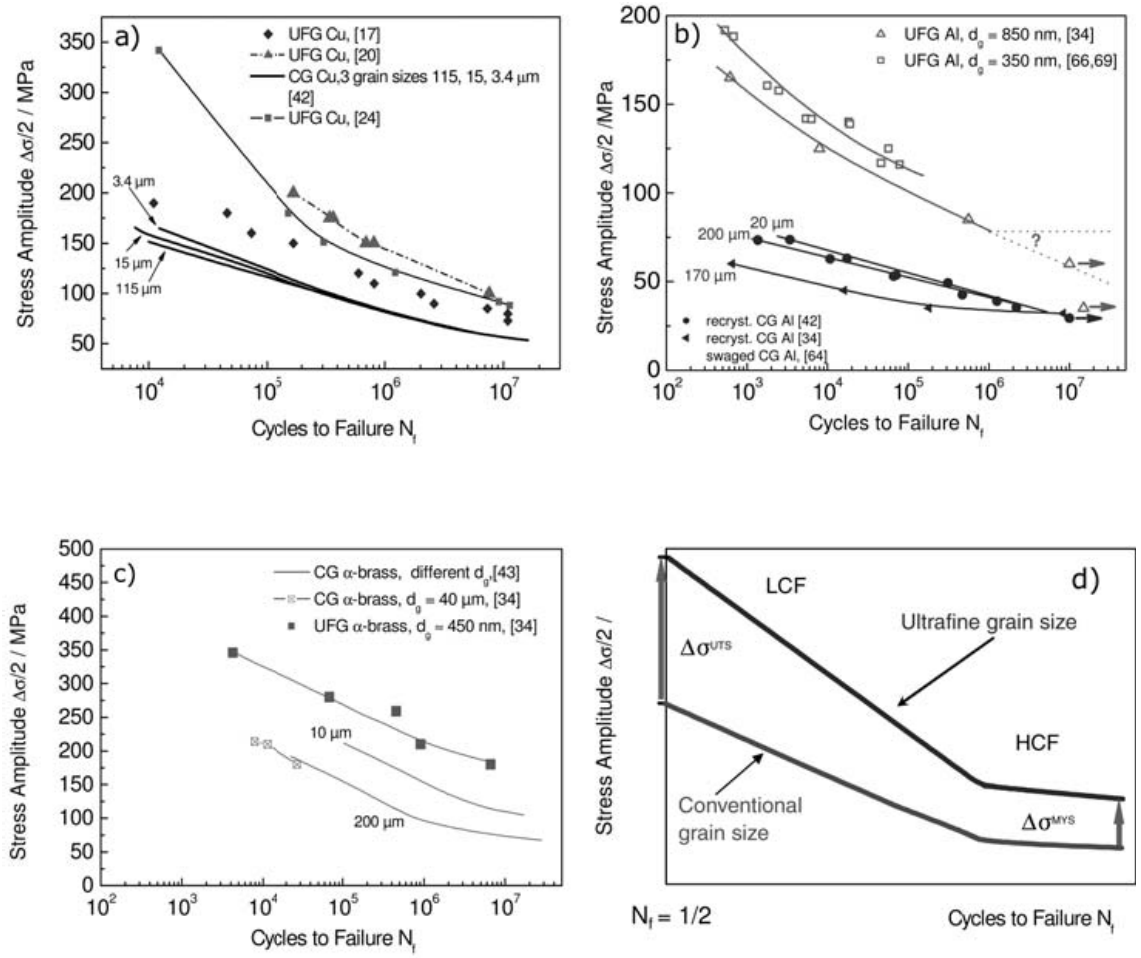

Figure 2.16 Wöhler S-N diagrams for (a) copper, (b) commercial purity (CP) aluminum, (c) α-brass for different grain sizes and (d) schematic view. [81]

(V) Superplasticity

When metallic specimens are pulled in tension, they generally fracture after relatively small amounts of ductility. However, some materials are capable of exhibiting superplastic behavior in which the samples pull out uniformly without failure and ultimately break at very high tensile elongations. This phenomenon of superplasticity is the basis for the superplastic forming industry in which complex shapes are formed from sheet metals for use in applications ranging from aerospace and transportation to

architectural decorations.

It is now recognized that two requirements must be fulfilled in order to achieve superplastic ductility. Firstly, the grain size of the material must be very small and typically less than 10μm. Secondly, since superplastic flow is a diffusion-controlled process, the temperature of deformation must be sufficiently high that diffusion rates are reasonably rapid. This means in practice that the temperatures associated with superplasticity are at and above $0.5T_m$, where T_m is the absolute melting temperature of the material.

The early prediction that the ultrafine grains introduced by SPD processing would lead to excellent superplastic properties, including the occurrence of superplastic flow at very rapid strain rates, has been fulfilled by the very extensive experimental data now available documenting the occurrence of superplasticity in a number of different alloy systems. Furthermore, there are numerous clear demonstrations that the superplastic effect is achieved in these nanostructured materials at strain rates that are significantly faster than those in conventional micrometer-grained materials. Nevertheless, it is important to recognize that superplasticity can be achieved only in those materials where the ultrafine grain sizes introduced through processing remain small and reasonably stable at the temperatures needed to attain diffusion-controlled plastic flow. This means in practice that superplastic flow is not easily achieved in pure metals or solid solution alloys where the grains grow rapidly when heated to high temperatures. [82]

2.3.4 Deformation Mechanisms of UFG/NC Metals

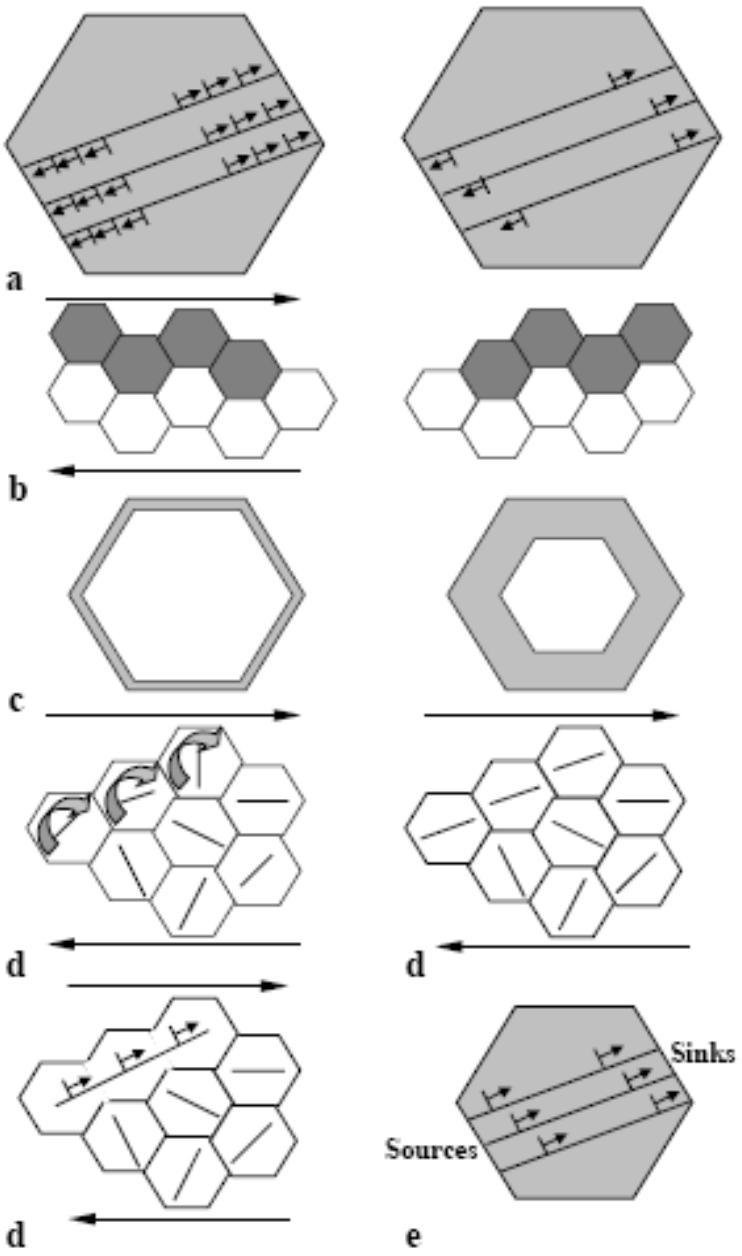

Figure 2.17 Sketches of different deformation mechanisms: (a) pile-up breakdown; (b) grain boundary sliding; (c) core and mantle; (d) grain coalescence; (e) sequential generation in grain boundary sources and annihilation in grain boundary sinks.

There are various physical models related to interpretation of the physics deformation

of UFG/NC metals and alloys. As shown in Fig.2.17, these models identify interrelationship between the deformation mechanisms active during grain refinement process and to determine their influence on the mechanical behavior.

The unique mechanical properties of UFG/NC materials are attributed to their unique deformation mechanisms, which, in many cases, are different from those in their CG counterparts. In summary, UFG/NC metals and alloys deform by mechanisms different from their CG counterparts. Deformation mechanisms in UFG/NC materials include slip of full dislocations and partial dislocations, deformation twinning, wide stacking faults, grain-boundary sliding and grain rotations. The activation and significance of each mechanism depend on intrinsic material properties such as stacking-fault energy and shear modulus, structural features such as grain size, and external factors such as applied stress and deformation temperature.

The following key points can be drawn from available molecular-dynamics (MD) simulations and experimental observations. Full dislocation slip is found active in grains as small as 10nm; however, its significance decreases with decreasing grain size. Emission of partial dislocations and deformation twinning become significant in nanostructured metals and alloys, even for those with high stacking-fault energy such as Al and Ni. There is a clear grain-size effect in the nucleation and growth of deformation twins. For metals and alloys with medium to high stacking-fault energy, deformation twins were observed in grains smaller than a certain value. Wide stacking faults were observed in nanostructured Al due to a grain-size effect. General planar fault-energy curves may be able to explain the stacking faults observed in nanostructured Ni but cannot reasonably predict the nucleation and growth of deformation twinning. Grain-boundary sliding and grain rotation may become significant deformation

mechanisms with decreasing grain size. [83]

2.3.5 Limitations of UFG/NC Metals

Strengthening at the cost of ductility is not uncommon, UFG/NC bulk materials indicate that they possess very high hardness and strength, 3~5times that of their CG counterpart, but their ductility, in particular uniform elongation in tension has been rather low and in the most cases nowhere close to that of the conventional metals and alloys. [84, 85] Both strength and ductility are the important mechanical properties of the materials for industrial applications. The UFG/NC materials have no capability to sustain a sufficient high rate of strain hardening and start necking soon after yielding, leading to a plunging tensile curve almost from the outset, which is a major shortcoming of UFG/NC materials.

In general, the tensile ductility of a solid is controlled by a competition between plastic deformation and fracture processes as well as by the resistance to plastic flow localization (Fig.2.18). Most UFG/NC metals fail to exhibit homogeneous plastic deformation in tensile testing (Fig.2.18b) but instead they are characterized by low tensile ductility at room temperature because of two processes: (i) brittle crack nucleation and propagation instabilities (Fig.2.18c) and (ii) plastic strain instability in the form of a localization of plastic flow in shear bands and neck formation (Fig.2.18d). The former process dominates in UFG/NC metals having the finest grains with grain sizes, d, lower than a critical value of $d_c \approx 10\sim30$nm depending on the material and structure characteristics. Alternatively, plastic strain instability is the main factor causing low tensile ductility in NC metals with intermediate grain sizes up to 100 nm

and in UFG metals with grain sizes from 100 to 1000nm. [86]

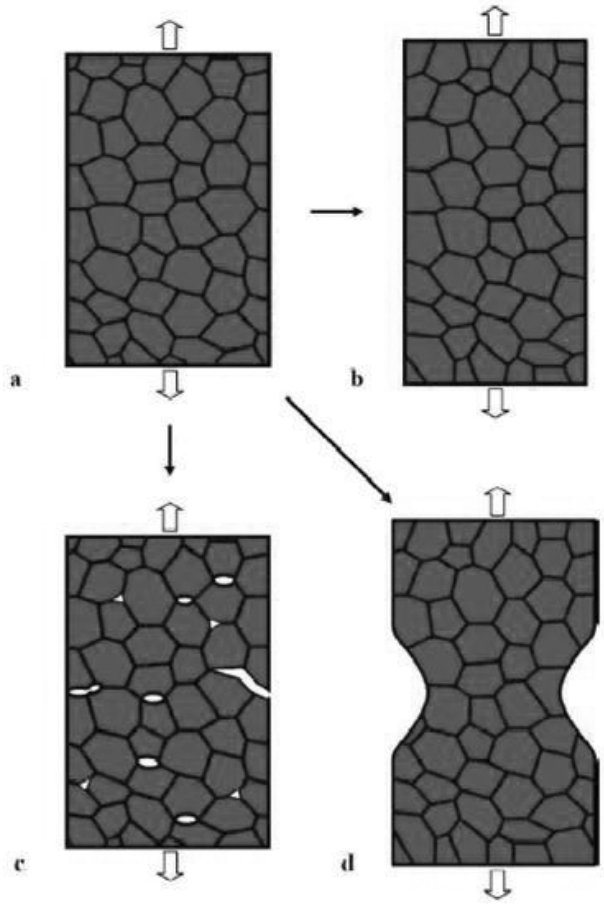

Figure 2.18 Key evolution routes of a NC specimen under tensile load. (a) Initial state of the NC specimen. (b) Homogeneous plastic deformation of the specimen corresponding to its enhanced ductility. (c) Brittle fracture in the NC specimen occurs through crack nucleation and growth instabilities, typically involving the fast nucleation of nanoscale cracks, their convergence and/or growth along the grain boundaries. (d) The specimen shows plastic strain instability with necking. Routes (c) and (d) correspond to low tensile ductility. [86]

Crack nucleation instability (Fig.2.18c) means that plastic flow is suppressed in a solid so that the applied stress rapidly reaches a level close to the critical stress needed to initiate cracks near local stress concentrations. These concentrations may occur either

at fabrication-produced flaws or at defects generated due to the very limited local plastic deformation. The subsequent crack propagation is due to the suppression of conventional toughening mechanisms, such as lattice dislocation emission from crack tips that are needed to provide a resistance to crack growth. [87, 88]

Plastic strain instability in a solid under tensile deformation (Fig.2.18d) is controlled by its strain hardening rate. CG polycrystalline metals exhibit good tensile ductility due to high strain hardening associated with lattice dislocation storage in the grain interiors during plastic deformation. By contrast, UFG/NC materials often have low values of strain hardening rate so that they typically show plastic strain instability. The low ductility is caused by the low strain-hardening rate, which cause early-localized deformation in the form of necking. In general, two factors are responsible for the low or zero strain-hardening rate: (i) A high density of dislocations already exists in nanostructured materials processed by SPD and the density quickly reaches saturation upon further deformation. Once the saturation is reached, dislocations no longer accumulate inside the grains and strain-hardening rate becomes zero. (ii) In the grains with very small diameters e.g. <100 nm dislocations are emitted from a grain boundary segment and disappear into another grain boundary segment on the opposite side of the grain without accumulating inside the grain. The saturation density of dislocation is determined by a balance between the dislocation generation rate and the recovery rate, and this saturation density is expected to be higher at lower deformation temperature and higher strains. [89, 90]

Additionally, in practice, these techniques are often limited to the production of fairly small samples that may be useful for applications in fields such as electronic devices but are generally not appropriate for large-scale structural applications. Furthermore, the

finished products from these techniques invariably contain some degree of residual porosity and a low level of contamination, which is introduced during the fabrication procedure. These drawbacks could be an insurmountable hurdle in bringing UFG/CG bulk materials from laboratory to commercialization.

2.3.6 Approaches to Improve Ductility of UFG/NC Metals

As mentioned in Section 2.3.5, it is well-known that the inadequate ductility of UFG/NC materials is caused by plastic strain instability or crack nucleation instability which is achieved at the early stage of deformation. Therefore, a key to meeting the ductility challenge is to use stabilizing mechanisms to overcome the instabilities that threaten the tensile elongation of NS metals and alloys. The basic approaches adopted to enhance the tensile ductility of UFG and NC metals are outlined briefly in this section. [86, 91, 92]

(I) Bimodal (multi-modal) grain size distribution.

What turned out to be interesting is that one could do better than just a simple trade-off. When the bimodal structure was created on the nano-micro-scale, a large gain in work hardening and uniform strain was achieved, with only a (relatively) small loss of strength. The extra strain hardening ability may have something to do with the microstructural length scales involved, which are in this case close to the characteristic (or intrinsic) length scale of a material for strain-gradient plasticity to play a significant role. The storage of geometrically necessary dislocations required for compatible plastic strains may be pronounced for the unusually large strain gradient produced. Also

possibly contributing is the twinning activities triggered by stress concentrations in a highly non-uniform grain structure deforming at a high flow-stress level.

Bimodal bulk UFG/CG metals and alloys can be synthesized by: (i) Thermo-mechanical treatment involving severe plastic deformation, i.e., cold rolling or equal-channel angular pressing, followed by an appropriate thermal annealing under controlled conditions [93-95]; and (ii) Mechanical milling plus the consolidation of the milled powders mixed with certain volume fractions of the as-received CG powders [96-98]. Hono et al. [99-101] fabricated the bimodal bulk materials by mechanical milling at room temperature and spark plasma sintering (SPS). Lavernia et al. [102-104] have been developed cryomilling followed by various consolidation methods for manufacturing bimodal bulk metals and alloys. Bimodal bulk metals and alloys, wherein comprised of UFG/NC grains separated by CG regions, show balanced mechanical properties of enhanced yield and ultimate strength and reasonable ductility and toughness as compared to comparable conventional alloys and UFG/NC metals and alloys. As the volume fraction of coarse grains is increased, tensile ductility increase and strength decrease.

The tensile deformation and fracture mechanism of bimodal pure Al and Al-Mg alloys have been reported. An enhanced tensile elongation associated with the occurrence of a Lüders band was observed in the bimodal alloys. [105-107] In the bimodal pure Ni, it is also found that the large localized plastic strain within the coarse grains was observed during compression. The strain localization resulted in occurrence of debonding and cracks in the NC region or in the interface between CG and NC components. [108] A descriptive model for tensile deformation and fracture of bimodal UFG/CG metals, as shown in Fig.2.19. Firstly, the CG regions are elongated along the

extrusion direction in the as-extruded specimen (Fig.2.19a), and uniaxial tension is applied to the specimen along the extrusion direction. When the stress reaches the yield point of the CG material, plastic deformation occurs within these regions. Secondly, as the stress increases and reaches the yield point of UFG/NC material, voids initiate within UFG/NC regions and at UFG/CG interfaces and the CG bands undergo elongation, as shown in Fig.2.19b. Thirdly, as the tensile strain increases, cracks grow from the voids and extend transverse to the load axis. However, the cracks tend to be localized in UFG/NC regions between CG regions, as shown in Fig.2.19c. Cracks are effectively impeded by the CG stringers, which blunt and bridge the cracks, causing, in some cases, deflection and branching in CG regions and at UFG/CG interfaces. Finally, fracture ensues when cracks link and the CG regions can no longer sustain the load, as shown in Fig.2.19d. The ductile coarse grains in the UFG/NC matrix effectively impede propagation of microcracks, resulting in enhanced ductility and toughness while retaining high strength. [105-108]

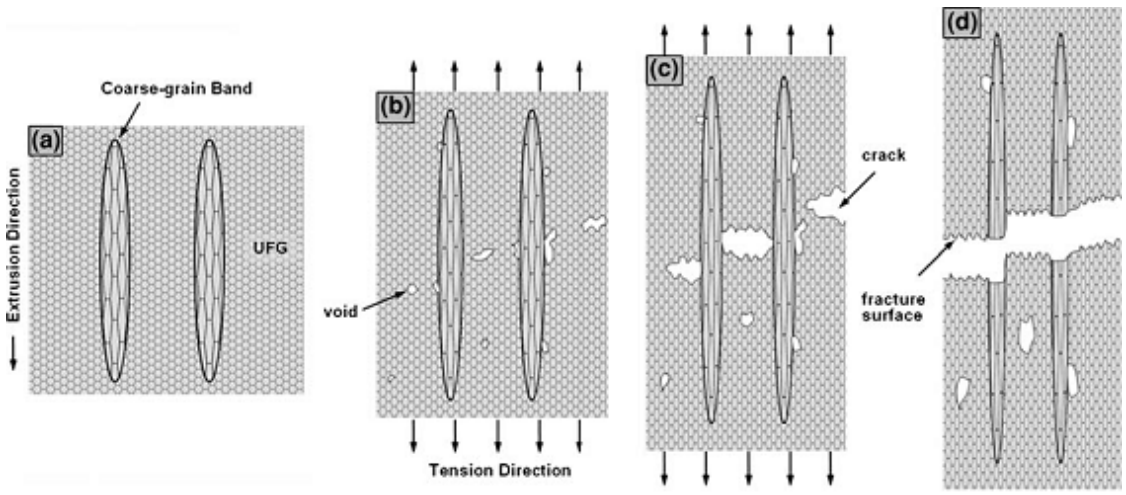

Figure 2.19 Schematic of tensile deformation and fracture mechanism of bimodal UFG Al-Mg alloys under uniaxial tension along the extrusion direction: (a) as extruded, (b) void nucleation and growth, (c) crack growth, and (d) fracture. [107]

This approach has these advantages: (i) The idea is simple and easy to grasp, the grain structure can be induced through traditional thermo-mechanical means (e.g., through recrystallization and secondary recrystallization) in a bulk sample, and a bimodal grain size distribution can even be produced by consolidating a simple mixture of powders of pre-selected, different grain size. (ii) Also note that a functionally gradient material with a combination of good strength and ductility is beneficial for fatigue performance. There are also some inconveniences: the exact distributions of the grain size, grain shape, and spatial locations depend on many processing parameters and may be difficult to reproduce each time, and the overall material response hence becomes tricky to predict/model. The outcome properties therefore span a relatively wide range depending on the microstructural variations.

(II) Mixture of two or multiple phases with varying size scales and properties.

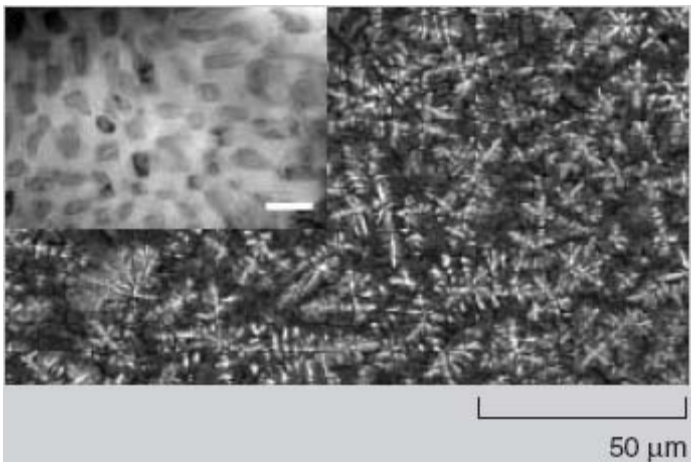

Figure 2.20 A scanning-electron microscope image of an in-situ composite formed via liquid casting of a titanium alloy. The matrix has a rod eutectic microstructure with eutectic spacing less than 100nm (see the TEM micrograph in the inset; the white scale bar represents 100nm). Embedded in the matrix are dendritic primary body-centered cubic titanium solid solution micrometers in size.[92]

A composite microstructure, wherein micrometer-sized ductile phase embedded in an ultra-strong (but brittle) eutectic product with UFG/NC spacing, was formed in-situ during casting (solidification) of the corresponding liquid titanium alloy. As perhaps expected, the microstructure shown in Fig.2.20 simultaneously provided impressive strength due to the large number of interfaces, a high strain hardening rate due to the dislocation accumulation in the micrometer-sized dendrites, and large plastic strains due to the large number of slip bands and profuse dislocation activities.

(III) Using nanoscale growth twins in lieu of the nanograins for strengthening.

It has been argued that a coherent twin boundary, while not much of a defect in terms of interface (grain boundary) energy, is very effective in blocking dislocations to require high stresses for slip transmission across this special grain boundary. Meanwhile, the twin boundaries do not encourage dynamic recovery as general high-angle grain boundaries or dislocation cells do. Dislocations accumulated in regions where the twin spacing is large, the thin twin ribbons were cut into pieces by dislocations tangles, and the twin boundaries had large numbers of dislocations and eventually became dislocation sources. In other words, the originally low defect content (with only coherent, low-energy twin boundaries) saved room for dislocation storage to further strengthen the material upon tensile straining.

(IV) Involving dispersions of nanoparticles and nano-precipitates.

Precipitation hardening is in fact the most potent strengthening method for many alloys. In UFG/NC grains, especially those on the larger side (on the order of 100nm), the hard precipitates also initiate, drag, and pin dislocations such that dynamic recovery

is reduced. Stress concentration is restrained during mechanical loading. The result is a significant dislocation storage required for compatible plastic strains, allowing a high strain-hardening rate that leads to larger uniform strains while elevating strength. Other dual phase microstructures, such as those in steels involving ultrafine martensites, are also advantageous in offering a good combination of strength and ductility.

(V) Using transformation-induced plasticity (TRIP) and twinning-induced plasticity (TWIP).

In tensile deformation, martensitic transformation was reported in UFG steel, at a rate similar to that in its CG counterpart so that the strain-hardening rate is also almost identical. Twinning-induced plasticity in some materials of low stacking fault energy is also likely. A very high density of extremely thin twins, often only two to several atomic layers thick, is observed in the tensile-tested UFG/NC cobalt sample. Some mechanical twinning and twin boundary migration may be ongoing to contribute to strength and strain hardening, although the majority of these observed twins must be growth twins formed during deposition of this metal of low stacking-fault energy.

(VI) Lowering of dynamic recovery at low-temperature (cryogenic temperatures) and/or dynamic strain rates.

In addition to tailoring the microstructure, changing deformation conditions, such as lowering dynamic recovery at low-temperature and dynamic strain rates, is known for CG face-centered cubic (FCC) metals and has been demonstrated to be applicable for UFG/NC FCC metals produced by SPD.

(VII) Improving strain rate hardening from the Hart's instability criterion.

A material with strain rate sensitivity, m, of the order of unity could be superplastic. For FCC metals, going to the UFG/NC grain size does increase the strain rate sensitivity, especially at slow strain rates where grain boundary mechanisms help mediate deformation. Several reports also suggest that after many SPD rounds, copper, titanium, and aluminum alloys appear to show enhanced ductility. The reasons are yet to be fully clarified, but the refined grain sizes and the highly non-equilibrium grain boundary structures may be promoting grain boundary deformation mechanisms, which offer a relatively high m. As a result, uniform tensile deformation is stabilized to relatively large strains.

(VIII) Strive for truly flaw-free materials.

Porosity in consolidated UFG/NC materials may lower strength and help initiate shear localization; this may be partly responsible for the high propensity for shear banding in irradiated alloys or consolidated UFG/NC metals. Therefore, striving for truly flow-free materials is the paramount requirement for enhancing ductility.

2.4 Research Progress of Harmonic-structured Metals

Recently, ball milling has been widely exploited for the synthesis of various nanomaterials, nanograins, nanoalloy, nanocomposites and nano-quasicrystalline materials. The kinetics of mechanical milling or alloying depends on the energy transferred to the powder from the balls during milling. The energy transfer is governed by many parameters such as the type of mill, the powder supplied to drive the milling

chamber, milling speed, size and size distribution of the balls, dry or wet milling, temperature of milling and the duration of milling. [109]

Moreover, it is reported that a surface layer (called transfer layer) with grain size of 3~30nm was observed after ball milling. The thickness of transfer layers may range from several to tens of mm. The adjacent region consists of subgrains and cells of 0.2~0.4mm range. The transfer layer and the block materials below it are separated by a sharply defined interface. It is reported that the formation of an equiaxed nanograined structure in the milled powders occurs because of the grain sub-division and rotation of the elongated grains. The formation of the nanograins depends on the stacking fault energy, since dislocation accumulation by milling is extremely important for the grain sub-division. Thus the nanograined regions appear near the surface of powder and are separated from the interior deformed structured region with sharp boundaries. [40, 110-112]

Thus, Professor Ameyama and co-workers proposed to create a novel microstructure design called “harmonic structure” based on ball milling and subsequent powder metallurgy methods. Effectively, this is a “nano and heterogeneous bimodal structure” consisting of coarse-grained areas (or “cores”) enclosed in a three-dimensional continuously connected network of ultrafine-grained structure (or “shell”). The proposed PM process consists of controlled mechanical milling (MM) of powders followed by their consolidation, see Fig.2.21. [113] The MM of powders is controlled in such a way that the UFG/NC area forms near the surface of the powder particles, which is separated from the interior by a rather sharp boundary. Harmonic-structured pure Ti [114] and alloy Ti-6Al-4V [115], Cu [116] as well as tow-phase stainless steel [117] demonstrated a combination of much higher strength and elongation almost as high as

that of their CG counterparts. In summary, the “harmonic structure” appears to be a remarkable design for improving the mechanical properties of materials. [118,119]

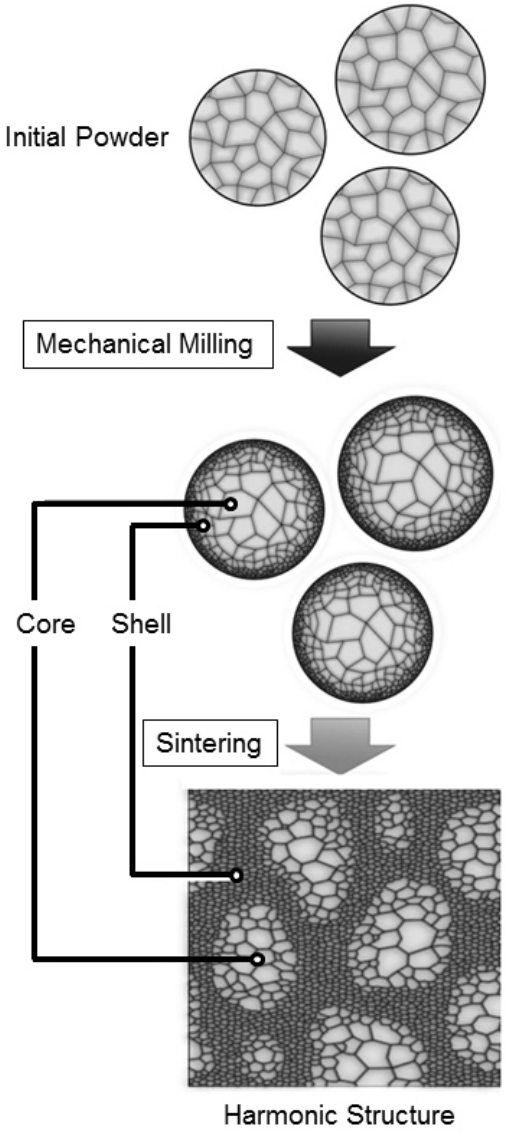

Figure 2.21 Schematic of “harmonic structure designed” materials fabrication process. [113]

References

[1] A.M. Helmenstine, Why is stainless steel stainless? (last accessed 12.25 2013).

[2] Nickel Institute, What is stainless steel? (last accessed 12.25 2013).

[3] Central State Industry, Stainless steel selection guide, (last accessed 12.25 2013).

[4] Stainless Plate Product Inc., White paper-stainless steel, (last accessed 12.25 2013).

[5] British Stainless Steel Association, The basics about stainless steel, (last accessed 12.25 2013).

[6] J. Davis, *ASM specialty handbook: Stainless steels*, ASM International, Materials Park OH, 1994.

[7] H. Cohrt and M. Enders, Sintered steel and iron, Ullmann's encyclopedia of industrial chemistry, A24 (1993), 185-204.

[8] L. Antony and R. Reddy, Processes for production of high-purity metal powders, JOM, 55 (2003), 14-18.

[9] E. Klar and P. Samal, *Powder metallurgy stainless steels: Processing, microstructures, and properties*, ASM International, Materials Park OH, 2007, 23-38.

[10] J. Dunkley and J. Palmer, Factors affecting particle size of atomized metal powders, Powder Metallurgy, 4 (1986) 287-290.

[11] A. Ankus and R. Venter, The water atomization of silver: Effect of pressure and superheat, Powder Technology, 73 (1992) 169-179.

[12] J. Hamill, C. Schade and N. Myers, Water atomized fine powder technology. Proceedings of 2000 Powder Metallurgy World Congress, Kyoto, Japan, JPMA Ed., 2000, 367-370.

[13] L. Nyborg, T. Tunberg and P. Wang, Surface product formation during water atomization and sintering of austenitic stainless steel powder, Metal Powder Report, 45 (1990) 750-753.

[14] H. Karlsson, L. Nyborg and S. Berg, Surface chemical analysis of prealloyed water atomised steel powder, Powder Metallurgy, 48 (2005) 51-58.

[15] H. Karlsson, L. Nyborg and R. Frykholm, Surface reactions during fabrication and sintering of 410L stainless steel powder, Powder Metallurgy Progress, 5 (2005) 220-233.

[16] A. Krajnikov, M. Gastel and H. Ortner, Surface characterisation of water-atomised Al–Zn–Mg–Cu alloy powders by SIMS and AES, Mikrochimica Acta, 138 (2002) 1-12.

[17] M. Hohmann and S. Pleier, Production methods and applications for high-quality metal powders and sprayformed products, Acta Metallurgica Sinica, 18 (2005), 15-23.

[18] S. Hariprasad and S. Sastry, Processing maps for optimizing gas atomization and spray deposition, JOM, 47 (1995) 56-59.

[19] N. Ashgriz, *Handbook of atomization and sprays: Theory and applications*, Springer, New York, 2011, 837-848.

[20] J. Dunkley, *Atomization, ASM Handbook: Powder metal technologies and applications*, ASM International, Materials Park OH, 7 (1998) 35-52.

[21] F. Biancaniello, J. Conway, P. Espina, G. Mattingly and S. Ridder, Particle size measurement of inert-gas-atomized powder, Materials Science and Engineering A, 124 (1990) 9-14.

[22] S. Osella, S. Ridder, F. Biancaniello and P. Espina, The intelligent control of an inert-gas atomization process, JOM, 43 (1991) 18-21.

[23] D. Tourret, G. Reinhart, C. Gandin, G. Iles, U. Dahlborg, M. Calvo-Dahlborg and C. Bao, Gas atomization of Al-Ni powders: Solidification modeling and neutron

diffraction analysis, Acta Materialia, 59 (2011) 6658-6669.

[24] Y. Feng and T. Qiu, Preparation, characterization and microwave absorbing properties of FeNi alloy prepared by gas atomization method, Journal of Alloys and Compounds, 513(2012) 455-459.

[25] O. Neikov, S. Naboychenko and I. Mourachova, *Handbook of non-ferrous metal powders: Technologies and applications*, Elsevier, Oxford, 2009, 317-321.

[26] R. Kumagae, Operating practice in plasma rotating electrode process, Metal Powder Report, 53 (1998) 34-34.

[27] S. Miller and P. Roberts, "Rotating Electrode Process", *Powder metal technologies and applications*, ASM handbook-Volume7, S. Lampman et.al. eds., ASM International, Materials Park OH, 1998, 97-101.

[28] M. Nishida, Y. Morizono, T. Kai, J. Sugimoto, A. Chiba and R. Kumagae, Microstructure dependence of compactibility of rapidly solidified Ti-rich TiAl alloy powders produced by plasma rotating electrode process, Materials Transaction, 38 (1997) 334-343.

[29] V. Moxson, O. Senkov and F. Froes, Innovations in titanium powder processing, JOM, 52 (2000) 24-26.

[30] M. Entezarian, F. Allaire, P. Tsantrizos and R. Drew, Plasma atomization: A new process for the production of fine, spherical powders, JOM, 48 (1996) 53-55.

[31] L. Nyborg, M. Norell and I. Olefjord, Surface studies of powder metallurgical stainless steel, Surface and Interface Analysis, 19 (1992) 607-614.

[32] I. Olefjord and L. Nyborg, Surface analysis of gas atomized ferritic steel powder, Powder Metallurgy, 28 (1985) 237-243.

[33] E. Hryha, C. Gierl, L. Nyborg , H. Danninger and E. Dudrov, Surface composition

of the steel powders pre-alloyed with manganese, Applied Surface Science, 256 (2010) 3946-3961.

[34] P. Bracconi and G. Gasc, Surface characterization and reactivity of a nitrogen atomized 304L stainless steel powder, Metallurgy and Materials Transaction A, 25A (1994) 509-520.

[35] A. Ozols, H. Sirkin and E. Vicente, Segregation in Stellite powders produced by the plasma rotating electrode process, Materials Science and Engineering A, 262 (1999) 64-69.

[36] N. Bekoz and E. Oktay, High temperature mechanical properties of low alloy steel foams produced by powder metallurgy, Materials & Design, 53 (2014) 482-489.

[37] R. Farnish, P. Kulkarni, R. Berry, M. Bradley and V. Guillebert, Testing of powders for sensitivity to air effect segregation, Powder Metallurgy, 54 (2011) 468-470.

[38] E. Hall, The deformation and ageing of mild steel: III Discussion of results, Proceedings of the Physical Society London, B64 (1951) 747-753.

[39] N. Petch, The cleavage strength of polycrystals, Journal of the Iron and Steel Institute, 174 (1953) 25-28.

[40] M. Umemoto, Nanocrystallization of steels by severe plastic deformation, Materials Transactions, 44 (2003) 1900-1911.

[41] S. Kolpakov, V. Parshin and A. Chekhovoi, Nanotechnology in the metallurgy of steel, Steel in Translation, 37 (2007) 716-721.

[42] M. Meyers, A. Mishra and D. Benson, Mechanical properties of nanocrystalline materials, Progress in Materials Science 51 (2006) 427-556.

[43] C. Koch, “Nanostructured Materials: An Overview”, *Bulk nanostructured materials* M. Zehetbauer and Y. Zhu eds, WILEY-VCH, Weinheim, 2009, 3-19.

[44] R. Valiev, R. Islamgaliev and I. Alexandrov, Bulk nanostructured materials from severe plastic deformation, Progress in Materials Science, 45 (2000) 103-189.

[45] V. Stolyarov, Y. Zhu, I. Alexandrov, T. Lowe and R. Valiev, Influence of ECAP routes on the microstructure and properties of pure Ti, Materials Science and Engineering A, 299 (2001) 59-67.

[46] Y. Zhao, X. Liao, Z. Jin, R. Valiev and Y. Zhu, Microstructures and mechanical properties of ultrafine grained 7075 Al alloy processed by ECAP and their evolutions during annealing, Acta Materialia, 52 (2004) 4589-4599.

[47] R. Valiev, Y. Estrin, Z. Horita, T. Langdon, M. Zechetbauer and Y. Zhu, Producing bulk ultrafine-grained materials by severe plastic deformation, JOM, 58 (2006) 33-39.

[48] V. Pushin, V. Stolyarov, R. Valiev, T. Lowe and Y. Zhu, Nanostructured TiNi-based shape memory alloys processed by severe plastic deformation, Materials Science and Engineering A, 410-411 (2005) 386-389.

[49] R. Lapovoka, R. Cottama, P. Thomsona and Y. Estrin, Extraordinary superplastic ductility of magnesium alloy ZK60, Journal of Materials Research, 20 (2005) 1375-1378.

[50] H.□Kim, W.□Ryu, M. Janecek, S.□Baik and Y. Estrin, Effect of equal channel angular pressing on microstructure and mechanical properties of IF steel, Advanced Engineering Materials, 7 (2005) 43-46.

[51] S. Divinski, J. Ribbe, D. Baither, G. Schmitz, G. Reglitz, H. Rösner, K. Sato, Y. Estrin and G. Wilde, Nano-and micro-scale free volume in ultrafine grained Cu-1wt.%Pb alloy deformed by equal channel angular pressing, Acta Materialia, 57 (2009) 5706-5717.

[52] N. Kobelev, E. Kolyvanov and Y. Estrin, Temperature dependence of sound attenuation and shear modulus of ultra fine grained copper produced by equal channel angular pressing, Acta Materialia, 56 (2008) 1473-1481.

[53] C. Huang, G. Yang, Y. Gao, S. Wu and Z. Zhang, Influence of processing temperature on the microstructures and tensile properties of 304L stainless steel by ECAP, Materials Science and Engineering A, 485 (2008) 643-650.

[54] S. Qu, C. Huang, Y. Gao, G. Yang, S. Wu, Q. Zang and Z. Zhang, Tensile and compressive properties of AISI 304L stainless steel subjected to equal channel angular pressing, Materials Science and Engineering A, 475 (2008) 207-216.

[55] A. Zhilyaev, G. Nurislamova, B. Kim, M. Baro, J. Szpunard and T. Langdon, Experimental parameters influencing grain refinement and microstructural evolution during high-pressure torsion, Acta Materialia, 51 (2003) 753-765.

[56] G. Sakai, Z. Horita and T. Langdon, Grain refinement and superplasticity in an aluminum alloy processed by high-pressure torsion, Materials Science and Engineering A, 393 (2005) 344-351.

[57] G. Sakai, K. Nakamura, Z. Horita and T. Langdon, Developing high-pressure torsion for use with bulk samples, Materials Science and Engineering A, 406 (2005) 268-273.

[58] K. Edalati, T. Fujioka and Z. Horita, Microstructure and mechanical properties of pure Cu processed by high-pressure torsion, Materials Science and Engineering A, 497 (2008) 168-173.

[59] K. Edalati and Z. Horita, High-pressure torsion of pure metals: Influence of atomic bond parameters and stacking fault energy on grain size and correlation with hardness, Acta Materialia, 59 (2011) 6831-6836.

[60] Y. Saito, H. Utsunomiya, N. Tsuji and T. Sakai, Novel ultra-high straining process for bulk materials-development of the accumulative roll-bonding (ARB) process, Acta Materialia, 47 (1999) 579-583.

[61] N. Tsuji, Y. Saito, S. Lee and Y. Minamino, ARB (accumulative roll-bonding) and other new techniques to produce bulk ultrafine grained materials, Advanced Engineering Materials, 5 (2003) 338-344.

[62] X. Huang, N. Hansen and N. Tsuji, Hardening by annealing and softening by deformation in nanostructured metals, Science, 312 (2006) 249-251.

[63] X. Huang, N. Tsuji, N. Hansen and Y. Minamino, Microstructural evolution during accumulative roll-bonding of commercial purity aluminum, Materials Science and Engineering A, 340 (2003) 265-271.

[64] N. Tsuji, R. Ueji and Y. Minamino, Nanoscale crystallographic analysis of ultrafine grained IF steel fabricated by ARB process, Scripta Materialia, 47 (2002) 69-76.

[65] S. Ohsaki, S. Kato, N. Tsuji, T. Ohkubo and K. Hono, Bulk mechanical alloying of Cu-Ag and Cu/Zr two-phase microstructures by accumulative roll-bonding process, Acta Materialia, 55 (2007) 2885-2895.

[66] C. Koch, Synthesis of nanostructured materials by mechanical milling: problems and opportunities, Nanostructured Materials, 9 (1997) 13-22.

[67] C. Koch and Y. Cho, Nanostructure formation by mechanical attrition, Nanostructured Materials, 6 (1995) 33-42.

[68] D. Zhang, Processing of advanced materials using high-energy mechanical milling, Progress in Materials Science, 49 (2004) 537-560.

[69] C. Koch, K. Youssef and R. Scattergood, Mechanical properties of nanocrystalline materials produced by in situ consolidation ball milling, Materials Science Forum,

579 (2008) 15-28.

[70] X. Zhang, H. Wang, M. Kassem, J. Narayan and C. Koch, Preparation of bulk ultrafine-grained and nanostructured Zn, Al and their alloys by in situ consolidation of powders during mechanical attrition Scripta materialia, 46 (2002) 661-665.

[71] V. Tellkamp, E. Lavernia and A. Melmed, Mechanical behavior and microstructure of a thermally stable bulk nanostructured Al alloy, Metallurgical and Materials Transactions A, 32 (2001) 2335-2343.

[72] R. Hayes, R. Rodriguez and E. Lavernia, The mechanical behavior of a cryomilled Al-10Ti-2Cu alloy, Acta Materialia, 49 (2001) 4055-4068.

[73] F. Zhou, X. Liao, Y. Zhu, S. Dallek and E. Lavernia, Microstructural evolution during recovery and recrystallization of a nanocrystalline Al-Mg alloy prepared by cryogenic ball milling, Acta Materialia, 51 (2003) 2777-2791.

[74] A. Zuniga, L. Ajdelsztajn and E. Lavernia, Spark plasma sintering of a nanocrystalline Al-Cu-Mg-Fe-Ni-Sc alloy, Metallurgical and Materials Transactions A, 37 (2006) 1343-1352.

[75] E. Lavernia, B. Han and J. Schoenung, Cryomilled nanostructured materials, processing and properties, Materials Science and Engineering A, 493 (2008) 207-214.

[76] B. Verlinden, Severe plastic deformation of metals, Proc. 2nd International Conference on Deformation Processing and Structure of Materials pages, 2005 3-18.

[77] B. Kashyap and K. Tangri, On the Hall-Petch Relationship and substructural evolution in type 316L, Acta Metallurgy Materials, 43 (1995) 3971-3981.

[78] X. Chen, J. Lu, L. Lu and K. Lu, Tensile properties of a nanocrystalline 316L austenitic stainless steel, Scripta Materialia, 52 (2005) 1039-1044.

[79] N. Tsuji, N. Kamikawa, R. Ueji, N. Takata, H. Koyama and D. Terada, Managing both strength and ductility in ultrafine grained steels, ISIJ International, 48 (2008) 1114-1121.

[80] Y. Wang and E. Ma, "Mechanical properties of bulk nanostructured metals", *Bulk nanostructured materials* M. Zehetbauer and Y. Zhu eds, WILEY-VCH, Weinheim, 2009, 425-450.

[81] H. Höppel, H. Mughrabi, and A. Vinogradov, "Fatigue properties of bulk nanostructured materials", *Bulk nanostructured materials* M. Zehetbauer and Y. Zhu eds, WILEY-VCH, Weinheim, 2009, 481-498.

[82] T. Langdon, "Superplasticity of bulk nanostructured materials", *Bulk nanostructured materials* M. Zehetbauer and Y. Zhu eds, WILEY-VCH, Weinheim, 2009, 455-468.

[83] Y. Zhu, B. Han and E. Lavernia, "Deformationmechanisms of nanostructured materials", *Bulk nanostructured materials* M. Zehetbauer and Y. Zhu eds, WILEY-VCH, Weinheim, 2009, 89-108.

[84] C. Koch, Optimization of strength and ductility in nanocrystalline and ultrafine grained metals, Scripta Materialia, 49 (2003) 657-662.

[85] E. Ma, Instabilities and ductility of nanocrystalline and ultrafine-grained metals, Scripta Materialia, 49 (2003) 663-668.

[86] I. Ovid'ko and T. Langdon, Enhanced ductility of nanocrystalline and ultrafine-grained metals, Reviews on Advanced Materials Science, 30 (2012) 103-111.

[87] I. Ovid'ko and A. Sheinerman, Ductile vs. brittle behavior of pre-cracked nanocrystalline and ultrafine-grained materials, Acta Materialia, 58 (2010)

5286-5294.

[88] Z. Lee, V. Radmilovic, B. Ahn, E. Lavernia and S. Nutt, Tensile deformation and fracture mechanism of bulk bimodal ultrafine-grained Al-Mg alloy, Metallurgical and Materials Transactions A, 41A (2010) 795-801.

[89] Y. Zhao, J. Bingert, Y. Zhu, X. Liao, R. Valiev, Z. Horita, T. Langdon, Y. Zhou and E. Lavernia, Tougher ultrafine grain Cu via high-angle grain boundaries and low dislocation density, Applied Physics Letters, 92 (2008) 081903.

[90] X. Zhang, H. Wang and C. Koch, Mechanical behavior of bulk ultrafine-grained and nanocrystalline Zn, Reviews on Advanced Materials Science, 6 (2004) 53-93.

[91] Y. Wang, E. Ma, Three strategies to achieve uniform tensile deformation in a nanostructured metal, Acta Materialia, 52 (2004) 1699-1709.

[92] E. Ma, Eight routes to improve the tensile ductility of bulk nanostructured metals and alloys, JOM, 58 (2006) 49-53.

[93] Y. Wang, M. Chen, F. Zhou and E. Ma, High tensile ductility in a nanostructured metal, Nature, 419 (2002) 912-915.

[94] B. Kumar and D. Raabe, Tensile deformation characteristics of bulk ultrafine-grained austenitic stainless steel produced by thermal cycling, Scripta Materialia, 66 (2012) 634-637.

[95] H. Azizi-Alizamini, M. Militzer and W. Poole, A novel technique for developing bimodal grain size distributions in low carbon steels, 57 (2007) 1065-1068.

[96] G. Dirras, J. Gubicza, S. Ramtani, Q. Bui and T. Szilágyi, Microstructure and mechanical characteristics of bulk polycrystalline Ni consolidated from blends of powders with different particle size, Materials Science and Engineering A, 527 (2010) 1206-1214.

[97] S. Ramtani, G. Dirras and H. Bui, A bimodal bulk ultra-fine-grained nickel: Experimental and micromechanical investigations, Mechanics of Materials, 42 (2010) 522-536.

[98] M. Haouaoui, I. Karaman, H. Maier and K. Hartwig, Microstructure evolution and mechanical behavior of bulk copper obtained by consolidation of micro-and nanopowders using equal-channel angular extrusion, Metallurgical and Materials Transactions A, 32A (2004) 2935-2949.

[99] B. Srinivasarao, K. Oh-ishi, T. Ohkubo, T. Mukai and K. Hono, Synthesis of high-strength bimodally grained iron by mechanical alloying and spark plasma sintering, Scripta Materialia, 58 (2008) 759-762.

[100] T. Sasaki, T. Ohkubo and K. Hono, Microstructure and mechanical properties of bulk nanocrystalline Al-Fe alloy processed by mechanical alloying and spark plasma sintering, Acta Materialia, 57 (2009) 3529-3538.

[101] B. Srinivasarao, K. Oh-ishi, T. Ohkubo and K. Hono, Bimodally grained high-strength Fe fabricated by mechanical alloying and spark plasma sintering, Acta Materialia, 57 (2009) 3277-3286.

[102] O. Ertorer, T. Topping, Y. Li, W. Mossb and E. Lavernia, Enhanced tensile strength and high ductility in cryomilled commercially pure titanium, Scripta Materialia, 60 (2009) 586-589.

[103] D. Witkin, Z. Lee, R. Rodriguez, S. Nutt and E. Lavernia, Al-Mg alloy engineered with bimodal grain size for high strength and increased ductility, Scripta Materialia, 49 (2003) 297-302.

[104] Z. Lee, D. Witkin, V. Radmilovic, E. Lavernia and S. Nutt, Bimodal microstructure and deformation of cryomilled bulk nanocrystalline Al-7.5Mg alloy,

Materials Science and Engineering A, 410-411 (2005) 462-467.

[105] B. Han, E. Lavernia1 and F. Mohamed, Mechanical properties of nanostructued materials, Reviews on Advanced Materials Science, 9 (2005) 1-16.

[106] B. Han, E. Lavernia, Z. Lee, S. Nutt and D. Witkin, Deformation behavior of bimodal nanostructured 5083 Al alloys, Metallurgical and Materials Transactions A, 36 (2005) 957-965.

[107] Z. Lee, V. Radmilovic, B. Ahn, E. Lavernia, and S. Nutt, Tensile deformation and fracture mechanism of bulk bimodal ultrafine-grained Al-Mg alloy, Metallurgical and Materials Transactions A, 41A (2010) 795-801.

[108] Q. Bui, Heterogeneous plastic deformation in bimodal bulk ultrafine-grained nickel, Journal of Materials Science, 47 (2012) 1902-1909.

[109] T. Yadav, R. Yadav and D. Singh, Mechanical milling: a top down approach for the synthesis of nanomaterials and nanocomposites, Nanoscience and Nanotechnology, 2 (2012) 22-48.

[110] H. Fujiwara, H. Inomoto, R. Sanada and K. Ameyama, Nano-ferrite formation and strain-induced-ferrite transformation in an SUS316L austenitic stainless steel, Scripta Materialia, 44 (2001) 2039-2042.

[111] K. Ameyama, Low temperature recrystallization and formation of an ultrafine (γ +σ) microduplex structure in a SUS316L stainless steel, Scripta Materialia, 38 (1998) 517-522.

[112] E. Oda, K. Ameyama and S. Yamaguchi, Fabrication of nano grain tungsten compact by mechanical milling process and its high temperature properties, Materials Science Forum, 503-504 (2006) 573-578.

[113] K. Ameyama, T. Sekiguchi, H.Fujiwara, Z. Zhang, Microstructure and mechanical

properties of hetero-structure metallic materials produced by harmonic structure design, Tetsu to Hagane-Journal of the Iron and Steel Institute of Japan, 98 (2012) 739-744. (in Japanese)

[114] T. Sekiguchi, K. Ono, H. Fujiwara and K. Ameyama, New microstructure design for commercially pure titanium with outstanding mechanical properties by mechanical milling and hot roll sintering, Materials Transactions, 51 (2010) 39-45.

[115] H. Fujiwara, T. Sekiguchi and K. Ameyama, Mechanical properties of pure titanium and Ti-4Al-4V alloys with a new tailored nano/meso hybrid microstructure, International Journal of Materials Research, 100 (2009) 796-799.

[116] D. Orlov, H. Fujiwara and K. Ameyama, Obtaining copper with harmonic structure for the optimal balance of structure-performance relationship, Materials Transactions, 54 (2013) 1549-1553.

[117] O. Ciuca, M. Ota, S. Deng and K. Ameyama, Harmonic structure design of a SUS329J1 two phase stainless steel and its mechanical properties, Materials Transactions, 54 (2013) 1629-1633.

[118] H. Fujiwara, T. Kawabata, H. Miyamoto and K. Ameyama, Mechanical properties of harmonic structured composite with pure titanium and Ti48 at%Al alloy by MM/SPS process, Materials Transactions, 54 (2013) 1619-1623.

[119] K. Ameyama and H. Fujiwara, Creation of harmonic structure materials with outstanding mechanical properties, Materials Science Forum, 706-709 (2012) 9-16.

Chapter 3 Experimental Procedure

Figure 3.1 shows the experimental procedure applied in the present dissertation and the details are described in the following section:

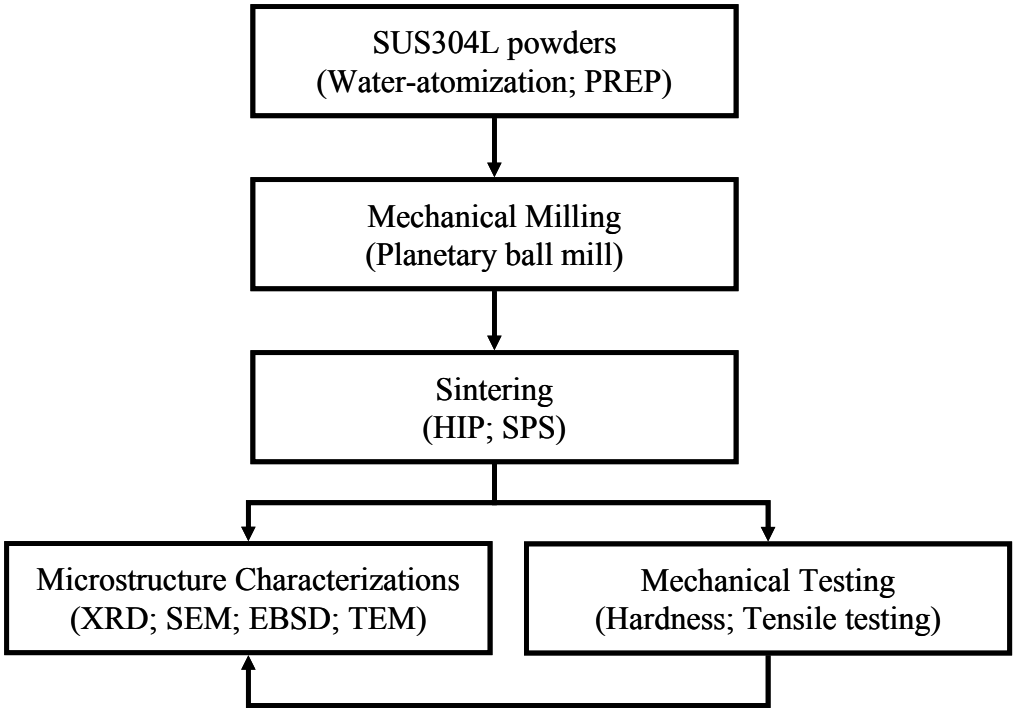

Figure 3.1 Flow chart of study on microstructure and mechanical properties in this dissertation.

3.1 Mechanical milling (MM)

There are a number of different types of mills for conducting mechanical milling (MM), such as mixer mills, planetary mills, attritors and uni-ball mill. These mills differ in their capacity, speed of operation, and their ability to control the operation by varying the temperature of milling and the extent of minimizing the contamination of the

powders. Planetary ball mill is a most frequently used system for mechanical milling since only a very small amount of powder is required. Therefore, the system is particularly suitable for research purpose in the laboratory. The ball mill system consists of one turn disc (turn table) and two or four bowls. The turn disc rotates in one direction while the bowls rotate in the opposite direction. The centrifugal forces, created by the rotation of the bowl around its own axis together with the rotation of the turn disc, are applied to the powder mixture and milling balls in the bowl. The powder mixture is fractured and cold welded under high energy impact. [1]

In the present study, mechanical milling process on SUS304L powders was carried out using a planetary ball mill (Fritsch P-5) manufactured by Fritsch GmbH in Germany. The view of equipment and schematic depicting the ball motion inside the ball mill is presented in Fig.3.2a and Fig.3.2b, respectively. Conditions of mechanical milling are listed in Table 3.1.

Table 3.1 Mechanical milling conditions

Powder		SUS304L PREP	SUS304L Water-atomization
		approximately 120μm	approximately 80μm
Ball	Composition	SUS304	
	Diameter	5.0mm	10.0mm
	Weight	400g	
Weight ratio (Ball : Powder)		2:1	
Rotation speed		200rpm	
MM time		180ks, 360ks	36ks, 108ks
Atmosphere		Ar	

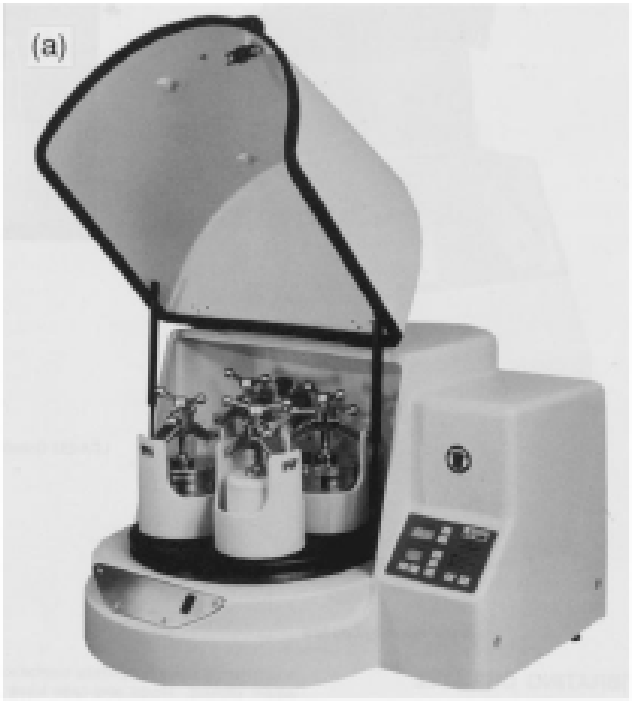

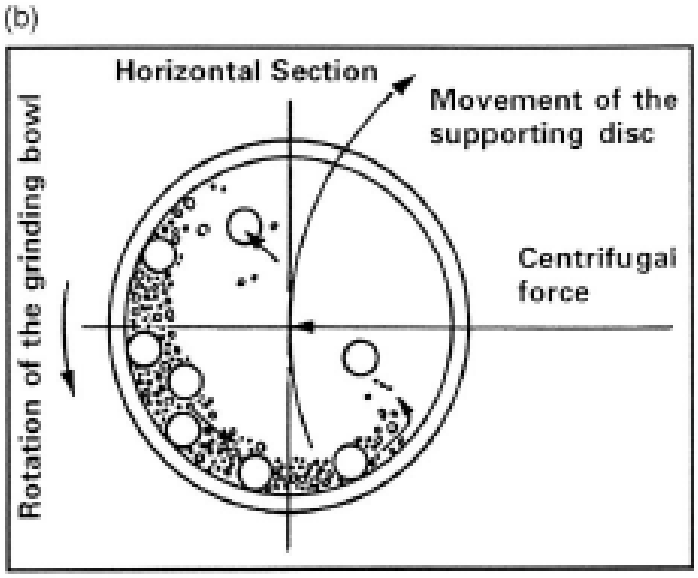

Figure 3.2 (a) Fritsch P-5 four station ball mill. (b) Schematic depicting the ball motion inside the ball mill. [1]

3.2 Sintering

3.2.1 Spark Plasma Sintering (SPS)

Spark plasma sintering (SPS) is a newly developed sintering process that combines the use of mechanical pressure and microscopic electric discharge between the particles. The enhance densification in this process has been attributed to localized self-heat generation by the discharge, activation of the particle surfaces, and the high speed of mass and heat transfer during the sintering process. As a result, samples can rapidly reach full density at relatively low temperature. [2] The schematic of SPS process is indicated in Fig.3.3.

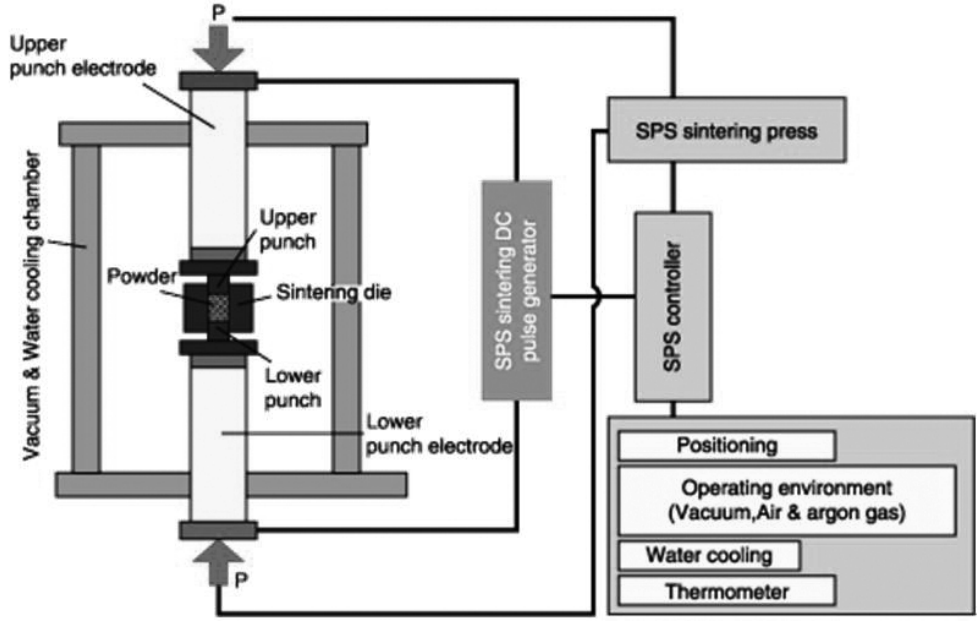

Figure 3.3 Schematic diagram of SPS process.

Spark plasma sintering (DR. SINTER 1020, Sumitomo) was applied to sinter the powders under 50MPa for 3.6ks at 1173K. The shape and dimension of graphite punch and die and sintering process are shown in Fig.3.4. The sintering parameters of SPS are presented in Table 3.2.

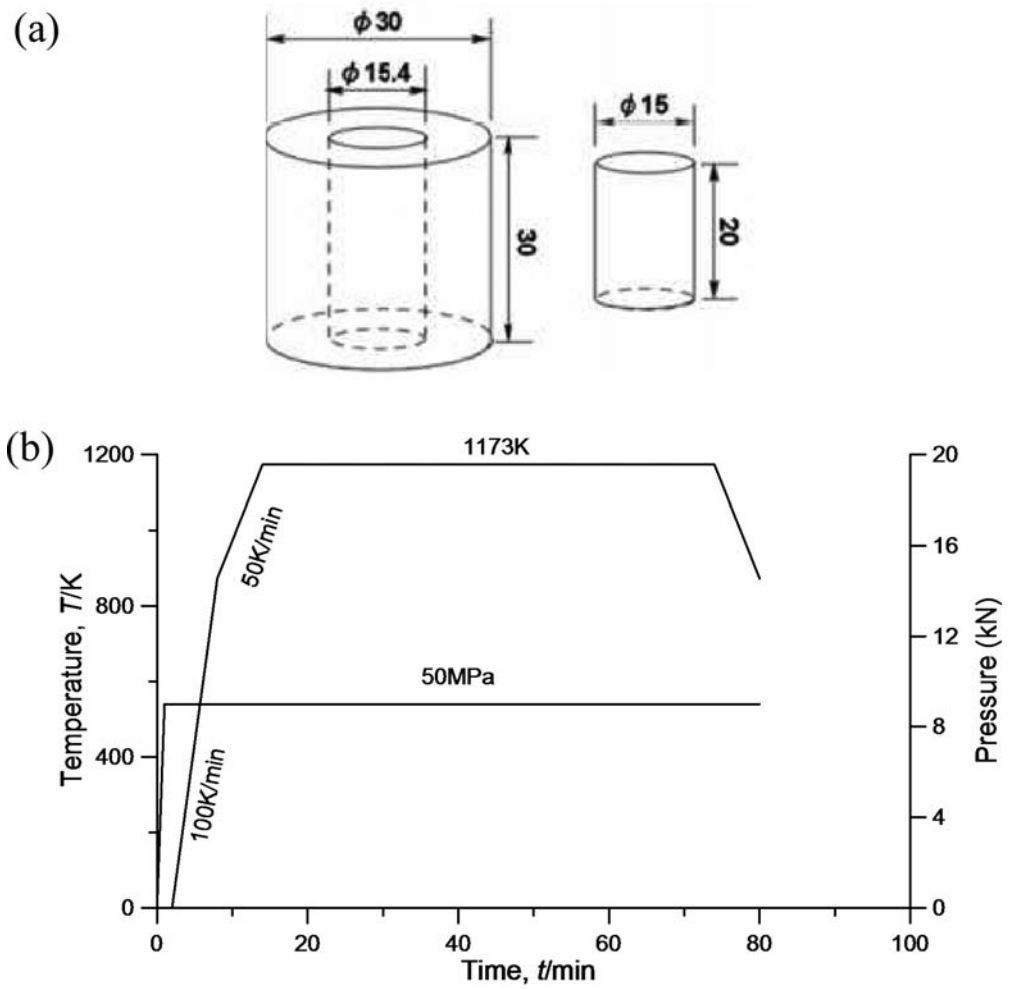

Figure 3.4 (a) Shape and dimension of graphite punch and die; (b) Spark plasma sintering process.

Table 3.2 Spark plasma sintering conditions

Sintering method	Spark plasma sintering
Powders	SUS304L PREP
Temperature	1173K
Heating rate	<873K 100K/min >873K 50K/min
Pressure	50MPa
Dwell time	3.6ks
Atmosphere	Vacuum (under 15Pa)
Cooling	Furnace

3.2.2 Hot Isostatic Pressing (HIP)

Hot isostatic pressing (HIP) is a material pressing technique in which high isostatic pressure is applied to a powder part or compact at elevated temperature to produce particle bonding. This process usually results in the manufacture of a fully dense body. During this process, the compact is subjected to equal pressure from every side. HIP is used for dense high performance ceramics, to remove porosity from castings, the consolidation of PM materials and surface coatings, diffusion bonding and improvement of weld integrity. [3] The schematic of HIP equipment is indicated in Fig.3.5.

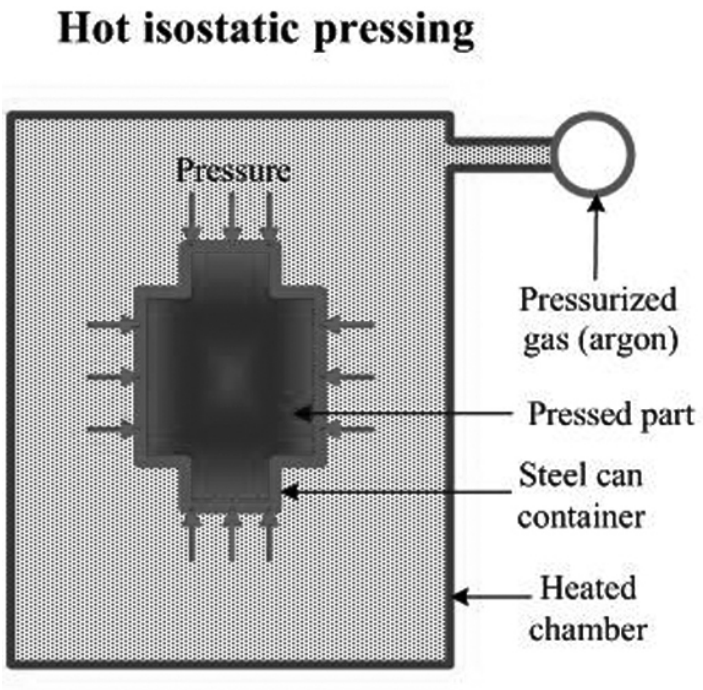

Figure 3.5 Schematic diagram of HIP process.

In this study, the container for HIP process is made of mild steel, and the dimension and sintering process are shown in Fig.3.6. After filled with MM powders, the cover and container were welded by Tosei Electrobeam Co., Ltd. and then the HIP process was

carried out by Kinzoku Giken Co., Ltd. The sintering parameters of HIP are presented in Table 3.3.

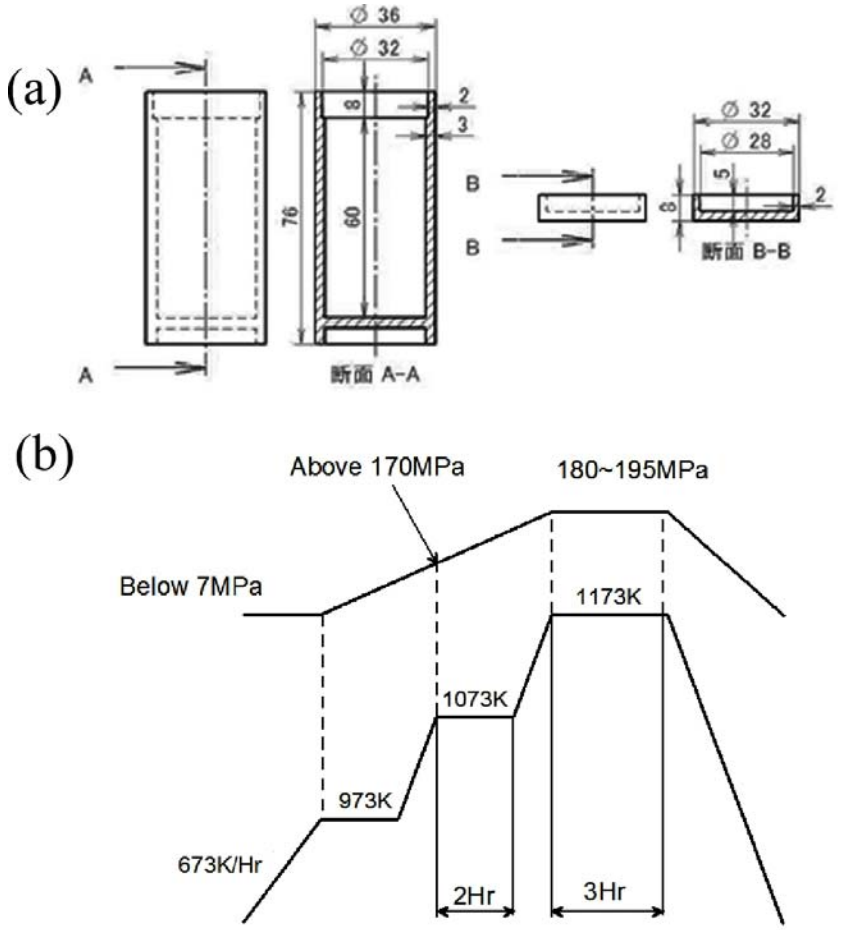

Figure 3.6 (a) Shape and dimension of HIP container; (b) Hot isostatic pressing sintering process.

Table 3.3 Hot isostatic pressing sintering conditions

Sintering method	Hot Isostatic Pressing
Powders	SUS304L water-atomization
Temperature	1173K
Heating rate	1.67K/ks
Pressure	200MPa
Dwell time	5.4ks
Atmosphere	Ar

3.3 Characterizations

3.3.1 X-ray Diffraction (XRD)

X-ray diffraction (XRD) is one of the most important tools of solid-state chemistry, since it constitutes a powerful and readily available method for determining atomic arrangements in matter. When an X-ray beam falls on matter, scattered X-radiation is produced by all the atoms. These scattered waves spread out spherically from all the atoms in the sample, and the interference effects of the scattered radiation from the different atoms cause the intensity of the scattered radiation to exhibit maxima and minima in various directions. [4] Schematic of X-ray diffraction is shown in Fig.3.7.

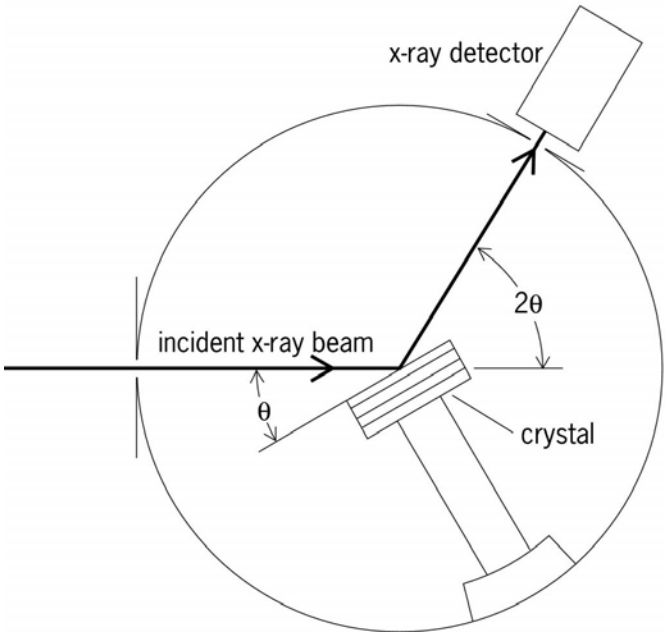

Figure 3.7 Schematic of X-ray diffraction. [4]

Powders and sintered compacts were analyzed by XRD-6000 (Shimadzu) in the present study. Surface of sample was mechanical polished fixed at sample holder for XRD analysis. The tests parameters are shown in Table 3.4.

Table 3.4 X-ray diffraction conditions

Target		CuKα
Measuring		continuous
Measurement axis		2θ/θ
X-ray tube voltage		40kv
X-ray tube current		20mA
Start angle		30°
Finish angle		100°
Sampling angle		0.0020°
Scan speed		1.000°/min
Slit setting	Divergent slit	1°
	Scattered slit	1°
	Optical slit	0.15mm

3.3.2 Scanning Electron Microscopy (SEM)

Scanning electron microscope (SEM) is a type of electron microscope that produces images of a sample by scanning it with a focused beam of electrons. The electrons interact with atoms in the sample, producing various signals that can be detected and that contain information about the sample's surface topography and composition. The electron beam is generally scanned in a raster scan pattern, and the beam's position is combined with the detected signal to produce an image. SEM can achieve resolution better than 1 nanometer. Specimens can be observed in high vacuum, in low vacuum, and in wet conditions. Schematic of SEM is shown in Fig.3.8. [5]

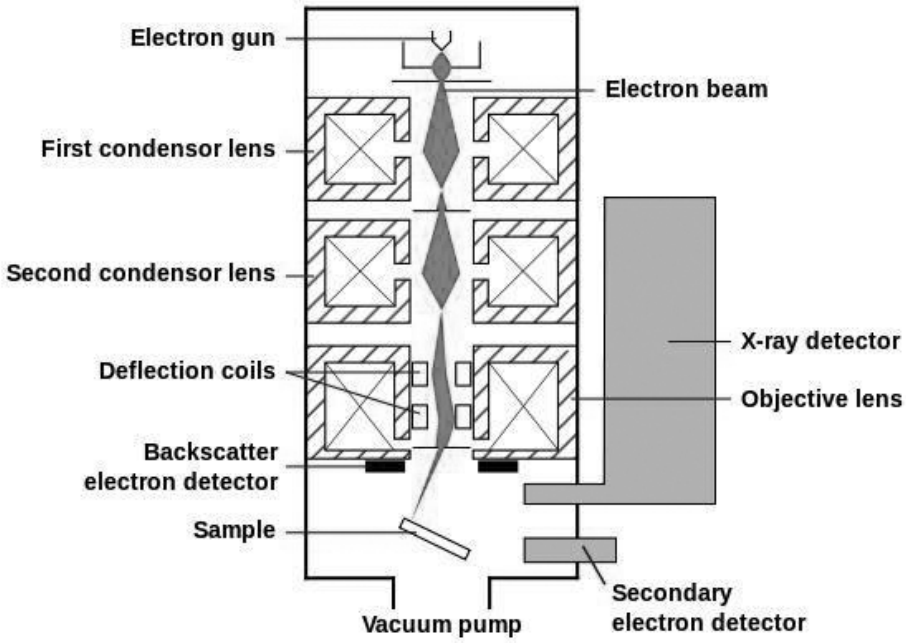

Figure 3.8 Schematic of scanning electron microscopy. [5]

SEM observations were conducted for the appearance and cross-section of the powder before and after mechanical milling, as well as the compacts consolidated by HIP or SPS process. SEM JSM-6400 (Jeol) was operated at 20kV in this thesis. The powders were conglutinated on the carbon tape, and appearance was observed directly. The powders were mounted in the epoxy, and then after mechanical polished and etched, the samples were carried out gold evaporation when observing the cross-section of powders.

The samples for SEM observation were mechanical polished using SiC papers on the polishing unit (Struers). Firstly, the specimen surface was ground from 80 to 2000 grit SiC paper respectively. Next, the specimens were buffed with 1μm Al_2O_3 suspension. Subsequently, specimens were mechanical grinding by OP-S suspension (Struers). OP-S suspension is a colloidal silica suspension for final polishing, which consists of negatively charged particles of silicon dioxide (SiO_2) with a pH value 9.8 and a grain size of about 0.04μm. After polishing with this solution, the sample surface is slightly

etched and the deformation layer during mechanical polishing is therefore removed. Finally, the prepared specimens were washed in an ultrasonic bath.

The samples were etched by copper sulfate solution or HCl/HNO_3 solution for SEM observation in the present study. $CuSO_4$ solution is common etching solution for ordinary stainless steels. HCl/HNO_3 solution is used for slight etching and the microstructure was observed by backscatter electron images (BEI). The composition of $CuSO_4$ solution and HCl/HNO_3 solution is show in Table 3.5 and Table 3.6, respectively.

Table 3.5 Composition of $CuSO_4$ solution

H_2O	50ml
C_2H_5OH	50ml
HCl	50ml
$CuSO_4$	10g
Mixture time	10s

Table 3.6 Composition of HCl/HNO_3 solution

CH_3OH	20ml
HCl	45ml
HNO_3	15ml
Mixture time	10s

3.3.3 Electron Backscatter Diffraction (EBSD)

Electron backscatter diffraction (EBSD) based on scanning electron microscopy (SEM) is a powerful technique to automatically and quantitatively measure the grain/subgrain size, local texture, point-to-point orientations, strain and phase identification. It has been established that EBSD has a lot of advantages over transmission electron microscopy (TEM), such as simple sample preparation, automatic

scanning and indexing, ultra-fast speed, large area investigation and a lot of postprocessing results derived from one EBSD scan. [6]

For an EBSD measurement a flat/polished crystalline specimen is placed in the SEM chamber at a highly tilted angle (~70° from horizontal) towards the diffraction camera, to increase the contrast in the resultant electron backscatter diffraction pattern. The phosphor screen is located within the specimen chamber of the SEM at an angle off approximately 90° to the pole piece and is coupled to a compact lens which focuses the image from the phosphor screen onto the CCD camera. In this configuration, some of the electrons which enter the sample backscatter and may escape. As these electrons leave the sample, they may exit at the Bragg condition related to the spacing of the periodic atomic lattice planes of the crystalline structure and diffract. These diffracted electrons can escape the material and some will collide and excite the phosphor causing it to fluoresce (Fig.3.9). [7]

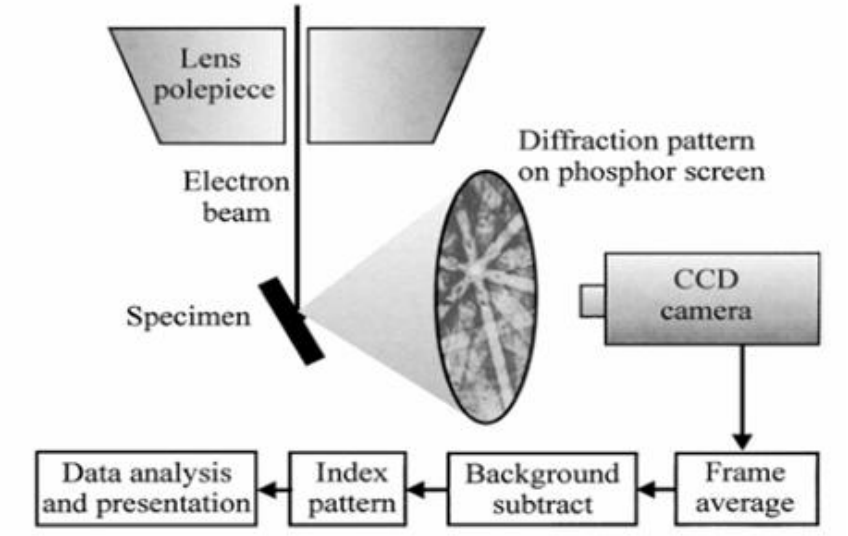

Figure 3.9 The basic set-up of electron backscatter diffraction [7]

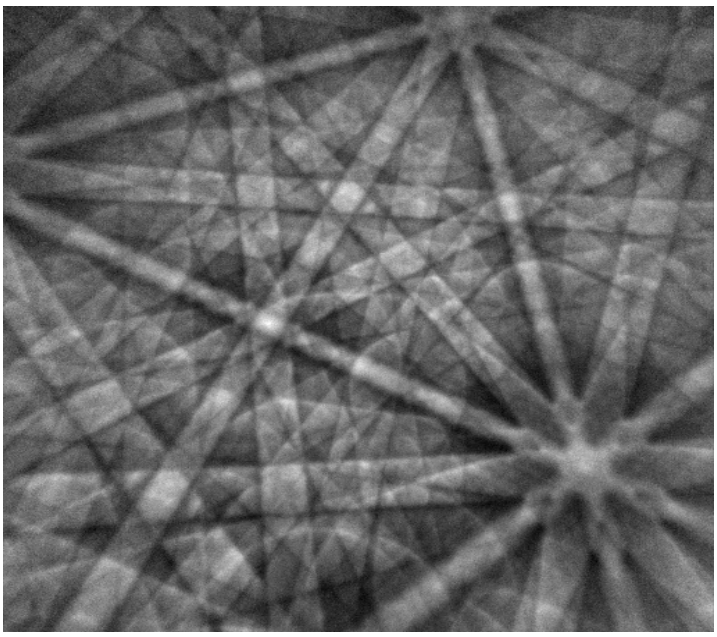

Figure 3.10 Kikuchi electron backscatter diffraction pattern.

An electron backscatter diffraction pattern (EBSP) is formed when many different planes diffract different electrons to form Kikuchi bands which correspond to each of the lattice diffracting planes (Fig.3.10). If the system geometry is well described, it is possible to relate the bands present in the EBSP to the underlying crystal phase and orientation of the material within the electron interaction volume.

For EBSD analysis, specimens were mechanical grinding by OP-S suspension (Struers). The EBSD microstructure observations were carried out in a FE-SEM Hitachi SU6600 microscope fitted with HKL NordlysMax electron backscatter diffraction (EBSD) detector. Postprocessing is carried out using the CHANNEL5 software (Oxford Instrument, Abington, Oxfordshire). In addition, EBSD technique was utilized for the quantitative analysis of microstructure. Hereafter, term “grain” will refer to crystallite areas predominantly surrounded by boundaries with misorientation angle $\theta \geq 15°$.

3.3.4 Transmission Electron Microscopy (TEM)

Transmission electron microscopy (TEM) is a microscopy technique in which a beam of electrons is transmitted through an ultra-thin specimen, interacting with the specimen as it passes through. An image is formed from the interaction of the electrons transmitted through the specimen; the image is magnified and focused onto an imaging device, such as a fluorescent screen, on a layer of photographic film, or to be detected by a sensor such as a CCD camera. The basic set-up of transmission electron microscopy is shown in Fig.3.11.

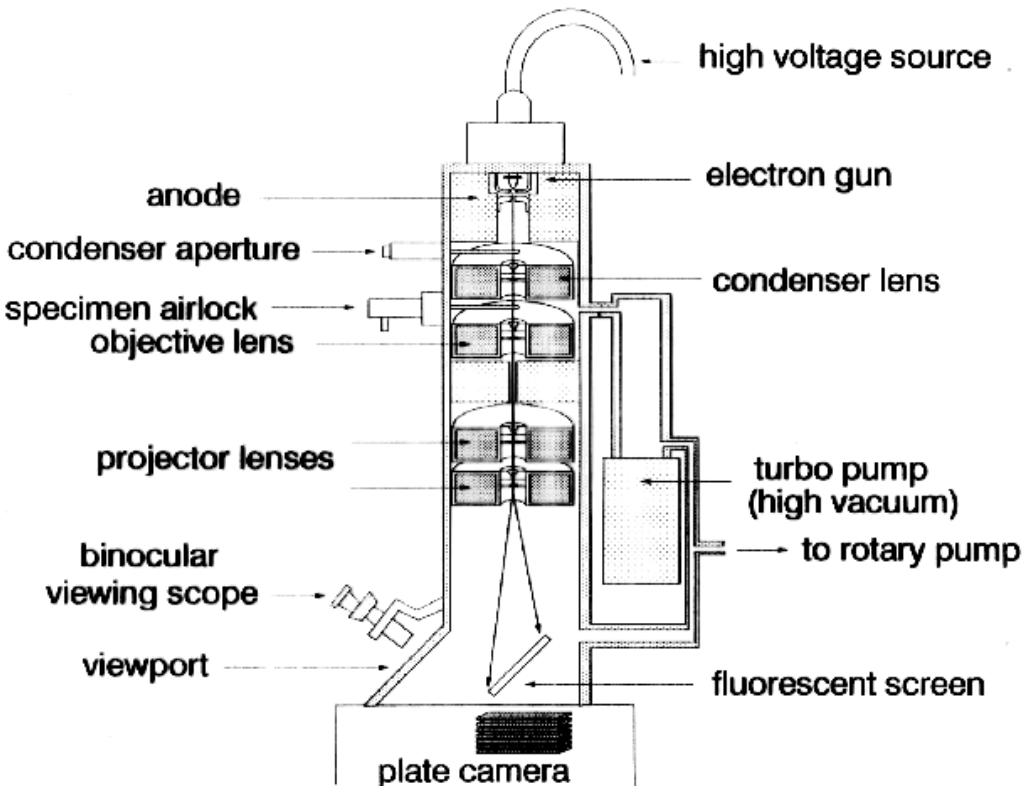

Figure 3.11 The basic set-up of transmission electron microscopy [8]

For TEM observation, the samples were machined to ϕ3 by wire-cut (Hitachi) and

prepared by mechanical grinding to below 200μm thickness. Then specimens were thinned by twin-jet electro-polishing (Tenupol-5 Struers), the conditions of twin-jet electron-polishing are shown in Table 3.7. TEM observation was also carried out by TEM JEM-2010 (Jeol) at 200kV.

Table 3.7 Twin-jet electron-polishing conditions

Electron-polishing solution	Solution	CH_3COOH-60%$HClO_4$
	Volume ratio	9:1
	Temperature	281K（8℃）
Appliance	Voltage	20V
	Time	∞

3.4 Mechanical Properties

3.4.1 Vickers Hardness Test

Hardness of specimens was measured using micro hardness tester (HMV-1, Shimadzu) based on Vickers indentation. Samples for hardness test were polished and etched, the hardness of coarse-grained region and ultrafine-grained region was measured respectively.

As illustrated in Fig.3.12, Vickers ranges use a 136° pyramidal diamond indenter that forms a square indent. The indenter is pressed into the sample by an accurately controlled test force. The force is maintained for a specific dwell time, normally 5~15s. After the dwell time is complete, the indenter is removed leaving an indent in the sample that appears square shaped on the surface. The size of the indent is determined optically by measuring the two diagonals of the square indent. The Vickers hardness number is a function of the test force divided by the surface area of the indent. The

average of the two diagonals is used in the following formula to calculate the Vickers hardness. [9] The Vickers hardness test condition is shown in Table 3.8.

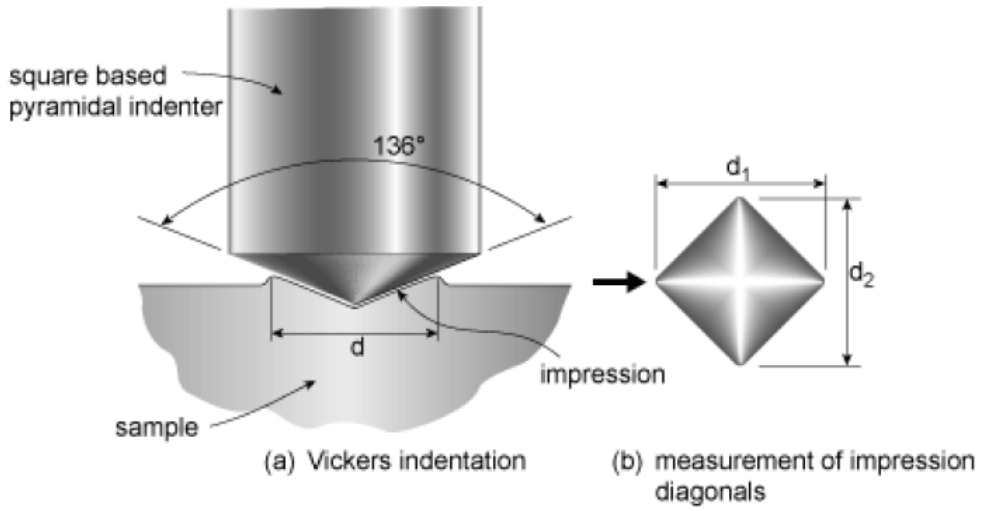

Figure 3.12 Principle of Vickers hardness test

HV = Constant × test force/indent diagonal squared

Table 3.8 Vickers hardness test conditions

Dwell time	5s
Load	0.98N (0.1HV)
HV/HK	HV

3.4.2 Tensile Test

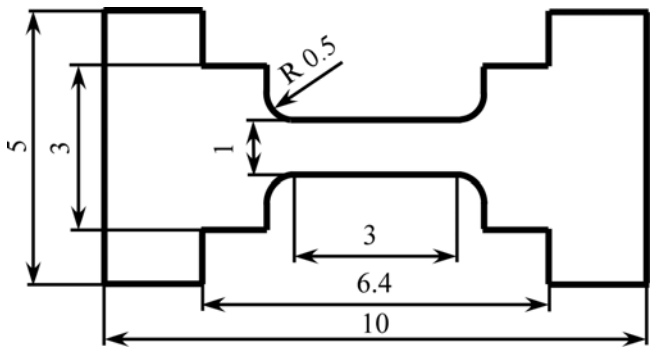

Figure 3.13 The dimension of tensile specimen.

Tensile experiments were conducted in a universal testing machine (Autograph AGS-10kND, Shimadzu), under displacement control. The specimens for tensile tests were machined by wire-spark cutting to a gauge length of 3mm and a cross-section area of $1\times1mm^2$ (Fig. 3.13) at a nominal strain rate of 5.56×10^{-4} s^{-1} (a cross-head speed of 0.1mm/min). The tensile specimens were machined from different sintered compacts and tensile tests were repeated at least four times under each condition. A non-contact extensometer based on CCD camera system was used to measure the strain during tensile tests. Due to the small gauge length of the tensile specimen, the measurement of elastic deformation was rough, so the elastic deformation was removed from stress-strain curves. The tensile test condition is listed in Table 3.9.

Table 3.9 Tensile test conditions

Gauge length (mm)	Gauge width (mm)	Gauge thickness (mm)	Head speed (mm/min)	Nominal strain rate (1/s)
3	1	1	0.1	5.56×10^{-4}

References

[1] C. Suryanarayana, Mechanical alloying and milling, Progress in Materials Science, 46 (2001) 1-184.

[2] Y. Gogoti editor, Nanomaterials Handbook, Published by CRC Press, 2006, 364-365

[3] C. Tam, S. Lee, S. Chang, T. Tang, H. Ho and H. Bor, Effects of the temperature of hot isostatic pressing treatment on Cr-Si targets, Ceramics International 35 (2009) 565-570.

[4] Dictionary, Mc-Graw-Hill Concise Encyclopedia of Physics, The McGraw-Hill

Companies.Inc, 2002.

[5] http://en.wikipedia.org/wiki/Scanning_electron_microscope, (last accessed 12.25 2013).

[6] Y. Chen, J. Hjelen and H. Roven, Application of EBSD technique to ultrafine grained and nanostructured materials processed by severe plastic deformation: Sample preparation, parameters optimization and analysis, Transaction Nonferrous Metals Society of China, 22 (2012) 1801-1809.

[7] F. Humphreys, Review grain and subgrain characterization by electro backscatter diffraction, Journal of Materials Science, 36 (2001) 3833-3854.

[8] http://digitalespiegelreflexkamerass.com/transmission-electron-microscope/, (last accessed 12.25 2013).

[9] http://www.instron.us/wa/applications/test_types/hardness/vickers.aspx, (last accessed 12.25 2013).

Chapter 4 Microstructure and Mechanical Properties of SUS304L Compacts with Harmonic Structure

4.1 Introduction

SUS304 is the most common of austenitic grades, containing approximately 18% chromium and 8% nickel. “L” means low carbon content, which can provide extra corrosion after welding. Owing to the excellent corrosion resistance, oxidation resistance as well as non-magnetic, SUS304L stainless steel has been used widely for chemical processing equipment, for food, dairy, and beverage industries, for heat exchangers, and for the milder chemicals. However, the low yield strength is the major drawback. Grain refinement has been applied to strengthen metals. However, plastic instability condition tends to be achieved in the early stage of tensile deformation, which leads to inadequate ductility. The idea of bimodal grain size distribution is an effective method to improve ductility, wherein ultrafine grains provide strength while coarse grains contribute to ductility. This idea is simple and easy to be synthesized by traditional themo-mechanical processing and sintering a mixture of as pre-selected metal powders. However, the exact UFG and CG spatial distribution is difficult to control in mentioned synthesis process. Therefore, “harmonic structure design” is applied to improve the mechanical properties of SUS304L stainless steel.

As described in Chapter 2, plasma rotating electrode process (PREP) is a commercial method to produce high purity metal powders. The PREPed powders are characterized by higher purity, low oxygen content and perfectly spherical powders. The present chapter deals with the fabrication and characterization of harmonic structure in SUS304L stainless steel using the powder metallurgy approach, which involves the mechanical milling of the PREPed powders followed by their consolidation using spark plasma sintering (SPS). The microstructural characteristics and mechanical properties of the "harmonic structure designed" SUS304L steels are presented and discussed. The effect of milling time on the grain size and relative volume fractions of the core and the shell areas is studied. Finally, the effect of core/shell volume fractions on the mechanical properties of the harmonic-structured compacts is presented and compared to those of "homogeneous" CG and UFG bulks.

4.2 Experimental Procedure

The SUS304L steel powder, prepared by plasma rotating electrode process (PREP), was used as a starting material. The chemical composition of the starting PREPed powder is shown in Table 4.1. Average particle size in the initial powders was approximately 120μm. Mechanical milling was carried out in a Fritch P-5 planetary ball mill using SUS304 steel vial and balls (5mm diameter). The milling was carried out under argon gas atmosphere at room temperature, wherein the ball-to-powder weight ratio was maintained at 2:1. The powder mixture was milled for 180ks and 360ks at a constant milling speed of 200rpm. Subsequently, the powders were sintered by SPS under 50MPa for 3.6ks at 1173K.

Table 4.1 Chemical composition of PREPed SUS304L powders (mass%).

C	Si	Mn	P	S	Ni	Cr	Fe
0.05	0.28	1.37	0.032	0.025	8.2	18.6	Bal.

The microstructure observations were carried out by scanning electron microscopy (SEM) in a FE-SEM Hitachi SU6600 microscope operating at 20kV. The microscope was fitted with HKL NordlysMax electron backscatter diffraction (EBSD) detector. For SEM analysis, specimens were prepared by mechanical grinding and etched with a solution consisting of 45mL HCl, 15mL HNO_3, and 20mL CH_3OH at room temperature. For EBSD analysis, specimens were mechanical grinding by OP-S suspension (Struers). OP-S suspension is a colloidal silica suspension for final polishing, which consists of negatively charged particles of silicon dioxide (SiO_2) with a pH value 9.8 and a grain size of about 0.04μm. After polishing with this solution, the sample surface is slightly etched and the deformation layer during mechanical polishing is therefore removed. [1] The micrographs were acquired using both secondary and backscattered electron imaging, SE and BSE, respectively. In addition, EBSD technique was utilized for the quantitative analysis of microstructure. Hereafter, term “grain” will refer to crystallite areas predominantly surrounded by boundaries with misorientation angle at least $\theta \geq 15°$. The “grain size” <d> was determined as an equivalent diameter of such areas. Standard metallographic procedures were employed for the SEM and EBSD sample preparation with final polishing using colloidal silica suspension.

The mechanical properties were examined by hardness and tensile tests. The specimens for tensile tests were machined by wire-spark cutting to a gauge length of 3mm and a cross-section area of $1 \times 1 mm^2$. Tensile tests were carried out using a

universal testing machine (AGS-10kND, Shimadzu), at a nominal strain rate of 5.56×10^{-4} s^{-1} (a cross-head speed of 0.1mm/min). A non-contact extensometer based on CCD camera system was used to measure the strain during tensile tests. Due to the small gauge length of the tensile specimen, the measurement of elastic deformation was rough, so the elastic deformation was removed from stress-strain curves. The Vickers Hardness (HV) measurements were carried out using 0.98N load and 5s dwell time.

4.3 Results

4.3.1 Microstructural Characteristics of the Powders

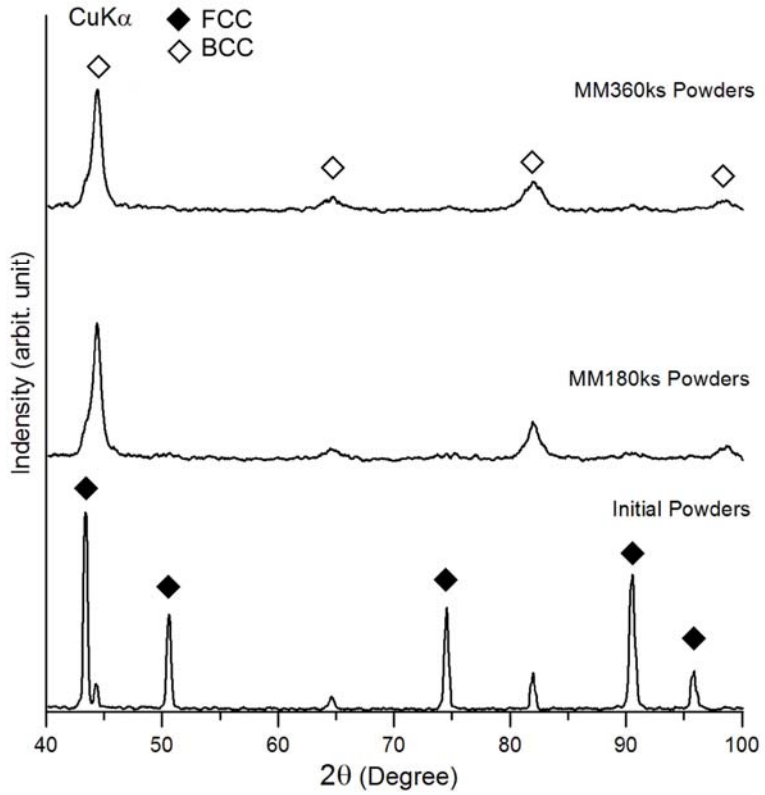

Figure 4.1 XRD results of PREPed SUS304L powders before and after mechanical milling.

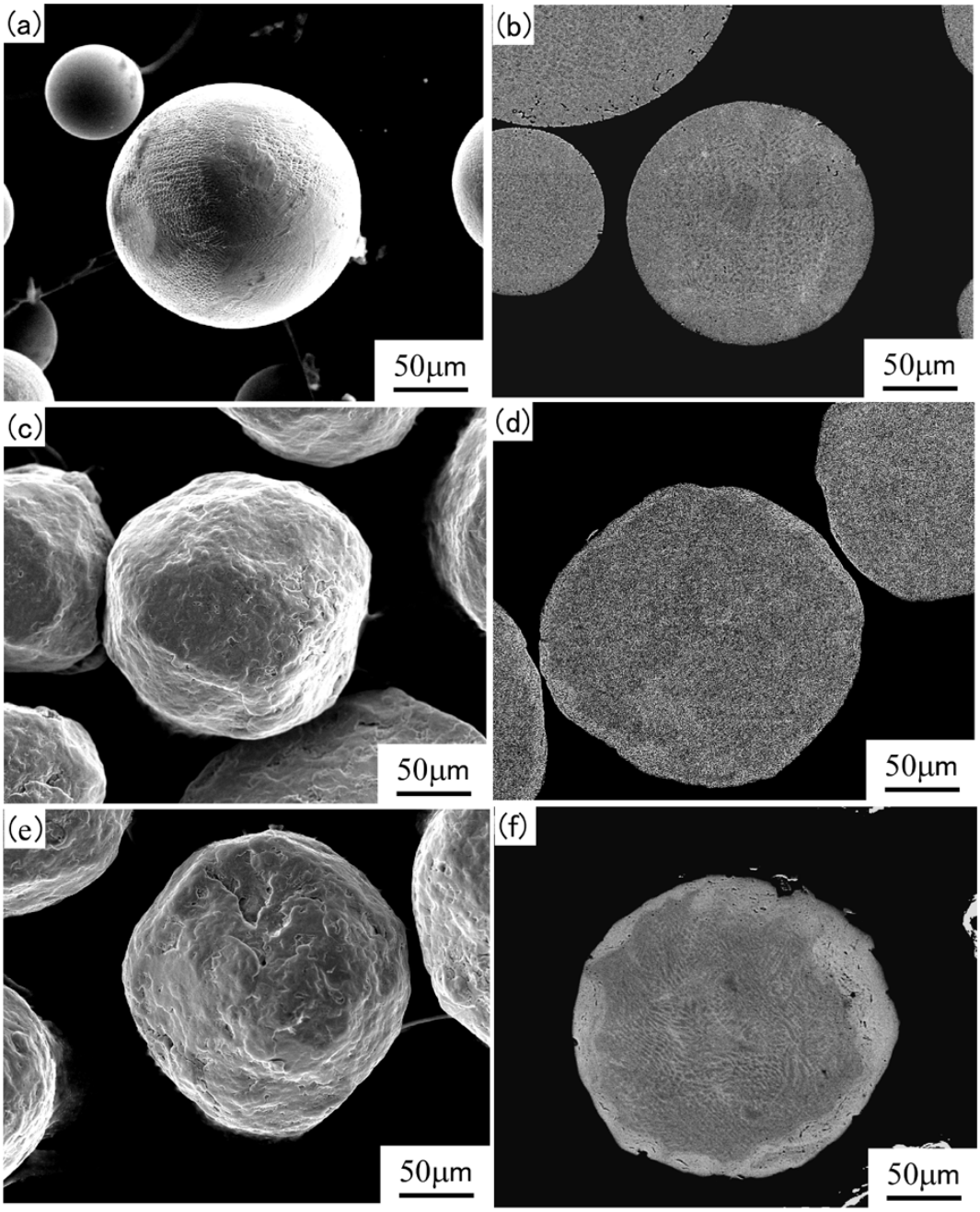

Figure 4.2 SE-SEM micrographs illustrating shape (a,c,e) and BSE-SEM micrographs revealing microstructure (b,d,f) of SUS304L steel powder particulates in the initial condition and after mechanical milling: (a,b) Initial powder; (c,d) MM180ks powder; (e,f) MM360ks powder.

Figure 4.1 shows the XRD results of SUS304L initial powders (IP) and the milled powders. The IP has a mixture of face-centre-cubic (FCC) structure and

body-centre-cubic (BCC) structure. The FCC structure is austenite, while the BCC structure is thought to be δ phase, which was remained in the powders during rapid cooling. By contrast, it is noticed that only BCC structure was shown in the milled powders for 180ks (MM180ks powders) and 360ks (MM360ks powders), which indicates the mechanical milling transformed austenite into martensite near the powder surface.

Figure 4.2 shows the morphology and the microstructure of SUS304L steel powders before and after the milling. The morphology of the initial steel powder particles, powder milled for 180ks and 360ks are shown in Fig.4.2a, 4.2c and 4.2e, respectively. It can be observed that the initial powder has a spherical shape and smooth surface appearance, whereas the milled powders have irregular shape and rough surface. It can also be noticed that the milled powder particles become increasingly distorted with an increase in milling time. It is worth emphasizing that the milling conditions were optimized in such a way that the MM processing did not lead to any fracturing or agglomeration due to cold welding of the powder particles. Therefore, such a change in morphology can be attributed to the increasing levels of accumulated plastic deformation of powder particles with increasing milling time.

The microstructures of the cross-section of the initial powder and the powders milled for 180ks and 360ks are shown in Fig.4.2b, 4.2d and 4.2f, respectively. It can be noticed that the initial powder has rather homogeneous contrast across the entire particle section, while the milled powders demonstrate contrast substantially varying between the periphery and the core areas. Namely, the formation of a thin bright-contrast layer near the surface of the powder particles is evident. Moreover, it can also be noted that the thickness of the surface layer increases with an increase of milling time, compare

Figs.4.2d and 4.2f, while the contrast of the core area does not change appreciably.

4.3.2 Microstructural Characteristics of the Sintered Compacts

Figure 4.3 shows the XRD results of sintered SUS304L compacts. Both the IP compacts and milled powder compacts have a mixture of FCC and BCC structure, which indicates that formed martensite near the milled powder surface was transformed into austenite after sintering, but still a small mount of δ-phase was remained in the sintered compacts.

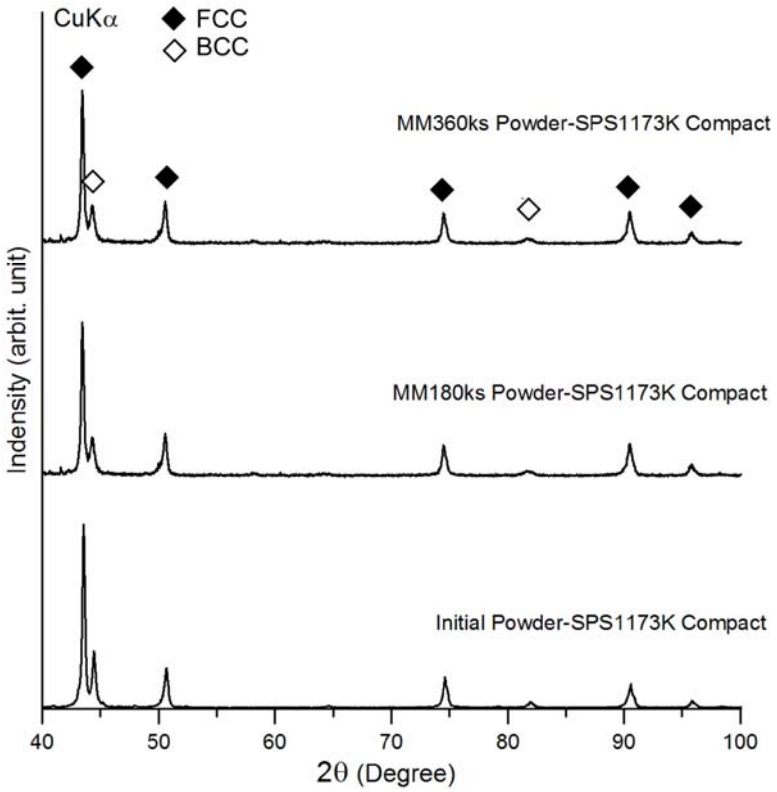

Figure 4.3 XRD results of sintered PREPed SUS304L powder compacts.

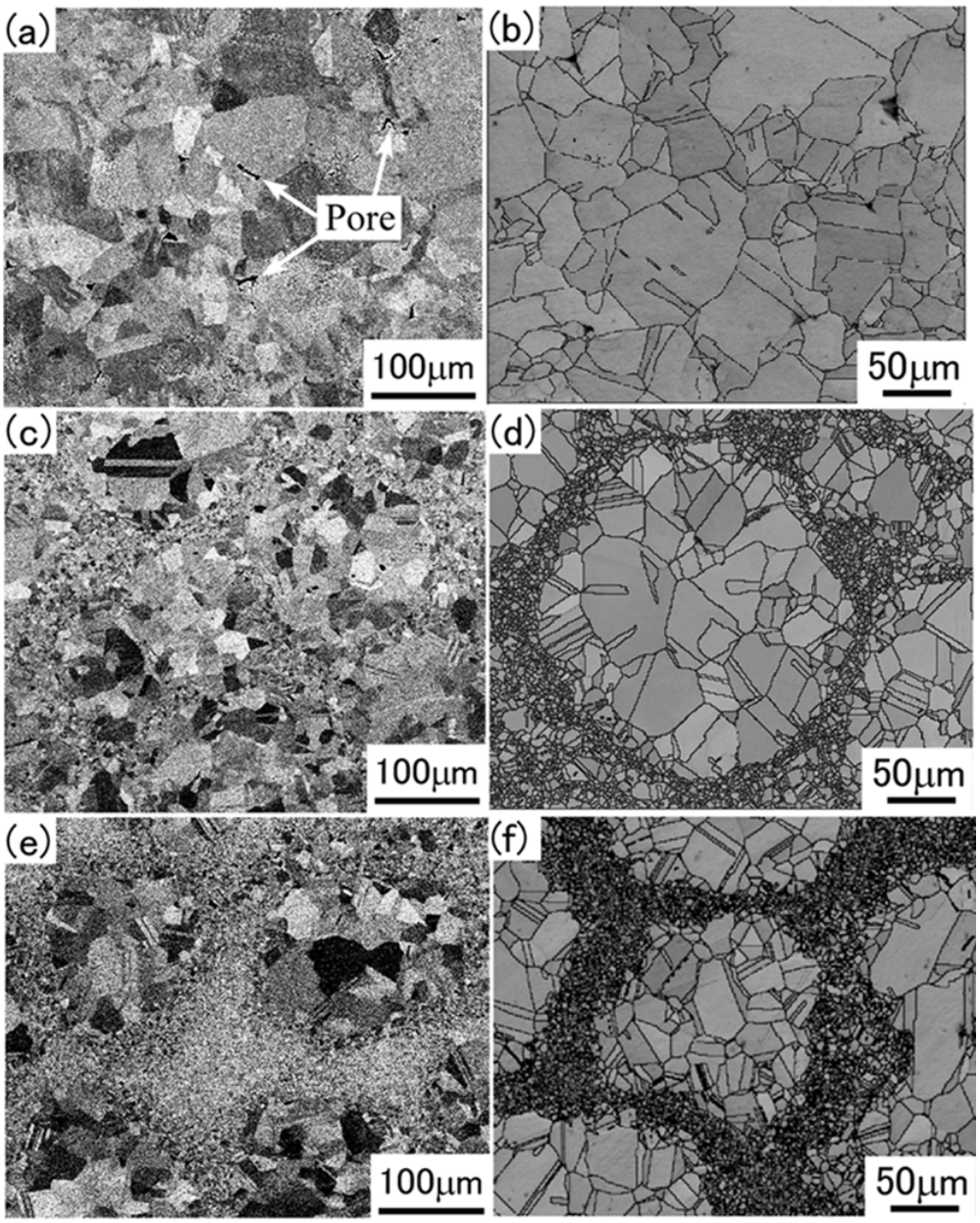

Figure 4.4 Microstructures of SUS304L compacts sintered from (a,b) initial, (c,d) MM180ks, and (e,f): MM360ks powders: (a), (c), (e) are BSE-SEM micrographs, and (b), (d), (f) are EBSD image quality maps overlaid with HABs.

Figure 4.4 shows the microstructure of the sintered SUS304L compacts prepared from the initial and the milled powders. As can be observed in Fig.4.4a, some residual pores remain in the sintered compacts prepared from the initial powder. These are usually attributed to regular spherical shape and a large particle size of a powder [2]. It

can also be clearly observed that a reasonably homogeneous coarse-grained structure, with an average grain size of approximately 19.5μm, is formed in the sintered compacts prepared from the initial powder (Fig.4.4a and 4.4b).

On the contrary, sintering of the milled powders results in near-full density compacts, as can be seen in Figs.4.4c and 4.4e. It can also be noticed that the microstructures of the MM180ks and MM360ks powder compacts consist of two different types of areas: (i) coarse-grained areas, or "core", and (ii) ultrafine-grained areas, or "shell" (Fig.4.4c-f). Furthermore, the sintered compacts prepared from the milled powders have a peculiar microstructure wherein the core areas are enclosed in a three-dimensional continuously connected network of the shell areas, which is termed as "harmonic structure". From Fig.4.4, it can also be noticed that an increasing milling time leads to an increased shell fraction in the sintered compacts (Fig.4.4c-f).

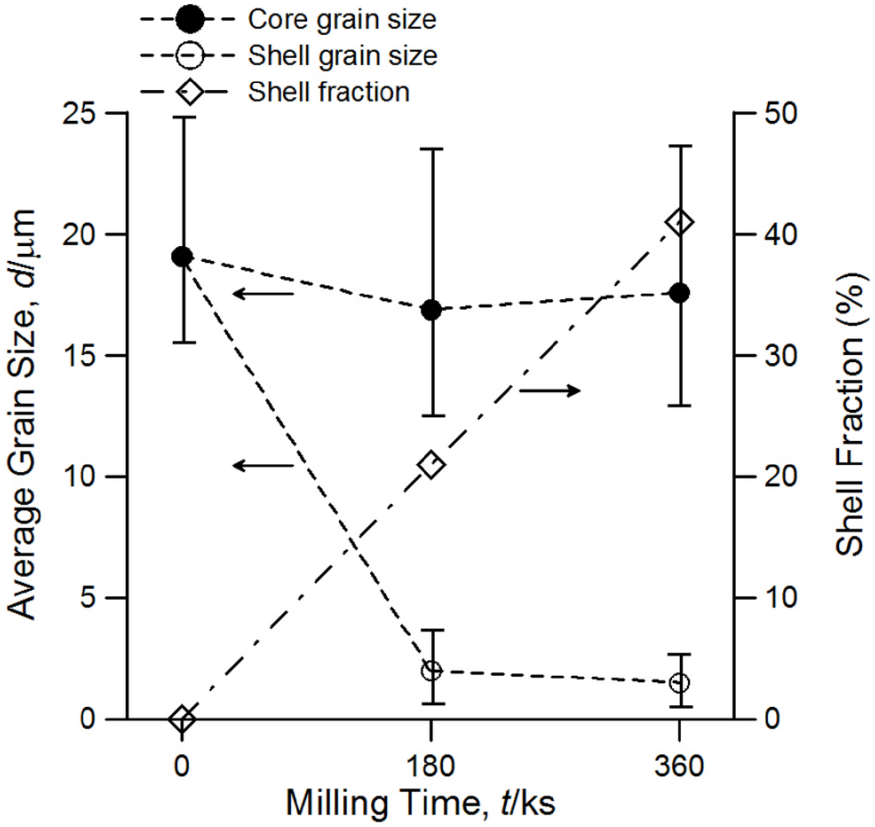

Figure 4.5 Diagram illustrating the dependence of grain size and shell fraction in the sintered SUS304L compacts on the time of mechanical milling.

Figure 4.5 and Table 4.2 summarize quantitatively the effect of milling time on the shell fraction and grain size in the sintered SUS304L compacts. It can be noted that the sintered compacts prepared from the initial powder have a homogeneous microstructure with an average grain size of approximately d_c=19.5μm within 15-25μm variation limits. Mechanical milling of the powders leads to the formation of two distinctly different populations of grain sizes in the final compacts, i.e. the bimodal grain structure consisting of ultrafine-grained "shell" and coarse-grained "core" areas. In the first, "coarse-grained" population, the grain size characteristics are similar to those of the initial powder compacts, and vary insubstantially with MM processing. The second, "ultrafine-grained" population, has an average grain size of approximately d_s=2.0μm

within 1-4μm variation limits. It is stabilized already after the MM processing for 180ks, and further processing leads to a decrease in the variation limits with a minor change in the average grain size. Along with these modest changes in the grain size characteristics of both the populations, the shell area fraction increases significantly from 21% to 42% with an increase of milling time from 180ks to 360ks.

4.3.3 Mechanical Properties of Harmonic-structured Compacts

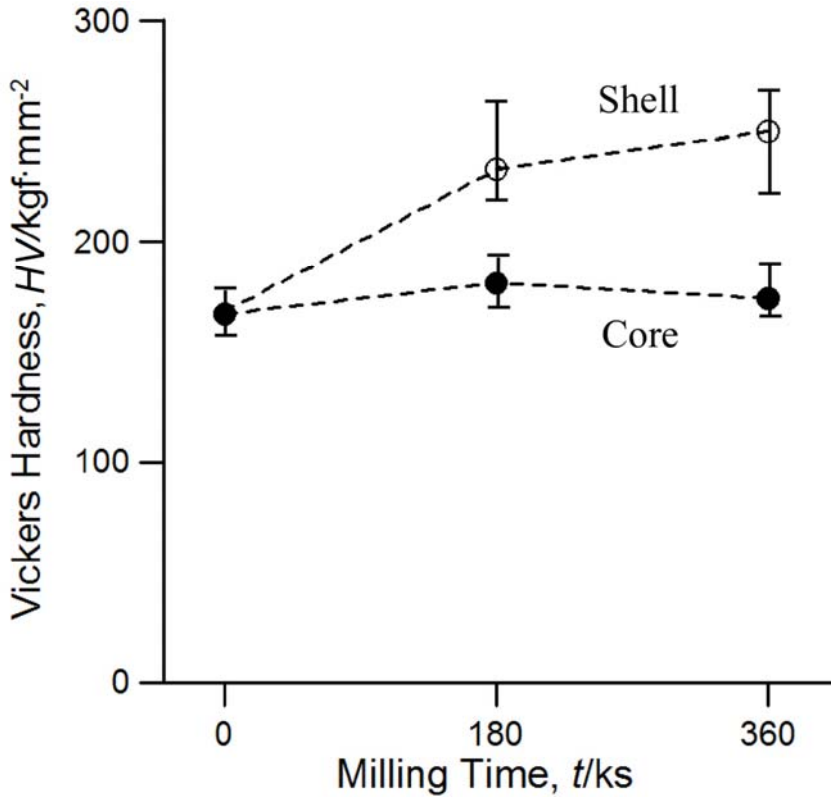

Figure 4.6 Diagram illustrating the dependence of Vickers hardness of the sintered SUS304L compacts on the time of mechanical milling.

Figure 4.6 shows the Vickers hardness (HV) values of sintered compacts prepared from the initial and the milled powders. In the harmonic-structured compacts, the

hardness measurements were carried out separately in the shell and the core areas. It can be noted that the hardness values of the compacts from the initial powder are at the same level as the hardness of the core in the harmonic-structured compacts. Figure 4.6 indicates that at the selected MM conditions, HV in the harmonic-structured SUS304L steel is almost independent on milling time, and the hardness of the shell becomes nearly 40% higher than that of the core. Although it appears that the average hardness value in the shell increases with an increase of MM time, effectively it remains within the statistical variation limits, and should rather be attributed to the accuracy of the measurement indenter positioning.

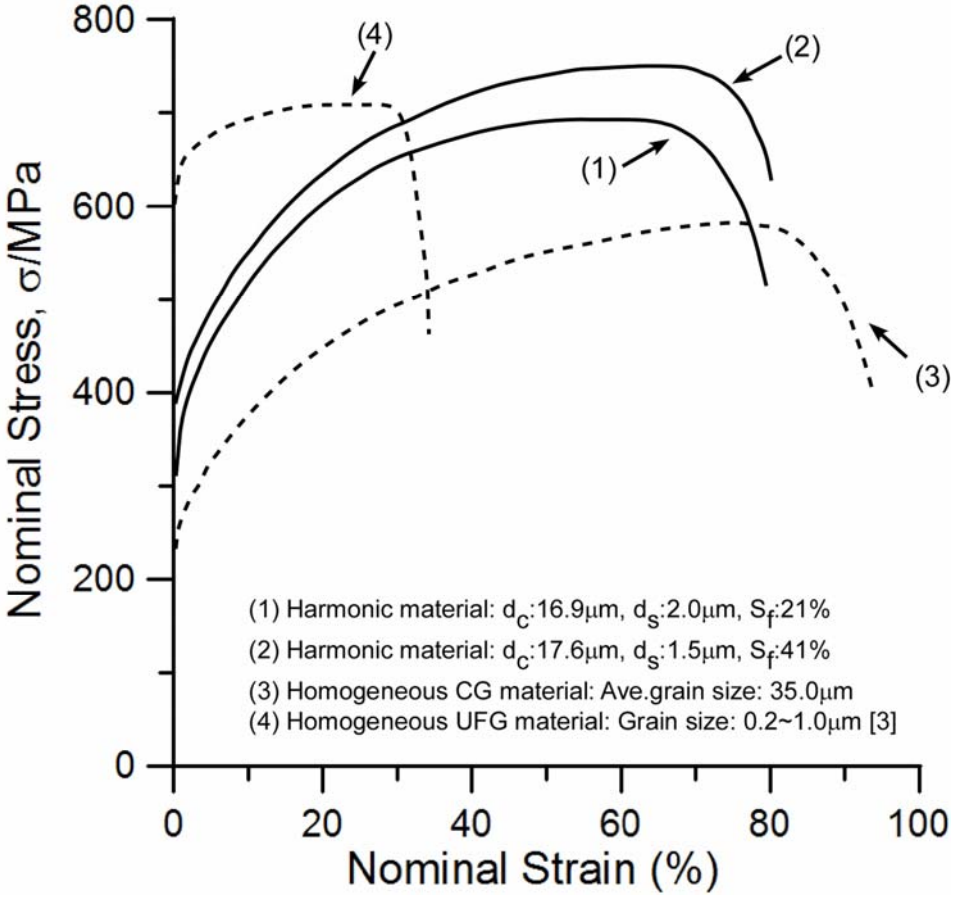

Figure 4.7 Representative tensile stress-strain curves of SUS304L steel having various structures.

(d_c means core grain size; d_s means shell grain size; S_f means shell fraction)

Table 4.2 Quantitative characteristics of mechanical properties of SUS304L steel after different kinds of thermo-mechanical processing.

No.	Processing**	$\sigma_{0.2}$* [MPa]	σ_{UTS}* [MPa]	ε_u* [%]	ε_t* [%]	Average grain size [μm], (fraction %)		Ref.
						bulk or core	shell	
1	MM180ks+SPS1173K	328	690	61.8	80.1	16.8 (79%)	2.0 (21%)	Present
2	MM360ks+SPS1173K	382	744	65.6	80.3	17.6 (59%)	1.5 (41%)	Present
3	Bulk	250	601	79.4	94.3	35.0 (100%)	---	Present
4	ECAP at 1073K	580	710	30.0	37.0	0.2-1.0 (100%)	---	[3]
5	IP+SPS1173K	260	516	44.6	48.4	19.7 (100%)	---	Present
6	ECAP at 973K	1013	1094	3.0	12.0	0.2-0.5 (100%)	---	[4]
7	Thermal cycling at 1173-1223K	902	1082	5.0	16.0	0.2-0.5 (100%)	---	[5]

*$\sigma_{0.2}$ stands for 0.2% proof stress; σ_{UTS} for ultimate tensile stress; ε_u for uniform elongation; and ε_t for total elongation.

**MM means mechanical milling of SUS304L powder; IP-initial powder; SPS-spark plasma sintering; and ECAP- equal channel angular pressing.

The results of tensile testing along with indicative data on SUS304L steel after different types of processing from the literature are summarized in Fig.4.7 and Table 4.2. The inferior ductility of compacts sintered from the initial powder can be attributed to the presence of significant amount of porosity compared to their fully dense alternatives produced by the ingot metallurgy route. Figure 4.7 shows the nominal stress-nominal strain curves, obtained from tensile tests of SUS304L steel specimens having various structures. It is interesting to note, that the 0.2% proof stress and the ultimate tensile

strength (UTS) of the harmonic-structured SUS304L steel (Specimen1: MM180ks powder compact; Specimen2: MM360ks powder compact) are superior to its coarse-grained counterpart (Specimen3: Bulk). At the same time, it has the uniform and the total elongations only 20% lower than that in the coarse-grained material. Moreover, the harmonic-structured compacts obtained from the MM360ks powder have higher strength, longer strain hardening stage, and more than twice higher elongation to failure when compared to the homogenous ultrafine-grained SUS304L steel (Specimen4), as can be seen in Fig.4.7. Homogeneous materials having finest, 0.2-0.5μm, grain size obtained by ECAP [4] or thermal cycling [5] have higher strength, but extremely inferior ductility characteristics when compared with the harmonic-structured one, as can be seen from Table 4.2.

Therefore, it can be concluded that the harmonic-structured SUS304L steel demonstrates winning combination of high strength, large uniform elongation and large total elongation to fracture.

4.4 Discussion

4.4.1 Control of Microstructure in Harmonic-structured SUS304L Steels during Fabrication

The experimental results presented above clearly demonstrate that the harmonic structure in the sintered compacts is derived from the presence of a shell-and-core bimodal structure in the mechanically milled powders. Moreover, in contrast to a more typically observed in a literature on bimodal grain structure, the harmonic one has a

specific periodic, or harmonic, arrangement. Such an arrangement is made possible by the selected approach and a strict control of the fabrication parameters. First, it is important to form core/shell structure in the metallic powder particles. This can be achieved by mechanical milling, as in the present study, or by other high-energy particle deformation techniques like jet milling, etc. Second, the particles having the core/shell structure should be sintered with minimal porosity, while the ultrafine-grained structure in the particle shell should be preserved to form a continuously connected network in the sintered compacts. This can be achieved by spark plasma sintering, as in the present study, or by other advanced sintering techniques like hot-roll sintering, etc.

Sharp core/shell grain size gradient could be observed in harmonic-structured SUS304L compacts (Fig.4.4). According to the XRD results of powders and sintered compacts in Fig.4.1 and Fig.4.3, the martensite transformation was observed near the powder surface during mechanical milling and austenite reversion was observed during sintering. Therefore, the possible cause of the formation of sharp core/shell grain size gradient is martensite transformation and subsequent austenite reversion. When powders received large strains at high strain rates, the temperature of the powders rise substantially. If the temperature rises above A_1 or A_3 point, the transformation to austenite phase can occurs. During unloading, the temperature of austenite area decreases rapidly and transforms to martensite. During the subsequent sintering process, the austenite reversion plays an important role on grain refinement in SUS304L steel. [6-9]

The thickness of this shell area, and hence the fraction of UFG structure, is controlled by such parameters of mechanical milling as (i) ball diameter (and hence weight), (ii) ball to powder ratio, (iii) milling time, and (iv) milling speed, temperature and

atmosphere. It is important to ensure that the impact from collisions between balls and particles leads to a limited-depth penetration of plastic deformation, and processing time is sufficient to produce the deformed UFG layer of even thickness. Of course, the fracture of particles should also be avoided. Appropriate selection of these parameters allows to control the process of mechanical milling precisely, and to produce the required gradient of microstructure in the processed powder particles.

A technique and parameters for the sintering of MM powders should be tailored to ensure appropriate compaction and then inter-particle bonding, while minimizing the processes of grain growth in the shell area. These can usually be achieved through the utilization of high hydrostatic pressure, fast heating/cooling rates, and high temperature applied for a short time. A technique perfectly satisfying all these criteria is spark plasma sintering, and therefore it was used in the present investigation. Hot-roll sintering is also an excellent technique for this purpose since in addition to hydrostatic pressure; it imparts shear deformation thus accelerating inter-particle bonding. In both these techniques, the control of holding temperature and time allows to adjust the balance of core/shell fractions, and to minimize the level of residual porosity.

In the present study, a significant amount of residual porosity is found in the compacts sintered from the initial non-processed powder, see Fig.4.4a. By contrast, the MM-processed powders sintered in essentially same conditions demonstrate virtually nil porosity in their microstructure, Fig.4.4c and 4.4e. These results indicate that, in addition to the formation of harmonic structure, the pre-processing by mechanical milling leads to the improvement of powder sinterability and density.

4.4.2 Correlation between Microstructure and Mechanical Properties in Harmonic-structured SUS304L Steels

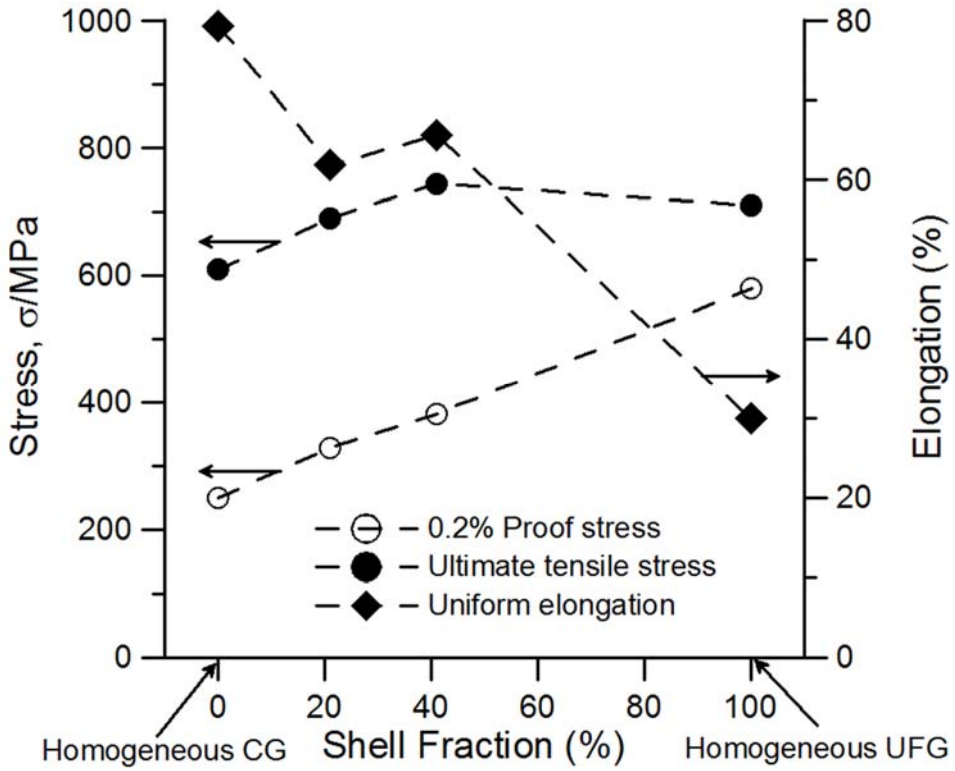

Figure 4.8 Dependence of strength and uniform elongation in SUS304L steel on shell fraction.

The microhardness measurements along with the SEM observations demonstrate that the harmonic-structured SUS304L compacts possess a microstructure wherein softer coarse-grained core areas are enclosed in a three-dimensional continuously connected network of harder ultrafine-grained shell. Qualitatively, such a variation in hardness well resembles the Hall-Petch relationship. Similar behaviour has 0.2% proof stress, which monotonically increases with an increase of the shell fraction, see Fig.4.8.

However, ultimate tensile strength and uniform elongation demonstrate different non-monotonic behaviour. Figure 4.8 reveals the dependencies of strength and uniform

elongation in SUS304L steel on the volume fraction of shell. It can be seen that the highest ultimate tensile strength of 744MPa is reached in the material with a shell fraction of 41%. Further increase of the fraction of UFG area to 100% only decreases the value of UTS a little. The uniform elongation in 100% UFG-structured SUS304L steel is less than a half of that in the 100% coarse-grained material. However, this dependence is non-monotonic in between these two extremes of the microstructural states. Namely, an increase in the shell fraction from 21% to 41%, leads to a substantial increase in uniform elongation as well as in the 0.2% proof stress. Therefore, the harmonic-structured SUS304L steel having 41% of the UFG shell area in the microstructure is found in the present study to be optimal for the balance of strength and ductility.

One more important conclusion can be made analysing a qualitatively different behaviour of the tensile testing characteristics in Fig.4.8. It can be seen that the rates of increase in 0.2% proof stress and UTS with an increase of the fraction of UFG structure are very different. This leads to a decrease of the difference between these two strength characteristics, which is also accompanied by a decrease of uniform elongation. Such behaviour can be attributed to a limited capacity of UFG materials produced by SPD for dislocation storage, and hence very limited strain hardening and uniform elongation. These are well-known drawbacks of ultrafine-grained and nano-crystalline microstructures [10]. In the harmonic-structured material, the capacity for strain hardening and uniform elongation as well as total elongation will depend on the balance between the shell and core fractions. This dependence can be as simple as the rule of mixtures, for example, or much more complicated. This question will be explored in further investigations.

4.4.3 Benefits of Harmonic Structure Design Concept for the Control of SUS304L Steels Performance

As summarized in Table 4.2, harmonic-structured SUS304L steel samples with superior mechanical properties were fabricated in the present study. The selected approach allows to control the microstructural characteristics, and thus the material performance, in a rather wide range. This design concept appears to be winning from the point of view of precisely tailorable balance between the strength and ductility characteristics. Namely, the harmonic-structured material significantly exceeds the mechanical characteristics of SUS304L steel commercially supplied by different manufacturers [11, 12]. Compared to the ordinary products with a homogeneous grain size of ~35μm produced by the ingot metallurgy route, the harmonic-structured one possesses slightly inferior ductility, but nearly 30% higher 0.2% proof and ultimate tensile strengths.

To the best of the authors knowledge, the record level of strength (0.2% proof stress = 1013MPa and UTS=1094MPa) was achieved in ultrafine-grained (<d>=0.2-0.5 μm) SUS304L steel by ECAP processing at 973 K [4]. A similar level of the strength and the microstructure characteristics was produced by a thermal cycling at 1173-1223 K [5]. However, the ductility characteristics were so low (the uniform and total elongations down to 3% and 12%, respectively) that further processing as well as potential applications of such materials were largely compromised. By contrast, the harmonic-structured SUS304L steel exceeds these ductility characteristics by far (68% and 80%, respectively), which opens up a much wide avenue for the applications of this

material.

Furthermore, the selected powder metallurgy based approach for the fabrication of harmonic-structured materials allows the consolidation of mechanically milled powders into final products. This may further reduce the cost of industrial manufacturing processes based on this approach, which makes the proposed concept of material design even more attractive for commercial applications.

4.5 Conclusions

In this chapter, the commercially supplied PREPed SUS304L powders were mechanical milled and spark plasma sintered to produce a compact material having "harmonic structure". The microstructure evolution and the mechanical properties of the sintered SUS304L compacts were analyzed. Based on this analysis, the following conclusions can be drawn:

(1) Martensite transformation and subsequent austenite reversion plays an important role on grain refinement in the sintered SUS304L steels.

(2) A heterogeneous shell-and-core microstructure with bimodal grain size distribution can be produced in SUS304L steel powder particles by mechanical milling. The parameters of microstructure in the milled powder can be controlled by such processing in a rather wide range. In addition, mechanical milling leads to the alteration of shape of initially spherical powder particles, which improves their compactability.

(3) Spark plasma sintering was successfully utilized for the consolidation of mechanically milled powders, which produced harmonic-structured material. The

microstructure of this material comprised of soft core areas with coarse structure enclosed into three-dimensional network of hard ultrafine-grained structure. A balance between the shell and core fractions is an extremely important parameter for the control of the mechanical performance of harmonic-structured SUS304 steel.

(4) The harmonic-structured SUS304L steel demonstrates a superior combination of high strength, large uniform elongation, and large total elongation. Such a combination makes this material as well as the proposed approach of its fabrication very attractive for commercial applications.

References

[1] Y. Chen, J. Hjelen and H. Roven, Application of EBSD technique to ultrafine grained and nanostructured materials processed by severe plastic deformation: Sample preparation, parameters optimization and analysis, Transaction Nonferrous Metals Society of China, 22 (2012) 1801-1809.

[2] P. Suri, R. Koseski and R. German, Microstructural evolution of injection molded gas- and water-atomized 316L stainless steel powder during sintering, Materials Science and Engineering A, 402 (2005) 341-348.

[3] S. Qu, C. Huang, Y. Gao, G. Yang, S. Wu, Q. Zhang and Z. Zhang, Tensile and compressive properties of AISI 304L stainless steel subjected to equal channel angular pressing, Materials Science and Engineering A, 475 (2008) 207-216.

[4] C. Huang, G. Yang, Y. Gao, S. Wu and Z. Zhang, Influence of processing

temperature on the microstructures and tensile properties of 304L stainless steel by ECAP, Materials Science and Engineering A, 485 (2008) 643-650.

[5] B. Kumar and D. Raabe, Tensile deformation characteristics of bulk ultrafine-grained austenitic stainless steel produced by thermal cycling, Scripta Materialia, 66 (2012) 634-637

[6] H. Fujiwara, H. Inomoto, R. Sanada and K. Ameyama, Nano-ferrite formation and strain-induced-ferrite transformation in an SUS316L austenitic stainless steel, Scripta Materialia, 44 (2001) 2039-2042.

[7] A. Di schino, I. Salvatori and J. Kenny, Effects of martensite formation and austenite reversion on grain refining of AISI304 stainless steel, Journal of Materials Science, 37 (2002) 4561-4565.

[8] M. Umemoto, Nanocrystallization of steels by severe plastic deformation, Materials Transactions, 44 (2003) 1900-1911.

[9] R. Valiev, M. Zehetbauer, Y. Estrin, H. Höppel, Y. Ivanisenko, H. Hahn, G. Wilde, H. Roven, X. Sauvage and T. Langdon, The innovation potential of bulk nanostructured materials, Advanced Engineering Materials, 9 (2007) 527-533.

[10] M. Meyers, A. Mishra and D. Benson, Mechanical properties of nanocrystalline materials, Progress of Materials Science, 51 (2006) 427-556.

[11] http:// www.susjis.info/austenitic/sus304l.html, (last accessed 12.25 2013).

[12] http:// www.316l-stianless.com/ Stainless-steel/ JIS-G4303-SUS304L.html, (last accessed 12.25 2013).

Chapter 5 Deformation and Fracture Mechanism of SUS304L Compacts with Harmonic Structure

5.1 Introduction

Strengthening at the cost of ductility is not uncommon, ultrafine-grained (UFG) bulk materials indicate that they possess very high hardness and strength, but their ductility, in particular uniform elongation in tension has been rather low and in the most cases nowhere close to that of the conventional metals and alloys. [1, 2] Most UFG materials are characterized by low tensile ductility at room temperature because of plastic strain instability in the form of a localization of plastic flow in shear bands and neck formation. Plastic strain instability is the main factor causing low tensile ductility in UFG materials. [3]

However, both strength and ductility are the important mechanical properties of the materials for industrial applications. Various strategies have been suggested to overcome these obstacles with the aim to jointly improve ductility and strength. [3-5] Creating a bimodal (or multi-modal) grain size distribution is a useful strategy to enhance ductility, which could achieve simultaneously good yield strength and fairly large uniform (and total) elongation. The UFG matrix in the bimodal microstructure provides the high strength, while the relatively large coarse grains (CG) contribute to

the ductility. Bimodal bulk UFG/CG metals and alloys can be synthesized by: (i) thermo-mechanical treatment involving severe plastic deformation, i.e., cold rolling or equal-channel angular pressing, followed by an appropriate thermal annealing under controlled conditions [6,7]; and (ii) mechanical milling plus the consolidation of the milled powders mixed with certain volume fractions of the as-received CG powders [8,9]. However, the exact distributions of the grain size, grain shape, and spatial locations depend on many processing parameters and may be difficult to reproduce each time. Therefore, the outcome properties span a relatively wide range depending on the microstructural variations. [4,5]

Recently, Ameyama and co-workers proposed an approach, which allows achieving both high strength and high ductility in metallic materials through the formation of socalled "harmonic" structure. Essentially, the "harmonic structure" is a "nano and heterogeneous bimodal structure" consisting of CG areas (or "cores") enclosed in a three-dimensional continuously connected network of UFG structure (or "shell"). In addition to be bimodal, the term "harmonic" signifies that this structure has a specific topology: "ultrafine" and "coarse" grains in it are positioned in a periodic, or the "harmonic" order. In Chapter 4, the harmonic-structured SUS304L compacts have been acquired using PREPed powders by MM-SPS method. Compared to homogeneous CG and UFG materials, the harmonic-structured SUS304L steel demonstrates a superior combination of high strength, large uniform elongation, and large total elongation. However, the reason for the improved ductility, in particular uniform elongation in tension has not been revealed yet. Therefore, in this chapter, heterogeneous bimodal structured SUS304L compacts are fabricated and compared with harmonic bimodal structured ones. The effect of heterogeneity and topology of bimodal structure on

ductility is discussed. Moreover, the deformation and fracture mechanism of harmonic-structured SUS304L is also discussed.

5.2 Experimental Procedure

In Chapter 4, it is found that the gain size of coarse grains and ultrafine grains of sintered SUS304L compacts was similar. In addition, the shell fraction of MM180ks powder compact was approximately 21%, while that value was approximately 42% in MM360ks powder compact. Therefore, MM180ks powders (mass100%) were used to fabricate harmonic bimodal structured compacts having a regular three-dimensional continuous network UFG structure. While a mixture of initial powders (IP) and MM360ks powders (weight ratio=1:1) was sintered to fabricate heterogeneous bimodal structured compacts having irregular spatial distribution of CG and UFG structure.

The same PREPed SUS304L powders were also mechanical milled and sintered by SPS under 50MPa for 3.6ks at 1173K. Subsequently, the microstructure observation and tensile tests were same like that used in Chapter 4.

5.3 Results

5.3.1 Mechanical Properties of Harmonic and Heterogeneous Bimodal Structured Compacts

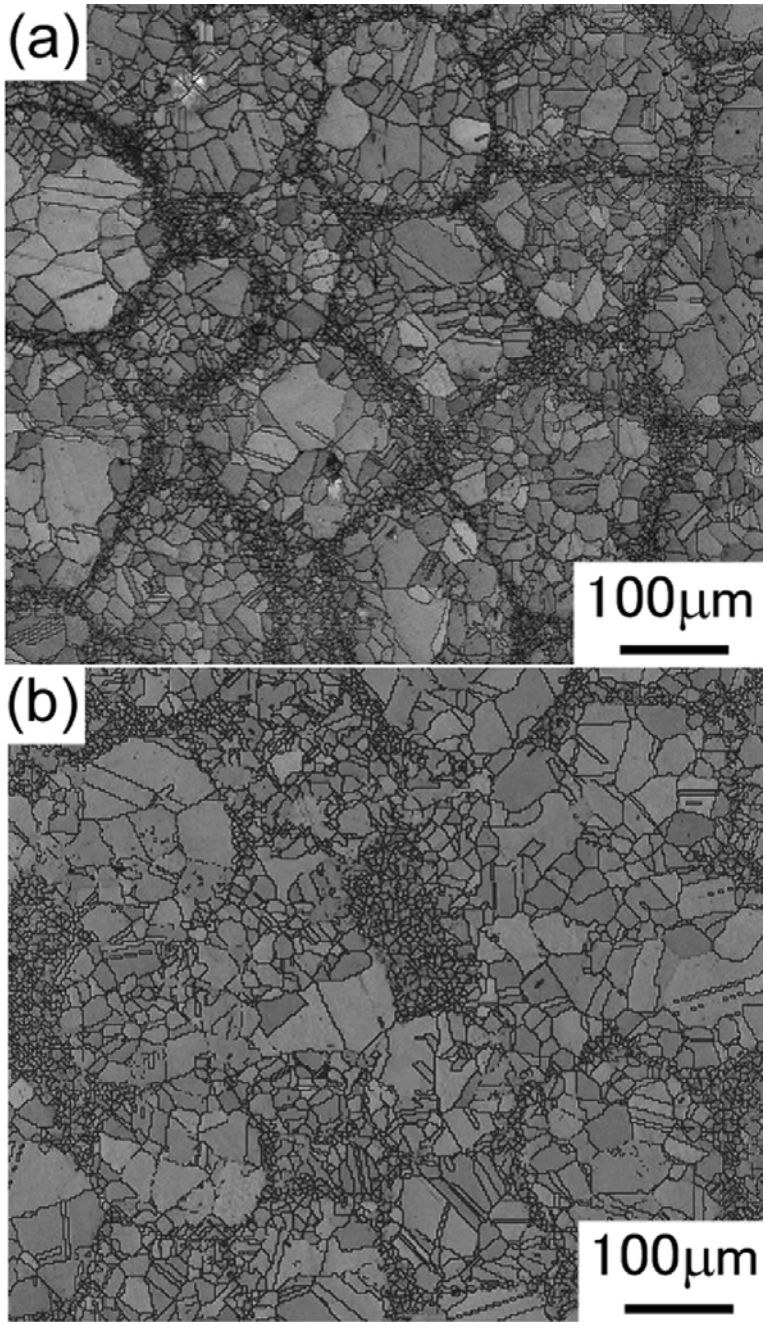

Figure 5.1 Microstructures of SUS304L compacts sintered from (a) MM180ks powders, (b) IP+MM180ks powders (weight ratio=1:1). (EBSD image quality maps overlaid with HABs)

Figure 5.1 and Table 5.1 shows the microstructure characteristics of the sintered SUS304L compacts prepared from MM180ks powders, and a mixture of initial powders and MM360ks powders (weight ratio=1:1). It can be clearly observed that both sintered

compacts have a bimodal microstructure with an average coarse grain size of approximately d_c=18μm within 15-25μm variation limits and an average ultrafine grain size of approximately d_s=2.0μm within 1-4μm variation limits. Furthermore, the UFG fraction is also similar, approximately 20%.

Table 5.1 Microstructure characteristics and mechanical properties of SUS304L steel after different kinds of processing.

No.	Processing**	$\sigma_{0.2}$* [MPa]	σ_{UTS}* [MPa]	ε_u* [%]	ε_t* [%]	Average grain size [μm], (fraction %)	
						CG	UFG
1	MM180ks+SPS1173K	328	690	61.8	80.1	16.8 (79.3%)	2.0 (20.7%)
2	IP+MM360ks (weight ratio=1:1) +SPS1173K	340	694	46.3	56.9	18.4(80.4%)	1.5 (19.6%)
3	Bulk	250	601	79.4	94.3	35.0 (100%)	---

*$\sigma_{0.2}$ stands for 0.2% proof stress; σ_{UTS} for ultimate tensile stress; ε_u for uniform elongation; and ε_t for total elongation.

**MM means mechanical milling of SUS304L powder; SPS-spark plasma sintering; IP-Initial powder.

However, the homogeneity and topology of UFG spatial location are different in both sintered compacts. It can be noticed that the sintered compact prepared from the MM180ks milled powders has a peculiar microstructure wherein the CG areas are enclosed in a three-dimensional continuously connected network of the UFG areas, which is termed as “harmonic bimodal structure”. By contrast, the sintered compact prepared from the mixed powders has a heterogeneous irregular CG and UFG areas distribution, which is termed as “heterogeneous bimodal structure”.

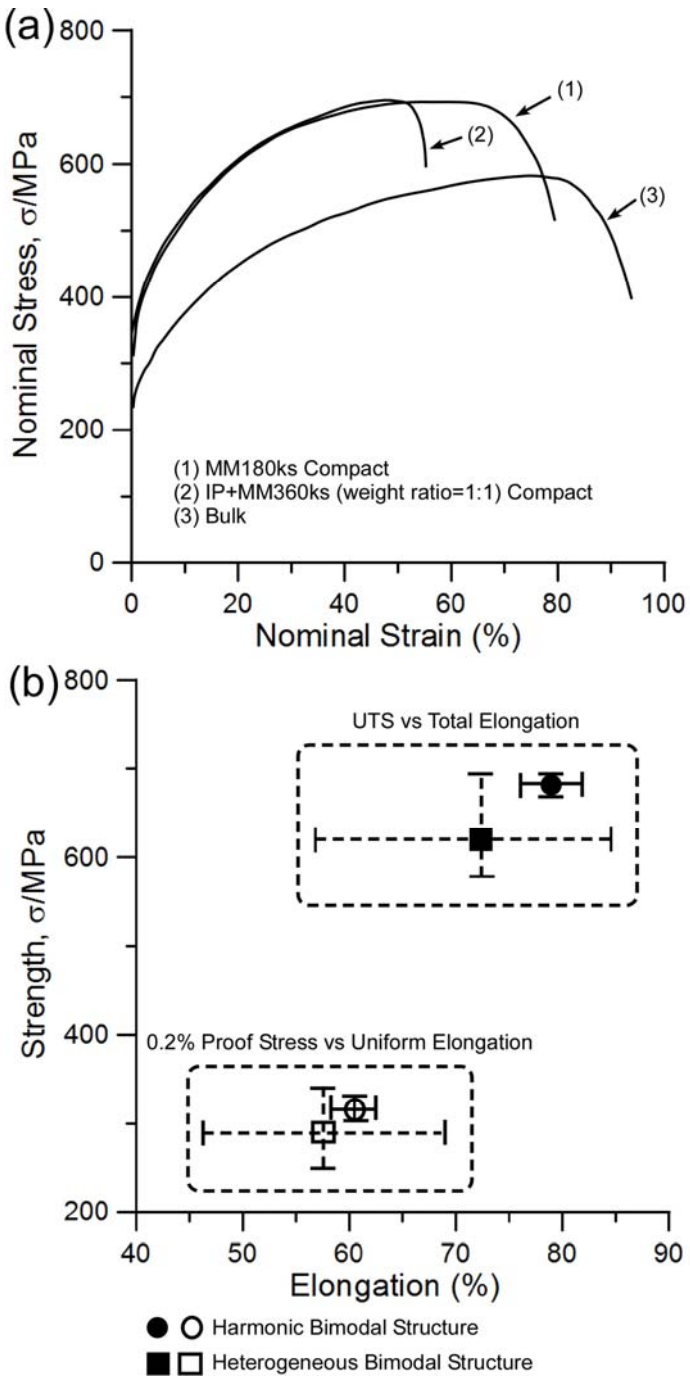

Figure 5.2 Representative tensile properties of SUS304L steel from different fabrication processes. (a) Nominal stress-nominal strain curves; (b) Tensile reproducibility of bimodal structured compacts.

The tensile performance of samples having these microstructures is summarised in Fig.5.2 and Table 5.1. Both samples having the bimodal grain size distribution exhibit significantly higher strength as compared to the ordinary CG specimens, Fig.5.2a and

Table 5.1. It can be noted that the heterogeneous and the harmonic structured samples have comparable yield strength (YS, the 0.2% proof stress) and the ultimate tensile strength (UTS), Fig.5.2b and Table 5.1. Moreover, the strain hardening behaviour of the heterogeneous and the harmonic structured samples is very similar, as can be seen from stress-strain curves in Fig.5.2a.

Nevertheless, it is interesting to note that despite very similar strength characteristics in the bimodal SUS304L compacts, their ductility characteristics are significantly different. Namely, the "harmonic structured" sample exhibit approximately 15% higher uniform elongation (E_u) and almost 25% higher total elongation (E_t) when compared to its "heterogeneous structured" counterpart, Fig.5.2a and Table 5.1. Furthermore, the harmonic structured sample demonstrates total elongation very close to that of the bulk CG material.

Statistical variation of the tensile properties of SUS304L compacts with the "harmonic" and the "heterogeneous" bimodal grain structures is presented in Strength-Elongation property space in Fig.5.2b. First, it is evident that the average values of $\sigma_{0.2}$-ε_u as well as σ_{UTS}-ε_t are higher in the harmonic structured material. This holds true even considering the variations of these properties in the harmonic-structured samples. Furthermore, the variation of the tensile properties in the "harmonic" structured material is reasonably narrow. By contrast, the variations of corresponding tensile properties in the "heterogeneous" structured material are very wide. In fact, these variations are so wide that they envelope the values of respective properties in the "harmonic" structured material. These observations suggest that the control of bimodal microstructure topology allows to improve the average values of tensile characteristics in SUS304L steel as well as the reproducibility of results.

Therefore, it can be concluded that the harmonic bimodal structured SUS304L steel demonstrates winning combination of high strength, large uniform elongation and large total elongation to fracture when compared to the heterogeneous bimodal structured ones. Moreover, the tensile properties of harmonic bimodal structured compacts exhibit well reproducibility.

5.3.2 Deformation Behavior of Harmonic and Heterogeneous Bimodal Structured Compacts

Figure 5.3 illustrates the morphologies of the gauge sections of tensile specimens with bimodal structure deformed to approximately same strain values of $\varepsilon \approx 0.57$. A diagram in Fig.5.3c reveals variations of the gauge cross-section along tensile axes of the harmonic and the heterogeneous structured specimens shown in Figs.5.3a and 5.3b, respectively. It is clear that the reduction of cross-section in the "heterogeneous" structured specimen is remarkably heterogeneous, i.e. the area of sample cross-section becomes non-uniformly reduced with a minimum value of ~0.6 mm^2, which is the evidence of necking, Fig.5.3b. By contrast, the reduction of cross-section area in the "harmonic" structured sample remains rather uniform, i.e. the area of sample cross-section becomes reduced from ~1 mm^2 to ~0.7 mm^2 without any noticeable neck formation, Fig.5.3a. These results demonstrate that although the 'harmonic' structure design is heterogeneous on microscale, it is extremely effective in thwarting the localization of plastic deformation during tensile straining, thus improving the overall homogeneity of plastic deformation on macroscale.

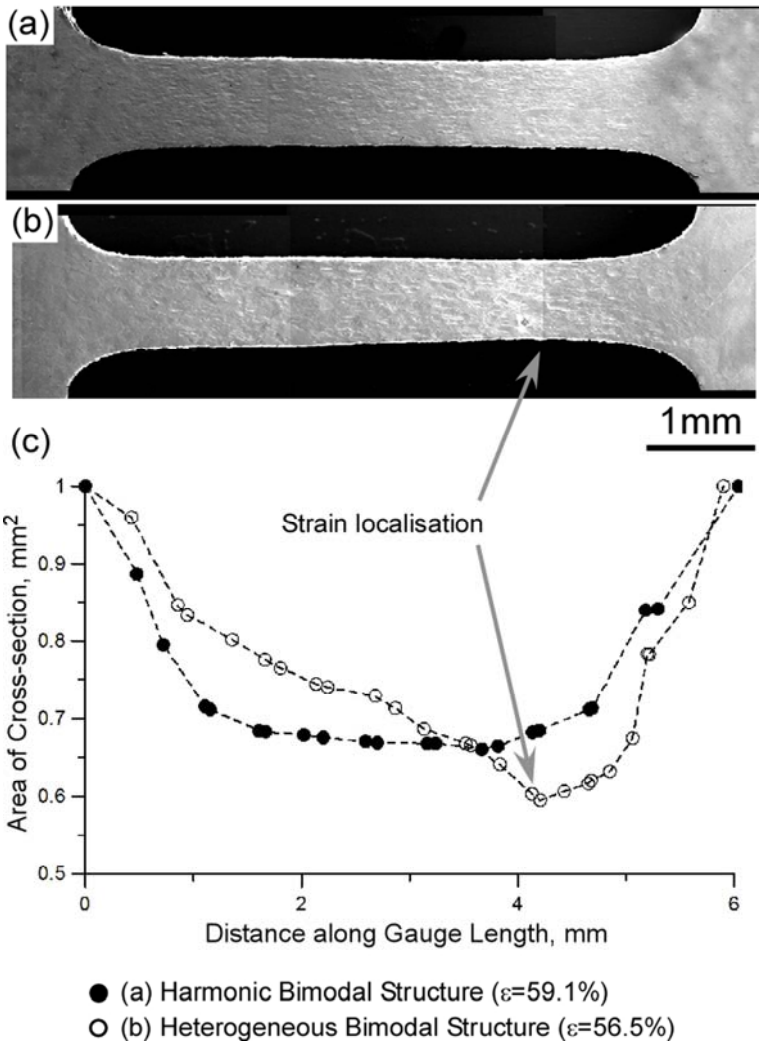

Figure 5.3 Morphology of tensile elongated specimens having bimodal structure: (a) Harmonic bimodal structure (ε=0.59); (b) Heterogeneous bimodal structure (ε=0.57); (c) Cross-sectional area shrinkage.

The EBSD technique has a significant impact on the study of component life expectancy and failure analysis by easily and efficiently providing information on grain size, grain boundary character, local and bulk texture and individual grain orientation. [10-12] In this work, local misorientation maps are used to present for visualizing plastic deformation at the micron length scale. These maps will highlight local strain variations in the elongated specimens, independent from the grain size.

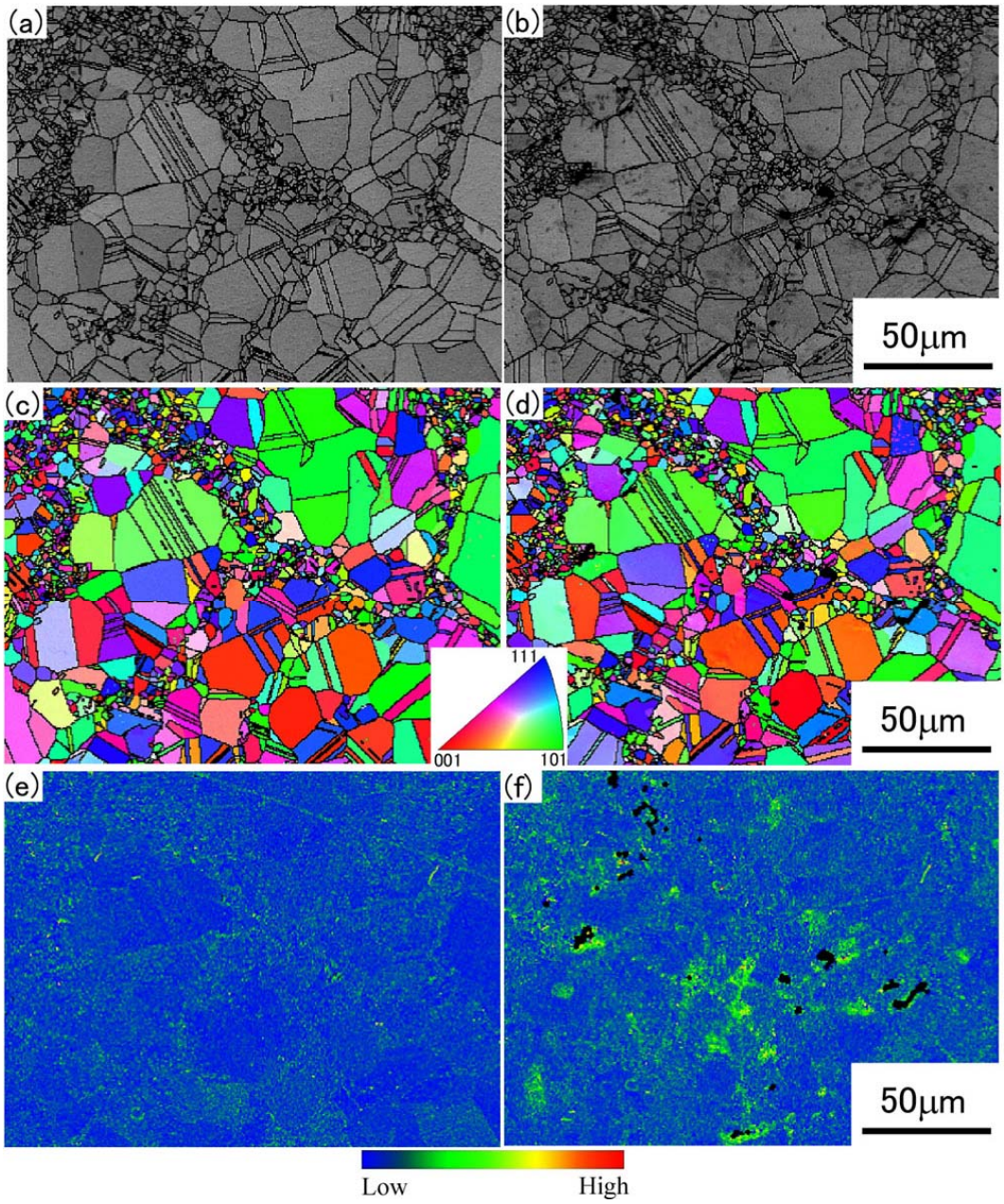

Figure 5.4 EBSD images taken on the same surface area of MM180ks powder specimen: the left images are before tensile test and the right images are after tension up to a strain of ε=0.01. (The tensile direction is horizontal)

(a) and (b) the image quality index (IQ) of the Kikuchi-lines together with the grain boundaries. Black lines indicate misorientations above 15° between adjacent points. (c) and (d) the inverse pole figure (IPF) based orientation maps. (e) and (f) the local misorientation maps.

Figure 5.4 illustrates the microstructure evolution in MM180ks powder compact during tension test by comparing the EBSD images taken on the same area before tension and after the sample has been deformed up to a plastic strain of about ε=0.01. Figure 5.4a represents the image quality index (IQ) of the Kikuchi-lines together with the grain boundaries. Black lines indicate misorientations above 15° between adjacent points. The coarse grains (core) and ultrafine grains (shell) can be observed clearly in this sample. Taking the inverse pole figure (IPF) based orientation map of Figs. 5.4c for the same sample, the same color inside the grains means similar orientation. Figure 5.4e presents the local strain distribution in the non-deformed sample by means of the colour coded misorientation map. The blue colour indicates the non-deformed sample with low local misorientation. The orientation map of the sample with ε=0.01 tensile strain exhibits the similar colour inside grains in both core and shell, which indicates very little deformation inside the grains after ε=0.01 tensile deformation (Fig.5.4d). However, high local misorientation (green and yellow colour) appears at shell/core boundary, (Fig.5.4f). It indicates the local strain concentrates at shell/core boundary firstly owing to the different ductility between shell and core. It is well known that the pattern quality of the EBSD deteriorates with increasing density of defects like dislocations and accumulated strain in materials. Therefore, sometimes non-indexed points (black points) present in the heavily deformed area. [13, 14]

Because the surface of specimen with a plastic strain of ε=0.1 deformed severely, the pattern quality of EBSD cannot be detected accurately. Therefore, another three specimens with a plastic strain of ε=0.1, ε=0.4 and ε=0.7 were re-polished and observed by OM and EBSD, respectively.

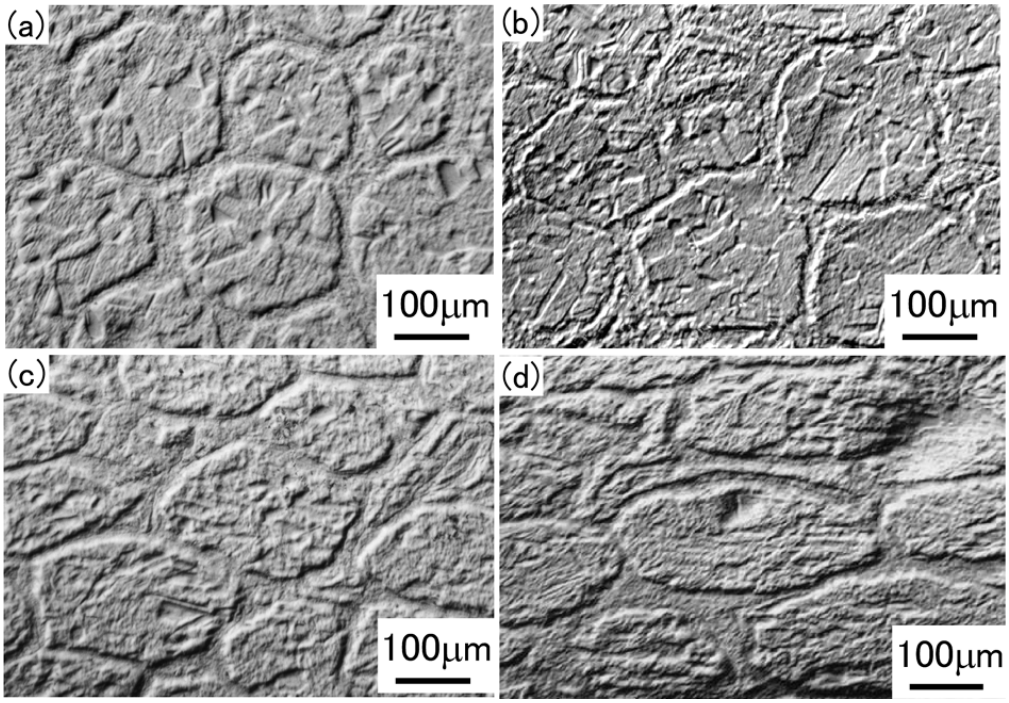

Figure 5.5 OM images taken on deformed MM180ks powder specimen: (a) ε=0; (b) ε=0.1; (3) ε=0.4; (4) ε=0.7. (The tensile direction is horizontal)

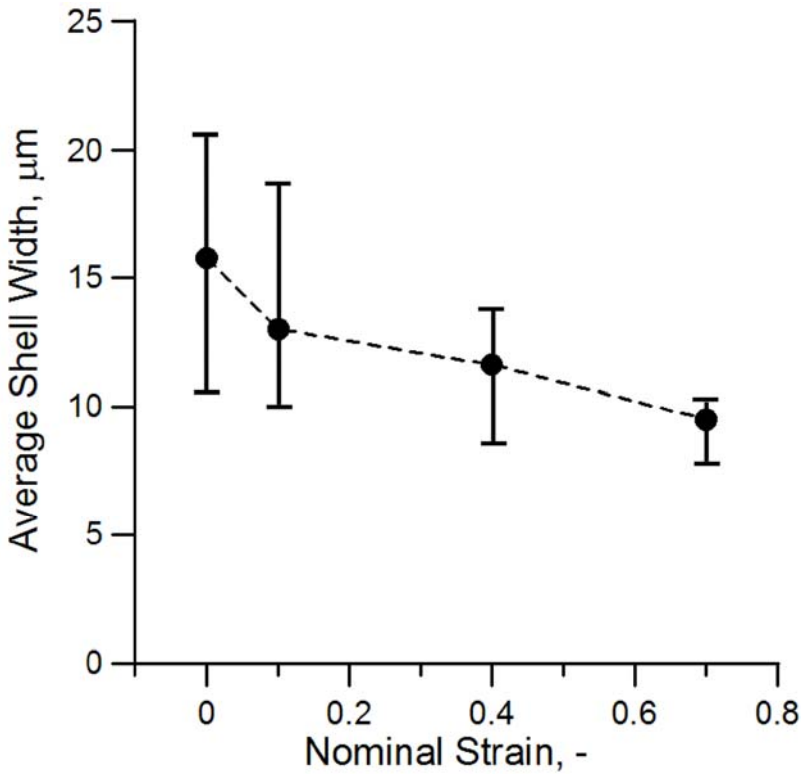

Figure 5.6 Shell width evolution under difference tensile strains.

Figure 5.5 shows the macrostructure evolution of specimens having different tensile strains. It is clearly that every shell-and-core unit is elongated along tensile direction homogenously with increased strain. Moreover, the average shell width evolution is presented in Fig.5.6. It is shown that the average shell width reduces when the tensile strain increases.

Figure 5.7 shows the microstructure evolution of ε=0.1, ε=0.4, and ε=0.7 strained specimens, respectively. Figure 5.7a and Figure 5.7b illustrates the sample deformed up to a plastic strain of about ε=0.1. It is clear that high misorientation forms at the grain boundary and mainly appears in the ultrafine-grained area. It is considered that the strain accumulates much heavier at grain boundary than inside the grains. Moreover, deformation occurs mainly in shell (UFG structure) at initial stage. As strain up to ε=0.4, it is clear from Fig.5.7c and Fig.5.7d that every shell/core unit deformation propagates to a wide range of the specimen. It is shown that the IQ distribution varies through the microstructure. Particularly the elongated coarse grains are much brighter than the ultrafine grains, indicating that ultrafine grains have larger stored energy. The slip bands and deformation twins appear in the elongated core. Noteworthy is that high misorientation distribution in each shell/core unit is similar. As strain up to ε=0.7, it is clear from Fig.5.7e and Fig.5.7f that the harmonic structure is elongated further, much more work-hardening accumulates in the core and high misorientation distribution in each shell-and-core unit is also similar. It is considered that work-hardening accumulates in the core and every shell-and-core unit deforms homogenously with increased strain.

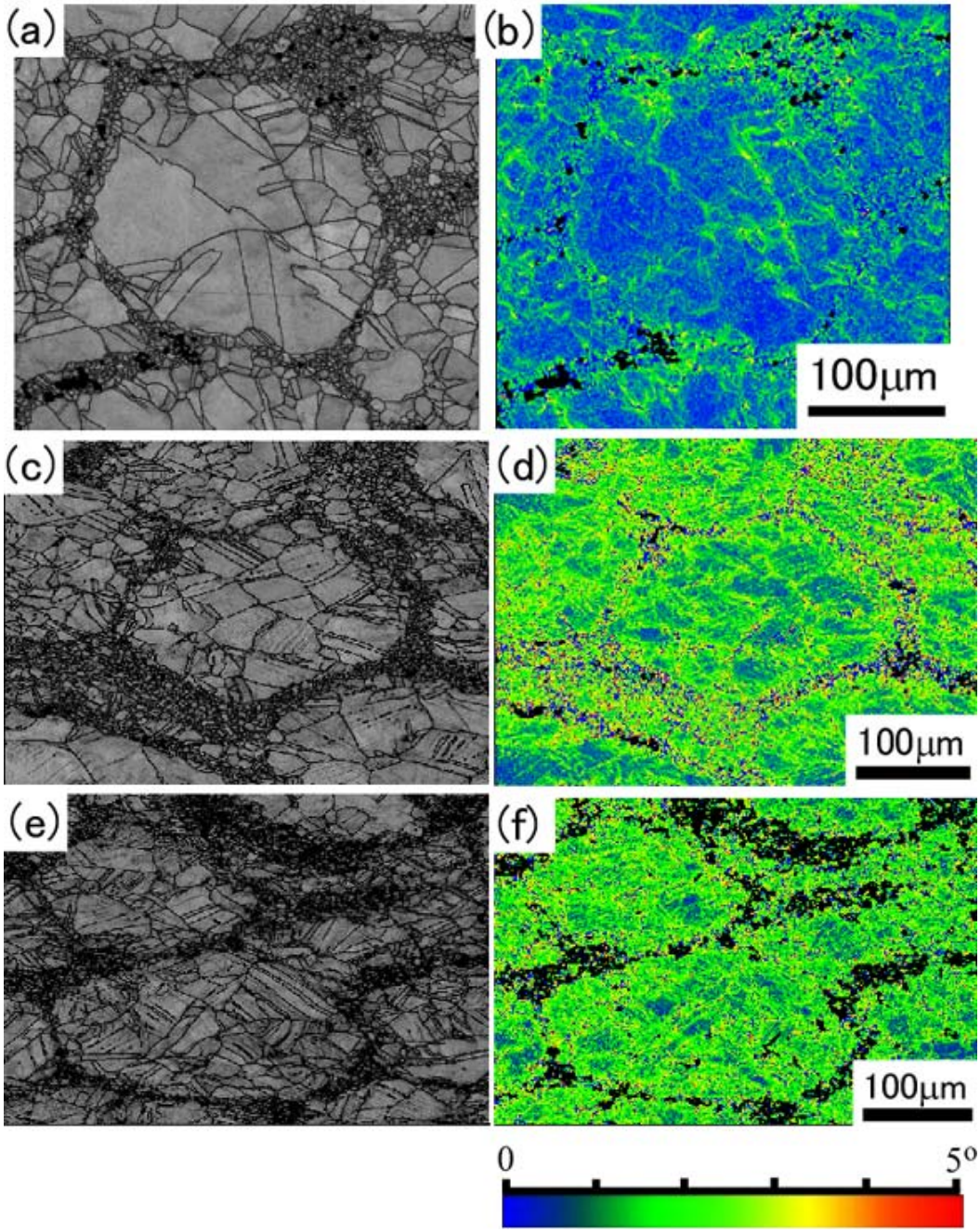

Figure 5.7 EBSD micrographs taken on deformed MM180ks powder specimens: the left maps are the image quality index (IQ) of the Kikuchi-lines together with the grain boundaries, and the right ones are the local misorientation maps. (a) and (b) ε=0.1; (c) and (d) ε=0.4; (e) and (f) ε=0.7. (The tensile direction is horizontal)

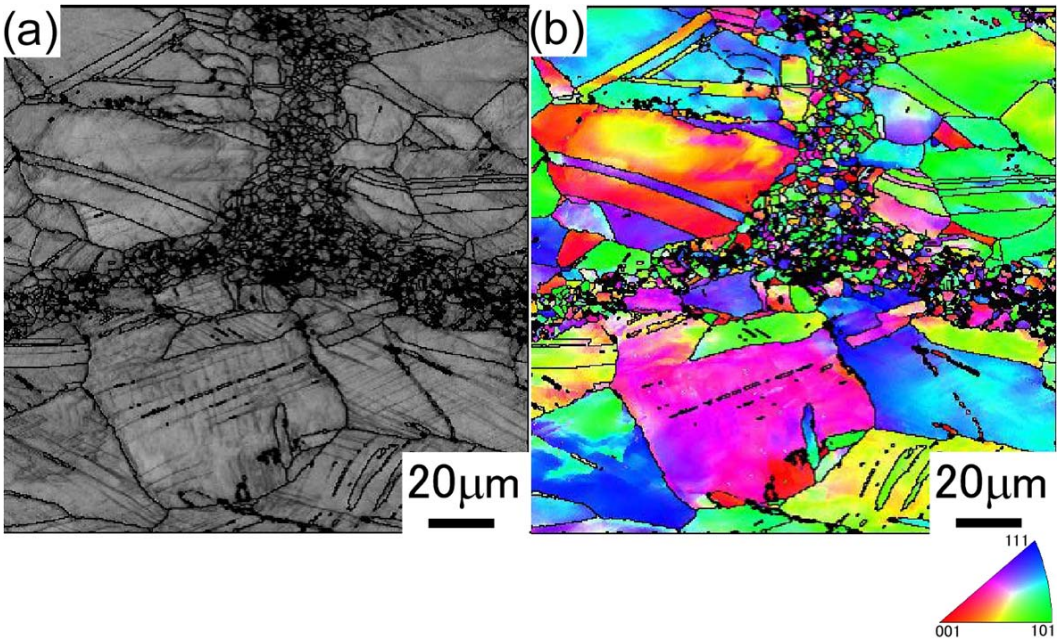

Figure 5.8 EBSD micrographs taken on deformed MM180ks powder specimens (ε=0.4): (a) the image quality index (IQ) of the Kikuchi-lines together with the grain boundaries; (b) the inverse pole figure (IPF) based orientation map. (The tensile direction is horizontal)

To reveal the deformation mechanism of CG and UFG grains, the EBSD micrographs taken on the specimen deformed up to a plastic strain of about ε=0.4 were observe under higher magnification. It is clear from Fig.5.8a the IQ distribution varies through the microstructure. The formed slip bands are observed in the CG region, rather than in the UFG region. Figure 5.8b illustrates the microstructure evolution in deformed specimen. It can be seen that the colour in the coarse grains is non-uniform. It indicates misorientation forms inside coarse grains during plastic straining as a result of dislocation activity. On the contrary, the colour in the ultrafine grains is still uniform, which indicates seldom the plastic deformation is accumulated in ultrafine grains.

5.3.3 Fracture Behavior of Harmonic and Heterogeneous Bimodal Structured Compacts

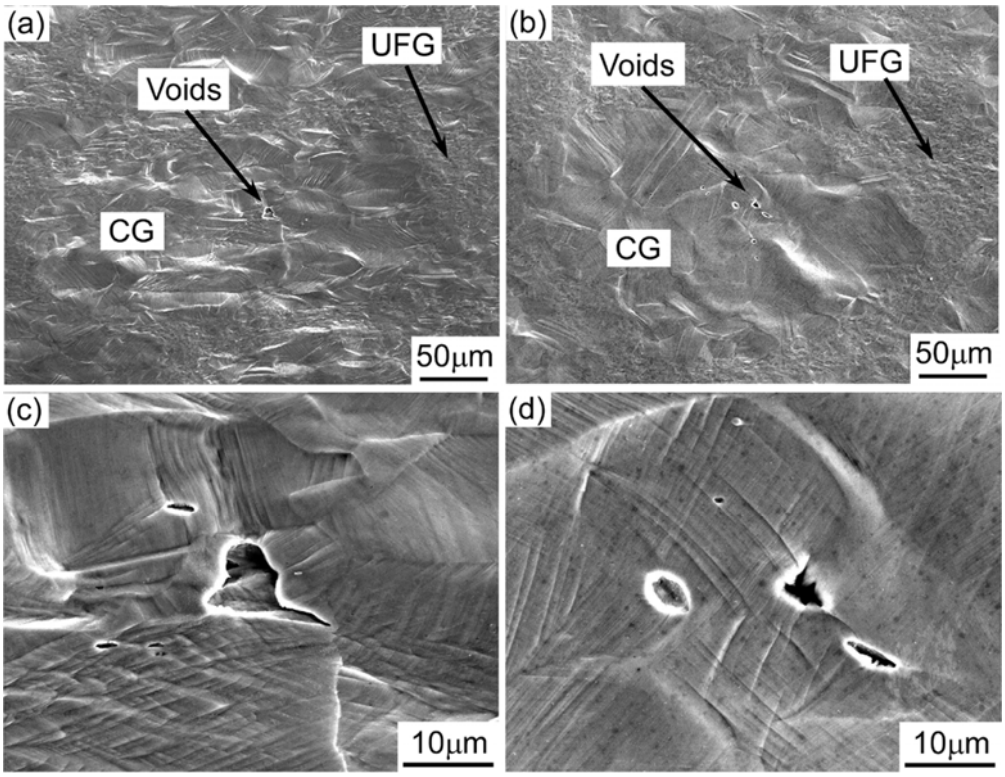

Figure 5.9 Void nucleation in tensile deformed SUS304L specimens having bimodal structure: (a) Harmonic bimodal structure (ε=0.59); (b) Heterogeneous bimodal structure (ε=0.57); (c) Enlargement of voids in Fig.5.9a; (d) Enlargement of voids in Fig.5.9b. (The tensile direction is horizontal)

To get understanding of the cracks initiation and propagation, surfaces of tensile-elongated specimen perpendicular to the fracture surface were analyzed. Figure 5.9 illustrates the void nucleation in the tensile deformed SUS304L specimen having bimodal structure. As shown in Fig.5.9a and Fig.5.9b, many slip bands and voids (microcracks) were observed in coarse grains of both harmonic and heterogeneous

bimodal structured SUS304L specimens. Observing these voids under higher magnification in Fig.5.9c and Fig.5.9d, it is note that the void nucleation occurred at the intersection position of pile-up slip bands in the CG regions. Moreover, statistical analysis has been employed to obtain an understanding of the voids and cracks positions in tensile deformed specimens. It is found that approximately 80% voids and cracks nucleated in the CG region, the other 20% voids nucleated at the CG/UFG boundary, but no void appeared in the UFG region in both bimodal structured specimens. Therefore, it is concluded that the void nucleation occur easily from pile-up slip bands in the CG regions in the tensile elongated SUS304L specimen having bimodal structure.

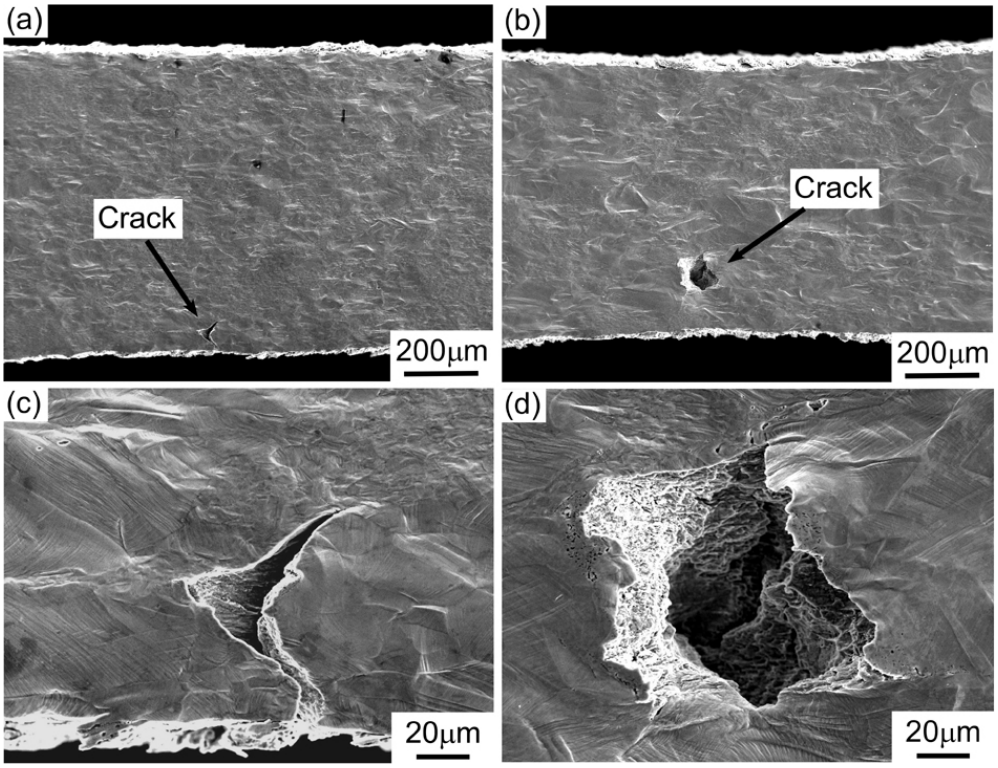

Figure 5.10 Cracks morphology in the tensile deformed specimens having bimodal structure: (a) Harmonic bimodal structure (ε=0.59); (b) Heterogeneous bimodal structure (ε=0.57); (c) Enlargement of cracks in Fig.5.10a; (d) Enlargement of cracks in Fig.5.10b. (The tensile direction is horizontal)

Figure 5.10 shows the morphology of the largest cracks formed in the bimodal structured SUS304L specimens with deformed up to a plastic strain of about ε=0.57. From Fig.5.10a and Fig.5.10c, the obvious necking cannot be seen in the tensile-elongated “harmonic” bimodal structured specimen. By contrast, it is clear from Fig.5.10c that the larger crack appeared in the strain localization region in the elongated “heterogeneous” bimodal structured specimen.

Statistical analysis has been employed to obtain an understanding of voids distribution in the bimodal structured SUS304L specimens with deformed up to a plastic strain of about ε=0.57 (just exceed neck formation) in Fig.5.11. As shown in Fig. 5.11a, the whole gauge was divided into five regions, wherein the mean area of voids and the number of voids in each region were summarized. Figure 5.11b shows the surface voids distribution in the harmonic bimodal structured specimen. Many voids spread through the gauge area and the mean area of voids increased gradually from the end to the center of gauge area. By contrast, it is clear from Fig.5.11c that the fewer but more concentrated voids were observed in the elongated “heterogeneous” structured sample as compared to the “harmonic” structured one.

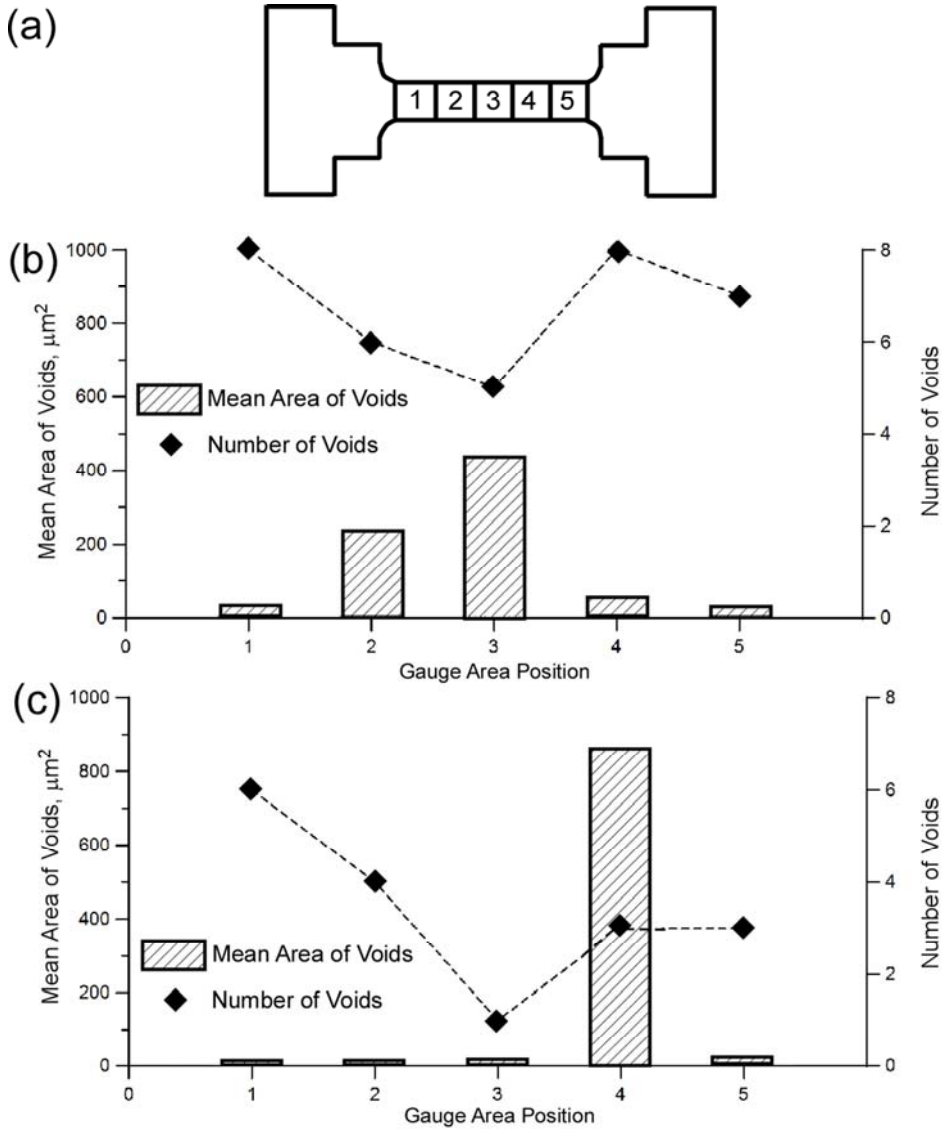

Figure 5.11 Surface voids distribution in the tensile-deformed specimens having bimodal structure: (a) Schematic of measured positions in the gauge area; (b) Harmonic bimodal structure (ε=0.59); (c) Heterogeneous bimodal structure (ε=0.57);

Figure 5.12 shows representative morphology of fracture surfaces of bimodal structured tensile specimens. The presence of a significant amount of cracks (debonding) can be clearly observed in the centre of fracture surface of harmonic bimodal structured specimen in Fig.5.12a. By contrast, more cracks widely distributed

on the fracture surface of heterogeneous bimodal structured specimen. Moreover, the morphology of fracture surface in the bimodal structured compacts was dominated with dimples, Fig.5.12c. In general, two different morphologies were apparent: (i) coarse dimples corresponding to the coarse grains and (ii) finer dimples arose from the fracture of UFG region. In addition, the several cracks formed in the vicinity of CG/UFG interface, as can be seen in Fig.5.12d.

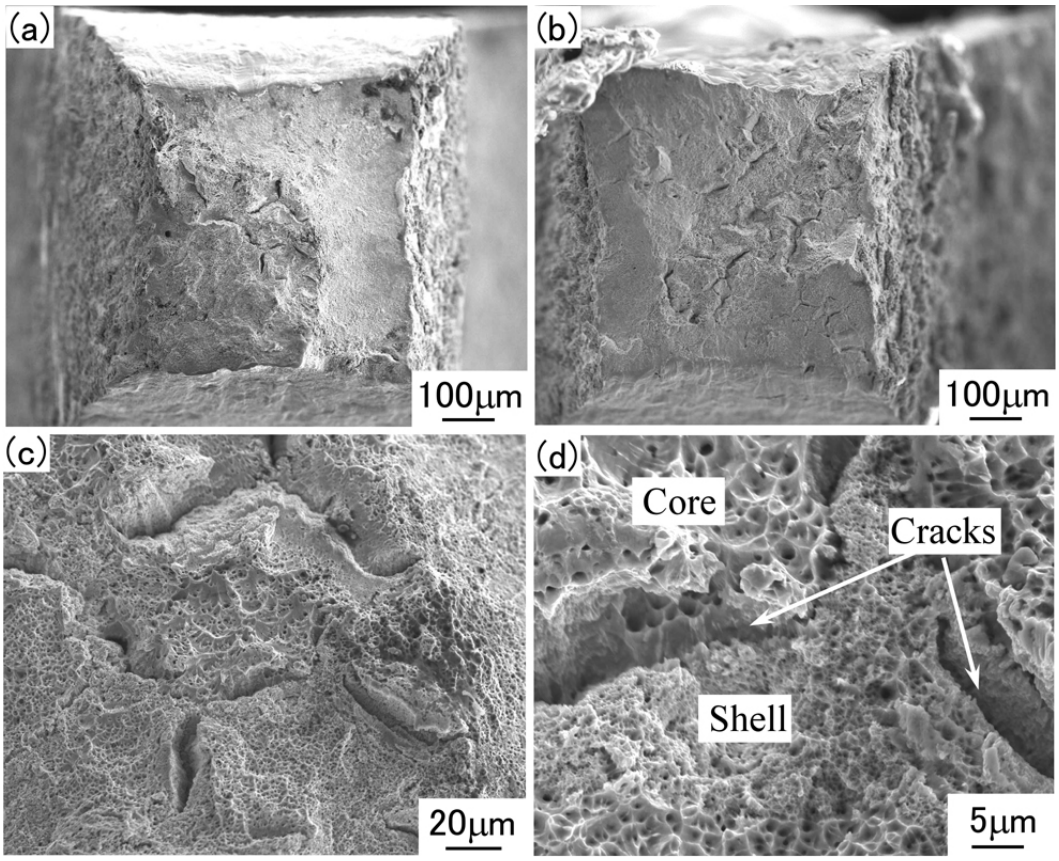

Figure 5.12 Morphology of fracture surfaces of bimodal structured SUS304L specimens: (a) Harmonic bimodal structure; (b) Heterogeneous bimodal structure; (c) Enlargement of cracks in Fig.5.12a; (d) Enlargement of cracks in Fig.5.12c.

5.4 Discussion

5.4.1 Improve Ductility through the Control of Bimodal Structure Heterogeneity and Topology

In the present study, the tensile properties of the bimodal structured SUS304L stainless steels having different spatial distribution of CG and UFG components have been compared. It is found that the harmonic-structured SUS304L steel having a periodic three-dimensional continuous connected network of UFG regions exhibited higher ductility, in particular uniform elongation as compared to the heterogeneous bimodal structured one having irregular CG and UFG spatial locations.

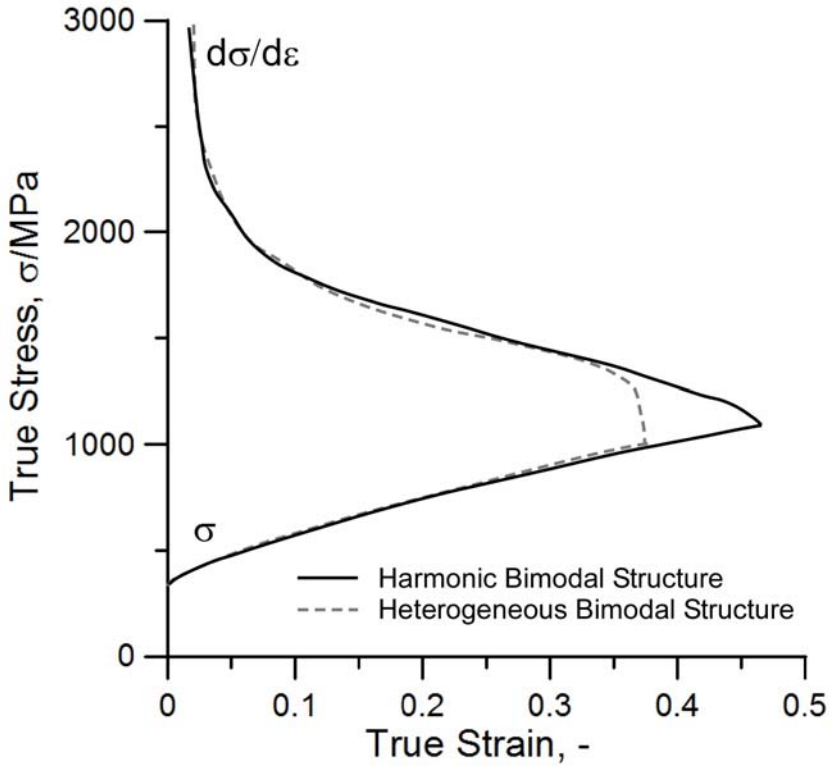

Figure 5.13 True stress-true strain curves and strain hardening rate curves of SUS304L steels having different microstructure.

It is reported that the inadequate ductility of UFG/NC materials is caused by plastic instability condition which is achieved at the early stage of deformation. The main factor to enhance the ductility of bimodal structured materials is to increase the strain hardening and delay the plastic instability. As shown in Fig.5.3, through comparing the tensile deformation of specimens having different bimodal structure heterogeneity and topology, it is concluded that the three-dimension continuous connected network UFG structure is conducive to restraining plastic strain localization during mechanical loading. As remarked in Fig.5.13, the suppressed strain localization leads to postpone the plastic strain instability and delay the neck formation. Therefore, the ductility, in particular uniform elongation in tension of harmonic bimodal structured SUS304L is superior to that of the heterogeneous bimodal structured one. In other words, the ductility of bimodal structured materials can be improved by the control of the bimodal structure heterogeneity and topology (CG and UFG spatial locations). It is proposed that the 3D continuous connected network of UFG structure is benefit for improving ductility, in particular uniform elongation in tension.

Furthermore, since the distribution and spatial locations of CG and UFG areas are regular and periodic in harmonic bimodal structured SUS304L steels, the tensile properties can be reproduced each time. It is thought that the exact distributions of the grain size, grain shape, and spatial locations in bimodal structured materials can be controlled and reproduced by mechanical milling and powder metallurgy methods. Therefore, “harmonic structure design” is proposed to be an effective strategy to reduce the variation of mechanical property and increase the reproducibility of material response.

5.4.2 Deformation Mechanism of Harmonic-structured SUS304L Compacts

Creating a bimodal (or multi-modal) grain size distribution is suggested to be a useful strategy to enhance ductility, wherein UFG matrix in the bimodal microstructure provides the high strength, while the relatively large coarse grains (CG) contribute to the ductility. The deformation mechanism of the harmonic-structured materials having a three-dimensional continuous network of UFG region is demonstrated from Fig.5.4 to Fig.5.8. In the early stage of tensile deformation, the stress concentration is located at UFG/CG boundary owing to the different ductility between CG and UFG components. Next, deformation accumulates mainly in shell (UFG) with increased strain, so harmonic-structured materials displays improved 0.2% proof strength. It is considered that ductile CG regions within the UFG matrix undergo yielding prior to UFG regions during tension. However, after yielding, CG regions plastically deformed without fracture while the UFG matrix carried most of the tensile load elastically. In contrast, UFG regions plastically deformed very briefly after yielding at a higher stress, because dislocation multiplication over short distances is effectively limited under sufficiently high applied stresses. In terms of load transfer, UFG regions sustained most of the applied stress and only a small part of the load is transferred to the softer CG regions. [15]

Then as strain increases, the work-hardening accumulates in the CG regions, which are elongated along tensile direction. However, meanwhile, plastic deformation is limited in ultrafine grains, which cannot be elongated as coarse grains. Therefore, it

thought that occurrence of strain-induced grain rotation happens in the shell region. The network structured shell region is elongated and extruded by the adjacent core regions during deformation, which leads to reduction shell width reduction. Owing to the regular spatial locations of CG and UFG in harmonic bimodal structured materials, the local strain distribute regularly in each shell-and-core unit along gauge area. Therefore, every shell-and-core unit deforms homogenously in a wide range of the specimen during tensile deformation, which is benefit to restrain plastic strain localization.

In view of observations collected, a descriptive model for tensile deformation of harmonic bimodal structured SUS304L stainless steels is proposed, as shown in Fig.5.14a and Fig.5.14b. Firstly, when the stress reaches the yield point of the coarse grains, plastic deformation occurs within these regions. Stress concentrates at the shell/core interface due to the different ductility between shell (UFG) and core (CG). Next, as the stress increases and reaches the yield point of ultrafine grains, which cannot undertake plastic deformation, strain-induced grain rotation occur in the shell and along shell/core interface. Stress concentrates at node of network structured shell and within shell regions. Then, as the tensile strain increases, slip bands form within the cores which also induce stress concentration, while the shell is extruded by the adjacent cores. The shell-and-core network structure is elongated homogeneously and regularly. Stress tends to be undertaken within each shell-and-core unit during tension, which is conducive to restraining plastic strain localization. Therefore, it is concluded that the shell (ultrafine grains) provides strengthening while the core (coarse grains) and the deformation of periodic three-dimension network structured can contribute to the ductility. Overall, each shell-and-core unit plays very important role in the harmonic structure deformation, which is conducive to the restrained plastic strain localization

during mechanical loading. The unique CG and UFG spatial locations (i.e. three-dimensional continuous network structured UFG) contribute to thwarting localization of plastic flow during mechanical loading, which leads to delay the plastic strain instability. Therefore ductility is increased, in particular uniform elongation in tension.

5.4.3 Fracture Mechanism of Harmonic-structured SUS304L Compacts

The knowledge of deformation and fracture mechanism of each component in bulk bimodal microstructure is useful for the concept of this kind of materials. A few of studies have been devoted to the mechanism of deformation and fracture of its two CG and UFG components. However, owing to variety of materials, these studies did not show completely the different deformation mechanism of bimodal structure materials.

In the study of Lee et al. [15, 16], the microstructure, mechanical properties, tensile deformation and fracture mechanism of bimodal structure Al-7.5Mg alloys were investigated. Direct observations in various scale ranges revealed void nucleation and crack behaviour in tensile fracture of bimodal Al-7.5Mg alloys. They remarked that the bimodal grain structures exhibited unusual deformation and fracture mechanisms similar to ductile-phase toughening of brittle materials. Ductile CG regions within the UFG matrix undergo yielding prior to UFG regions during tension. Subsequent to yielding of the UFG matrix, stress concentrations in the UFG regions may be relaxed by void generation and growth and by transferring local loads to the softer CG regions. In

addition, stress mismatch between CG and ultrafine grains also increases with the increase of quasi-static load and leads to initiation of voids at the UFG/CG interface. Subsequently, the CG bands tended to deform locally at stress concentrations, arresting cracks by local blunting, and resisting crack growth by bridging of crack wakes, and impeding crack propagation by deflecting and branching of crack tips and by delamination during plastic deformation.

In the study of Bui [17], the heterogeneous plastic deformation behavior of two bimodal ultrafine-grained Ni materials with different UFG and CG components fractions was investigated experimentally at the grain level. The large localized plastic strain within the coarse grains was observed during compression. The larger strain of the CG grains and the smaller strain of UFG grains may be a result of strain localization during compression. The strain localization results in a possibility of occurrence of debonding and cracks in the UFG region or in the interface between UFG and CG regions.

However, in the present thesis, it is remarkable that approximately 80% voids nucleated in the CG region of bimodal structured SUS304L steels, which indicates that SUS304L steels have its unique void nucleation mechanism. It is well-known that SUS304L steel is a typical metastable austenitic stainless steel. The strain-induced martensite transformation ($\gamma \rightarrow \alpha'$) during tension in SUS304 and SUS304L stainless steel has been reported. [18-20] The formation of deformation-induced martensite is related closely to slip bands. Moreover, it is reported that grain size has also been shown to affect the formation of α', with larger grains leading to higher amounts of α'. [21-23] As shown from Fig.5.7 to Fig.5.9, there are plenty of slip bands occurred in the elongated CG regions of bimodal structured SUS304L steels. Therefore, it is predicted

that many strain-induced martensite formed near the slip bands in the CG regions. It is known that the martensite is harder than austenite, which may be a result of strain localization at the intersection of the pile-up slip bands. The stress concentration may be relaxed by the ultrafine grains rotation in the UFG region and transferring local loads to the softer CG regions near UFG/CG interface in the UFG regions and UFG/CG interface. Therefore, it is predicted that owing to martensite transformation the stress concentration near intersection of the pile-up slip bands in the CG region is higher than that in the UFG region and at the UFG/CG interface, which leads to the occurrence of void nucleation in the CG regions easily. Any heterogeneity in a material that produces a stress concentration can nucleate void. Therefore, it is found that approximately 80% voids nucleated in the CG regions while the other 20% voids nucleated at UFG/CG interface.

As shown in Fig.5.10, owing to the strain localization, the only large crack formed in the neck region of “heterogeneous” structured SUS304L specimen. By contrast, owing to the restrained strain localization induced by the three-dimension continuous network structured UFG regions, more voids were well-distributed in the tensile elongated “harmonic” structured specimen during tensile deformation.

Figure 5.12 shows the morphology of fracture surface of typical bimodal structured SUS304L specimens. It is thought that the larger surface dimples indicate that the core (CG) regions underwent significantly more plastic strain than shell (UFG) regions. It is observed several cracks propagated at the UFG/CG interface perpendicular to the fracture surface. Therefore, it is concluded that owing to the different ductility of UFG and CG regions, the stress concentration at the UFG/CG interface is relaxed by the crack propagation. Moreover, crack propagation tends to stop at UFG/CG interface. In

other words, crack propagation can be apparently restrained by UFG/CG interface. Note also that several cracks between CG and UFG regions perpendicular to the fracture plane are evident. Such crack propagation may contribute to the enhanced ductility in bimodal structured specimen.

Furthermore, it is also clear from Fig. 5.12a that the debonding and cracks is located in the centre of fracture surface of harmonic-structured specimen. By contrast, it is indicated from Fig.5.12b that owing to the high strain localization near the fracture surface, the more well-distributed debonding and cracks can be observed on the fracture surface of heterogeneous bimodal structured specimen. These cracks can coalesce easily during deformation, which results in rapid fracture. Such fewer cracks initiation and coalescence near fracture surface may contribute to the enhanced ductility in harmonic-structured specimen.

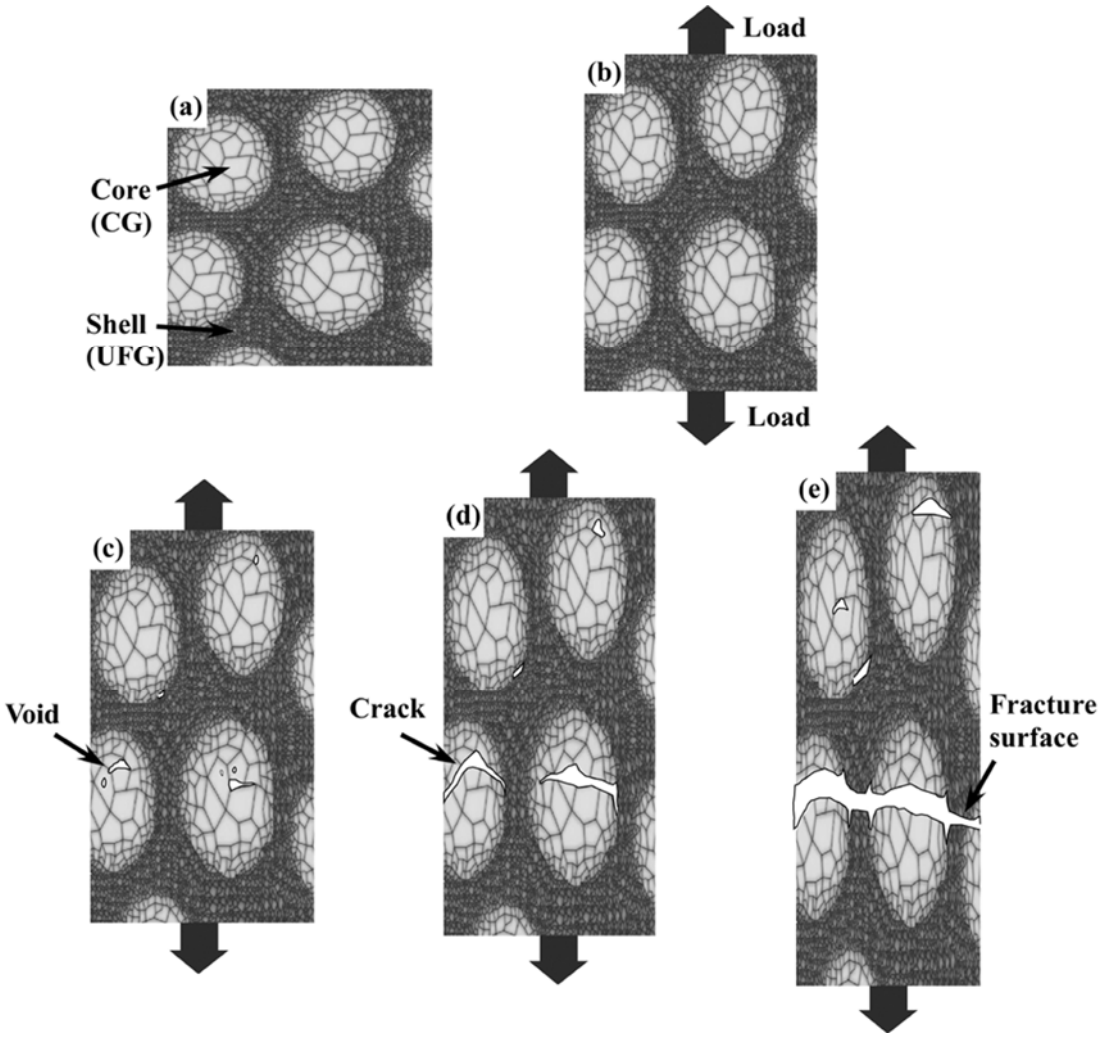

Figure 5.14 Schematic of tensile deformation and fracture mechanism of harmonic bimodal structured SUS304L steels under uniaxial tension: (a) Harmonic bimodal structure, (b) Tensile elongated, (c) Void nucleation, (d) Crack growth, and (e) Fracture.

In view of observations collected, a descriptive model is proposed for tensile fracture of harmonic-structured SUS304L stainless steel. As shown in Fig.5.14, tensile deformation and fracture stage are described by the four steps in the schematic. First, as shown in Fig.5.14b, the network structured shells and cores are elongated homogeneously along the tensile direction. Plastic deformation accumulates within cores, wherein slip bands occur. Second, as the stress increases at the intersection of

pile-up slip bands, most voids nucleate and well distribute within CG regions, as shown in Fig.5.14c. In addition, a part of voids also nucleate at shell/core interfaces owing to the different ductility between shell and core. Third, as the tensile strain increases, the CG regions undergo elongation and voids grow and coalesce to form cracks within the cores and extend transverse to the load axis. However, the cracks tend to propagate along shell/core interface, as shown in Fig.5.14d. Crack propagation is effectively impeded by cores and network structured shell, wherein the crack propagation is blunted by coarse grains and deflection at shell/core interfaces. Finally, fracture ensues when cracks coalescent and the CG regions can no longer sustain the load, as shown in Fig.5.14e. Owing to the restrained strain localization and periodic microstructure, the void nucleation and crack coalescence tend to form in the centre of cross-section of fracture surface, which may also enhance the ductility in harmonic bimodal structured SUS304L stainless steels.

5.5 Conclusions

In this chapter, the commercially supplied PREPed SUS304L powder was mechanical milled and spark plasma sintered to produce the compacts having different bimodal structure heterogeneity and topology. These compacts had similar CG and UFG grain sizes and volume fraction, but different CG and UFG spatial locations. Direct observations in tensile deformation and fracture behaviour in tensile fracture of “harmonic bimodal structured” and “heterogeneous bimodal structured” SUS304L steels were analyzed. Based on this analysis, the following conclusions can be drawn:

(1) The harmonic bimodal structured SUS304L steels, which has a three-dimensional

continuous network structured UFG spatial location, demonstrates winning combination of high strength, large uniform elongation and large total elongation to fracture as compared to the heterogeneous bimodal structured ones having irregular CG and UFG spatial distribution.

(2) Owing to the periodic network structure, “harmonic structure designed” materials can reduce the variation of corresponding mechanical properties therefore increasing the reproducibility of results.

(3) The three-dimensional continuous connected network UFG structure is conducive to restraining plastic strain localization during mechanical loading. The suppressed strain localization leads to postpone the plastic strain instability and delay the neck formation. The ductility of bimodal structured materials can be increased by the control of CG and UFG spatial distribution. It is proposed that the 3D continuous connected network of UFG structure is benefit for improving ductility, in particular uniform elongation in tension.

(4) In bimodal structured SUS304L steels, as the tensile stress increases at the intersection of pile-up slip bands wherein martensite forms, most voids tend to nucleate and well distribute within CG regions. Only a part of voids also nucleate at shell/core interfaces owing to the different ductility between shell and core. Since voids nucleate and grow in the CG regions firstly and deflect at UFG/CG interface, therefore cracks propagation is effectively impeded by CG regions and UFG/CG interface. Such crack propagation may contribute to the enhanced ductility in bimodal structured SUS304L steels.

References

[1] C. Koch, Optimization of strength and ductility in nanocrystalline and ultrafine grained metals, Scripta Materialia, 49 (2003) 657-662.

[2] E. Ma, Instabilities and ductility of nanocrystalline and ultrafine-grained metals, Scripta Materialia, 49 (2003) 663-668.

[3] I. Ovid'ko and T. Langdon, Enhanced ductility of nanocrystalline and ultrafine-grained metals, Reviews on Advanced Materials Science, 30 (2012) 103-111.

[4] Y. Wang, E. Ma, Three strategies to achieve uniform tensile deformation in a nanostructured metal, Acta Materialia, 52 (2004) 1699-1709.

[5] E. Ma, Eight routes to improve the tensile ductility of bulk nanostructured metals and alloys, JOM, 58 (2006) 49-53.

[6] B. Kumar and D. Raabe, Tensile deformation characteristics of bulk ultrafine-grained austenitic stainless steel produced by thermal cycling, Scripta Materialia, 66 (2012) 634-637.

[7] H. Azizi-Alizamini, M. Militzer and W. Poole, A novel technique for developing bimodal grain size distributions in low carbon steels, Scripta Materialia, 57 (2007) 1065-1068.

[8] G. Dirras, J. Gubicza, S. Ramtani, Q. Bui and T. Szilágyi, Microstructure and mechanical characteristics of bulk polycrystalline Ni consolidated from blends of powders with different particle size, Materials Science and Engineering A, 527 (2010) 1206-1214.

[9] B. Srinivasarao, K. Oh-ishi, T. Ohkubo and K. Hono, Bimodally grained high-strength Fe fabricated by mechanical alloying and spark plasma sintering, Acta Materialia, 57 (2009) 3277-3286.

[10] J. Jin and Y. Lee, Strain hardening behavior of a Fe–18Mn–0.6C–1.5Al TWIP steel, Materials Science and Engineering A, 527 (2009) 157-161.

[11] R. Petrov, L. Kestens, A. Wasilkowska and Y. Houbaert, Microstructure and texture of a lightly deformed TRIP-assisted steel characterized by means of the EBSD technique, Materials Science and Engineering A, 447 (2007) 285-297.

[12] M.R. Barnett, M.D. Nave and C.J. Bettles, Deformation Microstructures and Textures of Some Cold Rolled Mg Alloys, Materials Science and Engineering A, 386 (2004) 205-211.

[13] Y. Chen, J. Hjelen and H. J. Roven, Application of EBSD technique to ultrafine grained and nanostructured materials processed by severe plastic deformation: Sample preparation, parameters optimization and analysis", Transaction Nonferrous Metals Society of China, 22 (2012) 1801-1809.

[14] Y. Liu, M. Shazly and J. J. Lewandowski, Microstructural effects on crack path selection in bending and fatigue in a Nb-19Si-5Cr-3.5Hf-24Ti-0.75Sn-1W alloy, Materials Science and Engineering A, 527 (2010) 1489-1500.

[15] Z. Lee, V. Radmilovic, B. Ahn, E. Lavernia, and S. Nutt, Tensile deformation and fracture mechanism of bulk bimodal ultrafine-grained Al-Mg alloy, Metallurgical and Materials Transactions A, 41A (2010) 795-801.

[16] Z. Lee, D. Witkin, V. Radmilovic, E. Lavernia and S. Nutt, Bimodal microstructure and deformation of cryomilled bulk nanocrystalline Al-7.5Mg alloy, Materials Science and Engineering A, 410-411 (2005) 462-467.

[17] Q. Bui, Heterogeneous plastic deformation in bimodal bulk ultrafine-grained nickel, Journal of Materials Science, 47 (2012) 1902-1909.

[18] N. Tsuchida, Y. Morimoto, T. Tonan, Y. Shibata, K. Fukaura and R. Ueji, Stress-induced martensitic transformation behaviors at various temperatures and their TRIP effects in SUS304 metastable austenitic stainless steel, ISIJ International, 51 (2011) 124-129.

[19] J. Choi and W. Jin, Strain induced martensite formation and its effect on strain hardening behavior in the cold drawn 304 austenitic stainless steels, Scripta Materialia, 36 (1997) 99-104.

[20] M. Smaga, F. Walther and D. Eifler, Deformation-induced martensitic transformation in metastable austenitic steels, Materials Science and Engineering A, 483-484 (2008) 394-397.

[21] K. Lo, C. Shek and J. Lai, Recent developments in stainless steels, Materials Science and Engineering R, 65 (2009) 39-104.

[22] S. Varma, J. Kalyanam, L. Murr, S. Srinivas, Effect of grain size on deformation-induced martensite formation in 304 and 316 stainless steels during room temperature tensile testing, Journal of Materials Science Letters, 13 (1994) 107-111.

[23] S. Raman, K. Padmanabhan, Tensile deformation-induced martensitic transformation in AISI 304LN austenitic stainless steel, Journal of Materials Science Letters, 13 (1994) 389-392.

Chapter 6 Effects of SiO_2 Particles on Deformation of SUS304L Powder Compacts with Bimodal Structure

6.1 Introduction

Water atomization is the most commonly-used technique for high-volume, low-cost metal powders production. Therefore, water-atomized metal powders have been widely used in the industry. Thus, “harmonic structure design” is also attempt to apply in SUS304L water-atomized powders compacts in this Chapter. The microstructure evolution and mechanical properties of mechanically milled water-atomized SUS304L powder compacts will be discussed. The deformation and fracture mechanism of the sintered compacts will be also clarified.

6.2 Experimental Procedure

The chemical composition of the water-atomized SUS304L powders used is shown in Table 6.1. The average powder size was approximately 80μm. Mechanical milling was carried out in a Fritsch P-5 planetary ball mill with SUS304 vial and steel balls in argon gas atmosphere at room temperature. 10mm diameter balls were used and the ball-to-powder weight ratio was maintained at 2:1. The powder mixture was milled for

36ks and 108ks at a constant milling speed of 200rpm, respectively. The milled powders were charged into a mild steel capsule and then hot-isostatically pressed, which involved sintering under 200MPa for 14.4ks at 1173K.

Table 6.1 Chemical composition of water-atomized SUS304L powders (mass %).

C	Si	Mn	P	S	Ni	Cr	Fe
0.018	0.9	0.2	0.022	0.003	11.22	18.76	Bal.

The mechanical properties were examined by hardness and tensile tests. The Vickers hardness was measured under a load of 0.98N. The microstructure observations were carried out by optical microscopy (OM), scanning electron microscopy (SEM) with JEOL JSM-6400 operating at 20kV and transmission electron microscopy (TEM) with JEOL JEM-2010 operating at 200kV. The samples were etched by copper sulfate solution for OM and SEM observation. For TEM observation, the samples were machined to ϕ3 and prepared by mechanical grinding to below 200μm thickness. Then specimens were thinned by twin-jet electro-polishing.

Evaluating from SEM and TEM images of compacts with homogenous structure, the diameter of grains and area fraction were defined as grain size and volume fraction, respectively. The specimens for tensile tests were machined by wire-spark cutting to a gauge length of 3mm and a cross-section area of $1\times1mm^2$. Tensile experiments were conducted by a universal testing machine (Autograph AGS-10kND, Shimadzu), under displacement control with nominal strain rate of 5.56×10^{-4}/s (cross-head speed of 0.1mm/min). The fracture surfaces were analyzed by 3-D reconstructions obtained using the MeX software package (Alicona).

6.3 Results and Discussion

6.3.1. Microstructure of the MM-HIP Compacts

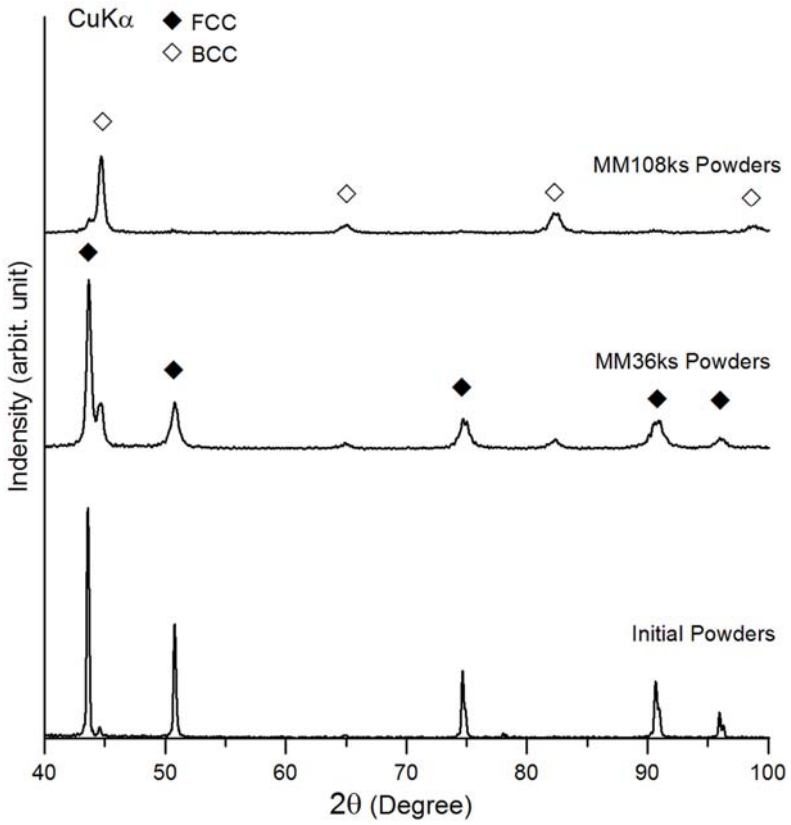

Figure 6.1 XRD results of water-atomized SUS304L powders before and after mechanical milling.

Figure 6.1 shows the XRD results of initial powders (IP) and the milled powders. The IP mainly has an austenite phase (FCC). By contrast, it is noticed that martensite (BCC) was shown in the milled powders. Moreover, as milling time increase from 36ks (MM36ks powders) to 108ks (MM108ks powders), the austenite transforms into martensite gradually. Therefore, it indicates the mechanical milling transformed austenite into martensite near the powder surface. Figure 6.2 shows the morphology of water-atomized SUS304L steel powders before and after the milling. Owing to the high

water pressure, the shape IP powders is irregular. Compared with PREPed powders, the powders were cold-welded after milled for only 36ks. Therefore, it is concluded that the MM process leads to agglomerate easily due to the cold wedding of the irregular-shaped initial water-atomized powder particles.

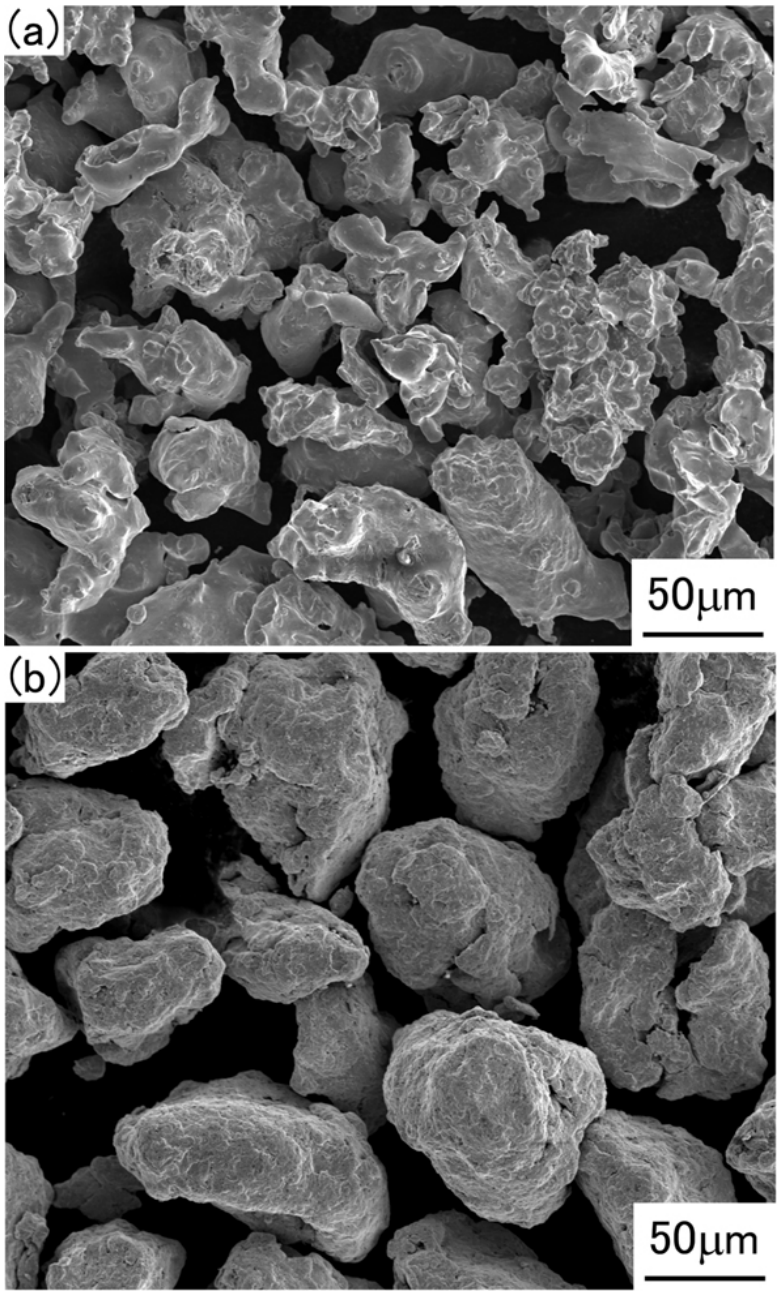

Figure 6.2 Morphology of water-atomized SUS304L initial powders (a) and the powders mechanical milled for 36ks (b).

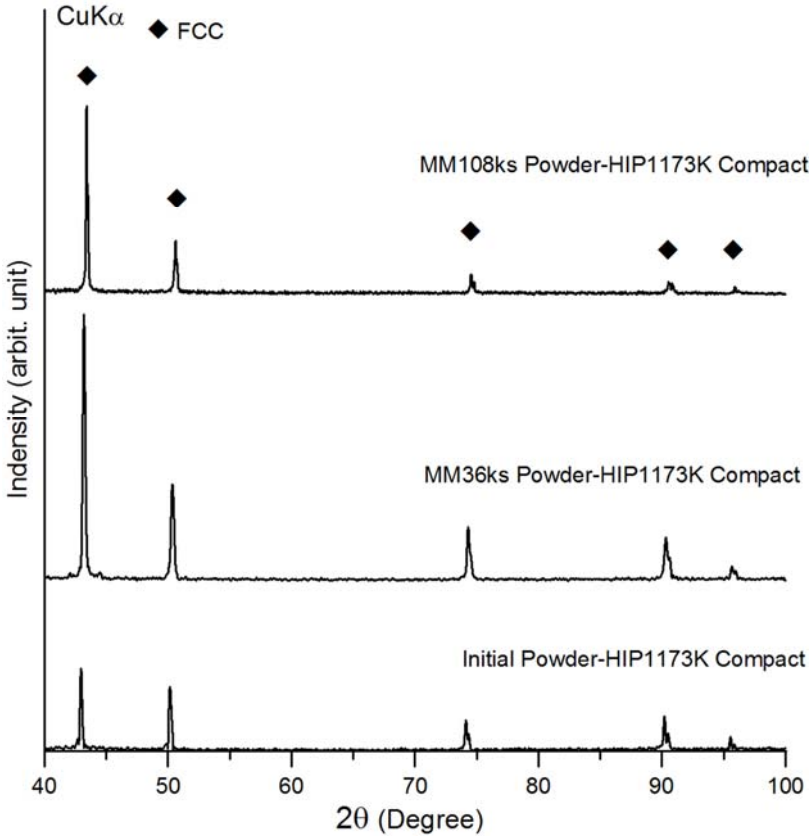

Figure 6.3 XRD results of sintered water-atomized SUS304L powder compacts.

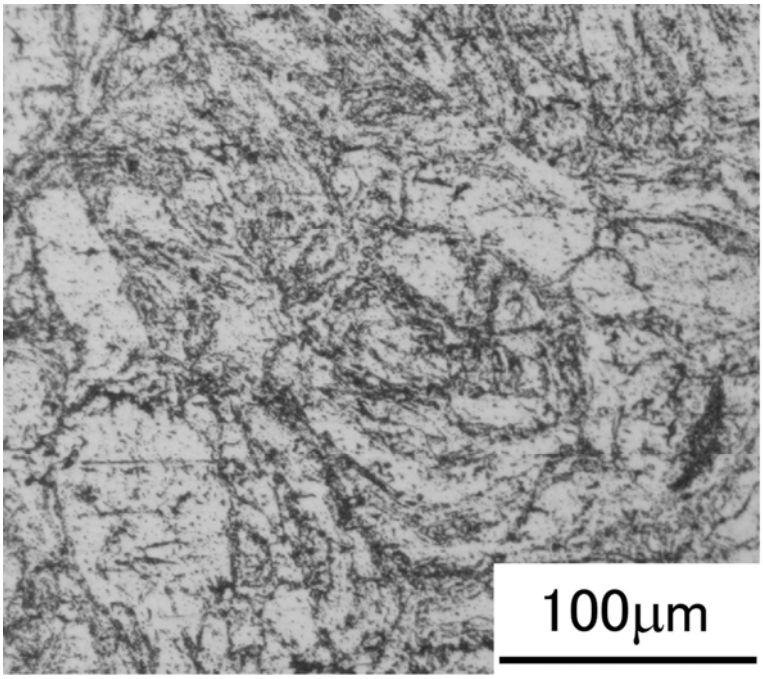

Figure 6.4 OM image of the SUS304L MM36ks-HIP compact microstructure.

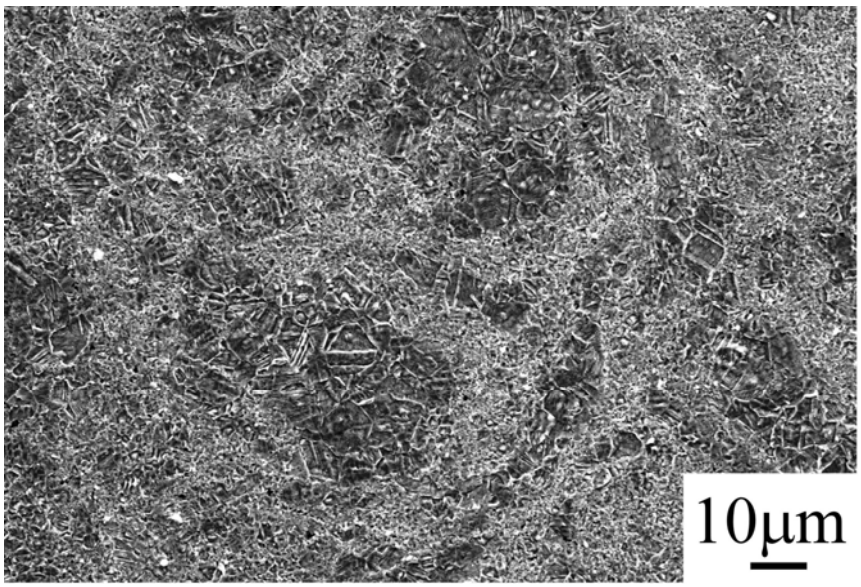

Figure 6.5 SEM image of the SUS304L MM36ks-HIP compact microstructure.

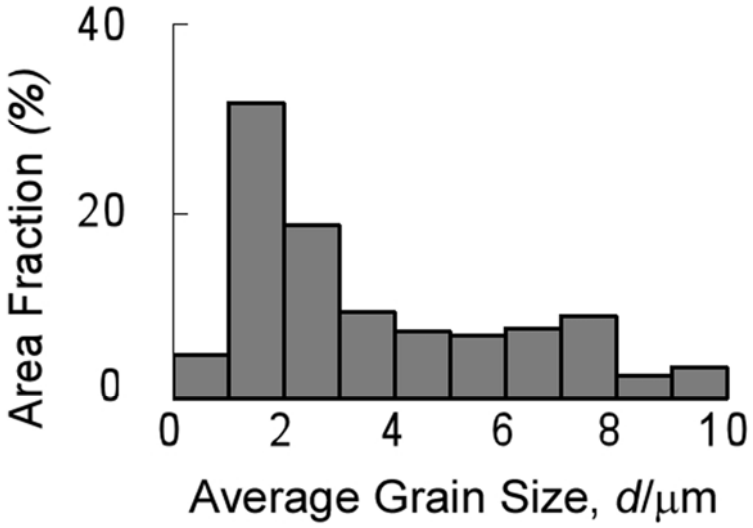

Figure 6.6 Grain size distribution of the SUS304L MM36ks-HIP compact microstructure.

Figure 6.3 shows the XRD results of sintered water-atomized SUS304L powder compacts. Both the IP compacts and milled powder compacts have an austenite phase (FCC), which indicates that martensite near the milled powder surface was reversed into austenite after sintering. Figure 6.4 shows an OM image of the microstructure of SUS304L compact consolidated by HIP from powders milled for 36ks (referred to as

MM36ks-HIP compact). The image shows thin regions with a dark appearance, forming a network which surrounds the brighter regions. This indicates that there are two different kinds of structure present in the sintered compact.

Figure 6.5 shows a SEM microstructure of the same compact, while the grain size distribution is shown in Fig.6.6. This compact indicates two different microstructures: coarse-grained (CG) regions and ultrafine-grained (UFG) regions. A bimodal structure can be observed in the sintered compact. The average grain size in the coarse-grained regions is about 7.7μm. The fractions of the coarse-grained and ultrafine-grained components are 68% and 32%, respectively. Therefore, it is concluded that the martensite transformation caused by mechanical milling and subsequent austenite reversion during sintering induce the ultrafine grains.

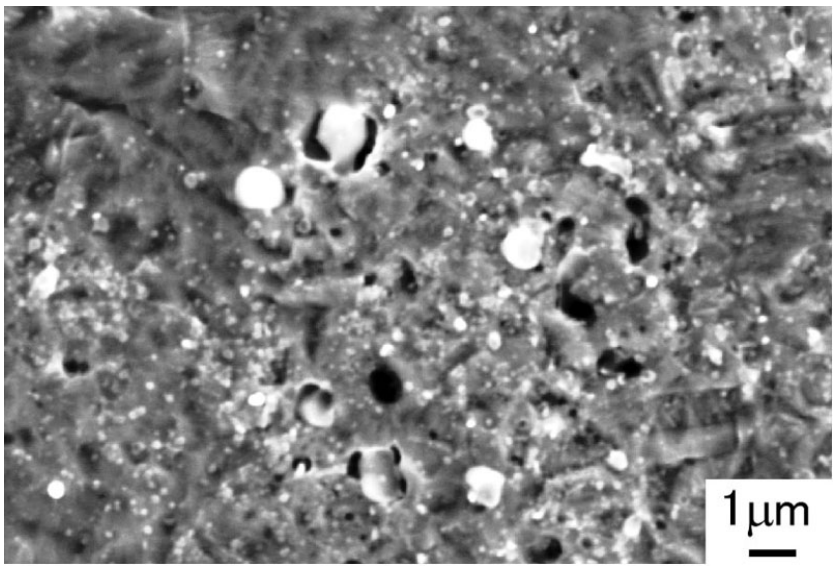

Figure 6.7 Particles disperse in ultrafine-grained region of MM36ks-HIP compact.

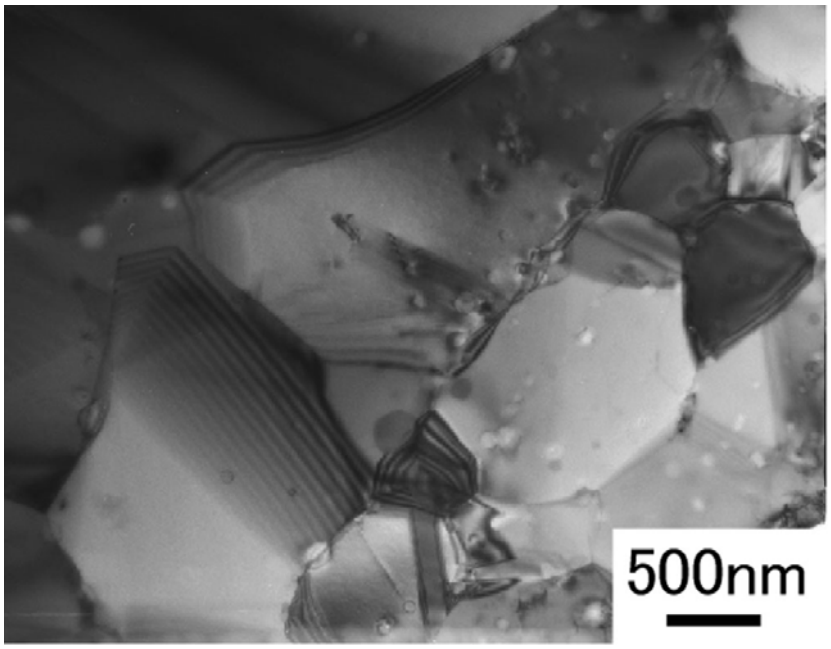

Figure 6.8 TEM image of the ultrafine-grained region in SUS304L MM36ks-HIP compact microstructure.

As shown in Fig.6.7, many particles disperse uniformly in the UFG region and at the ultrafine-grained region/coarse-grained region (UFG/CG) interface. The size ranges from 100nm to 1μm. A TEM study was also carried out for a better evaluation of the particle dispersion. The typical aspect of ultrafine-grained regions is shown in Fig.6.8. The ultrafine grain size varies from 300nm to 1μm, and many particles disperse in the UFG region and at the UFG/CG interface. The chemical composition and structure of the particles were studied by TEM-EDS and the results are presented in Fig.6.9. Fig.6.9a shows a particle in the ultrafine-grained region of sintered SUS304L. The EDS map in Fig.6.9b shows that Si and O are present in the particle. This suggests that the particle consists of silicon oxide. The electron diffraction pattern is shown in Fig.6.9c, and the halo pattern indicates that the particle consists of amorphous silica.

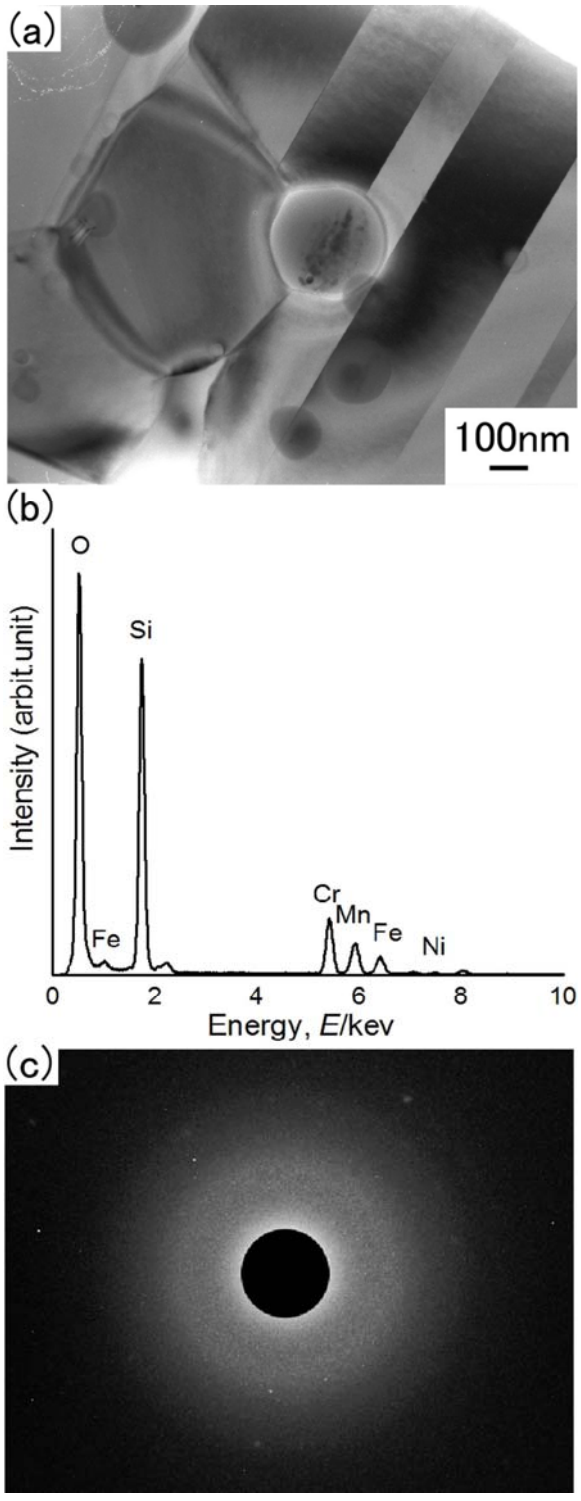

Figure 6.9 TEM-EDS analysis of particles in ultrafine-grained region.

(a) TEM image of particle; (b) Chemical compositions;

(c) Corresponding diffraction pattern. (Spot of the direct beam in the SADP has been masked)

Water atomization is the most commonly used technique for high-volume, low-cost metal powder production. During the powders fabrication, when the metal comes into contact with water, it reacts in accordance with:

$$xMe + yH_2O \rightarrow Me_xO_y + yH_2 \quad 6.1$$

The metal becomes partly oxidized, even though the atomizing tank has been purged with an inert gas to minimize oxidation of the powder. Silicon, with its greater affinity for oxygen than chromium and its high mobility in the liquid state, migrates to the surface of the liquid particle during water atomization, in preference of other constituents and despite its small concentration in the alloy. In essence, the critical role of silicon during water atomization and sintering is similar to what happens at a somewhat higher temperature in conventional stainless steel technology. The main difference between wrought and powder metallurgy (PM) stainless steel is that, in the former, the undesirable silicon dioxide is removed by the slag, whereas in PM it remains in the product unless it is removed or reduced during sintering. The phenomenon of preferred silicon oxidation has major implications because of the high affinity of silicon to oxygen and the difficult reduction, even in a matrix of stainless steel, of silicon oxides during sintering. The silicon oxide forms a continuous layer at 1393K, and it subsequently breaks up into particles as the temperature is raised up to 1523K. [1-4]

After sintering of the milled water-atomized SUS304L powders under 200MPa at 1173K, silicon oxide particles disperse uniformly in the UFG region and at the UFG/CG interface of the bimodal structure. It is therefore important to improve the knowledge of the effects of silicon oxide particles on deformation and fracture behavior of the compact with bimodal structure.

6.3.2 Deformation and Fracture of the MM-HIP Compacts

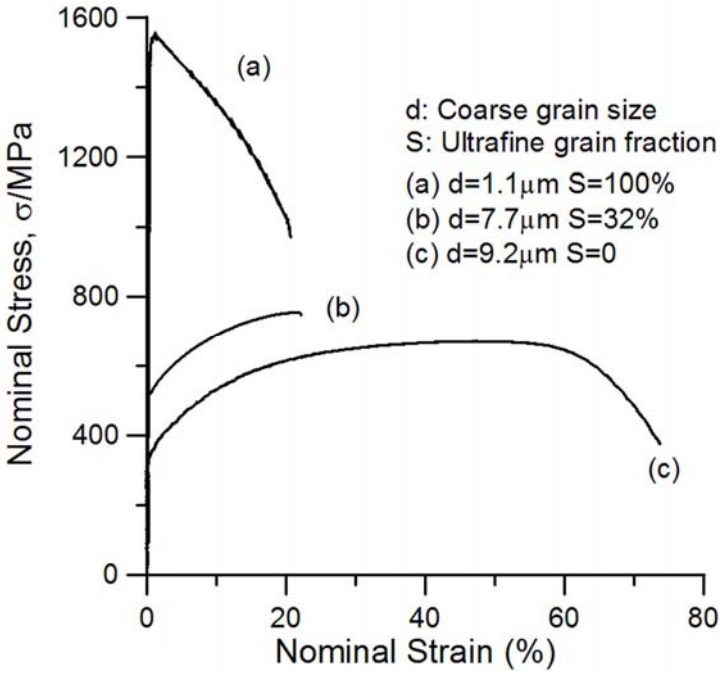

Figure 6.10 Nominal stress-nominal strain curves of SUS304L specimens.

(a) Bulk (ultrafine-grained structure); (b) MM36ks-HIP compact (bimodal structure with silicon oxide particles); (c) Bulk (coarse-grained structure).

Nominal stress–nominal strain curves of SUS304L obtained from tensile tests are shown in Fig.6.10. Specimen (b) is the result of the MM36ks-HIP compact, while specimens (a) and (c) are the result of bulk with average grain size of 1.1μm and 9.2μm, respectively. The MM36ks-HIP specimen is the bimodal structure compact with silicon oxide particles, and exhibits a 0.2% proof stress of 510MPa, tensile strength of 754MPa, uniform elongation of 20% and total elongation of 22%. It is found that the compact with bimodal structure demonstrates relatively higher strength (especially yield strength) than the conventional coarse-grained bulk with similar coarse grain size, but work-hardening of these two specimens is similar in the early stage. It suggests the

ultrafine-grained regions improve the strength of compact with bimodal structure. As grain size decreases, the elongation decreases also, especially the uniform plastic deformation. The total elongation of bimodal structure specimens with silicon oxide is identical to that of bulk with ultrafine-grained structure, but the uniform elongation is close to total elongation.

One of the reasons for the limited ductility and particularly the low uniform elongation in UFG metals is their propensity for plastic instability (inhomogeneous deformation such as necking in tension, and shear banding) in the early stage of plastic straining. UFG metals become unstable during tensile deformation due to their diminished strain hardening capacity and the inadequate strain hardening rate observed for these materials. The simplest equation for plastic instability condition of strain-rate insensitive materials is defined as,

$$\sigma \geq d\sigma/d\varepsilon \qquad 6.2$$

where σ is the flow stress (true stress) and $d\sigma/d\varepsilon$ is the strain hardening rate. The position where the two curves (flow stress σ and strain hardening rate $d\sigma/d\varepsilon$) meet is the point of plastic instability. It is assumed that the strain-hardening rate does not change even if the materials strengthened.

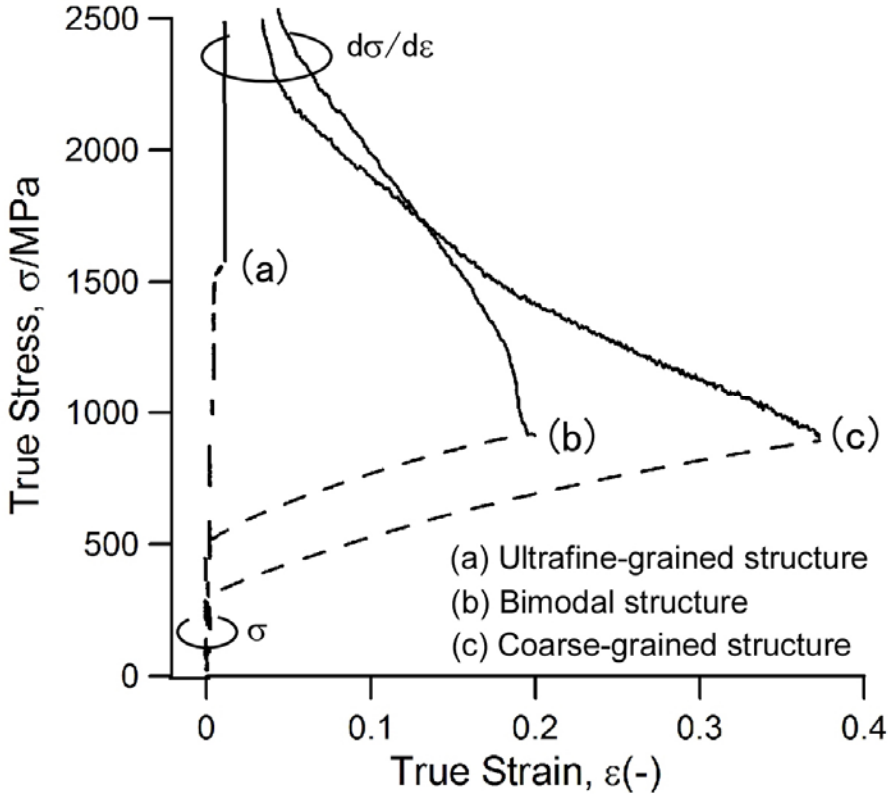

Figure 6.11 True stress-true strain curves (broken line) and strain hardening rate curves (solid line) of SUS304L compacts having different structure.

To reveal the deformation behavior of bimodal structure material, the strain hardening rates of bimodal structure material, CG material and UFG material have been analyzed. Fig.6.11 shows true stresses-true strain curves (broken lines) and strain hardening rate curves (solid lines) of SUS304L having different structure. The positions where the two curves meet correspond to the plastic instability condition. The strain hardening rate of CG material shows a gentle slope, and the angle of intersection between the true stress and strain hardening rate curves is small. On the contrary, the strain hardening rate of UFG material shows a steep slope, and the angle of intersection is large. Therefore, for UFG material, the plastic instability condition is achieved in the earlier stages of tensile deformation, which results in limited uniform elongation. The bimodal structure material exhibits a gentle slope for the strain hardening rate curve in the early stage of

tensile deformation, which suggests that the work-hardening and uniform elongation are provided by the coarse-grained structure. However, it is interesting that the strain hardening rate curve becomes steep near the intersection, which is similar to the case of the FG structure. It seems that the elongation of the bimodal structure specimen is insufficient and the specimen fractures prematurely during tensile deformation. [5-7]

Additionally, the hardness of the coarse-grained and ultrafine-grained components is 238HV and 285HV, respectively. The average hardness of bimodal structure compact is 258HV, while the hardness of bulk with uniform coarse-grained structure is 189HV. This suggests that the ultrafine-grained regions can improve the hardness of materials with bimodal structure.

Limited elongation and fracture without necking have been observed in the fractured bimodal structure compact with silicon oxide particles. Several tensile specimens are used to illustrate the fracture behavior.

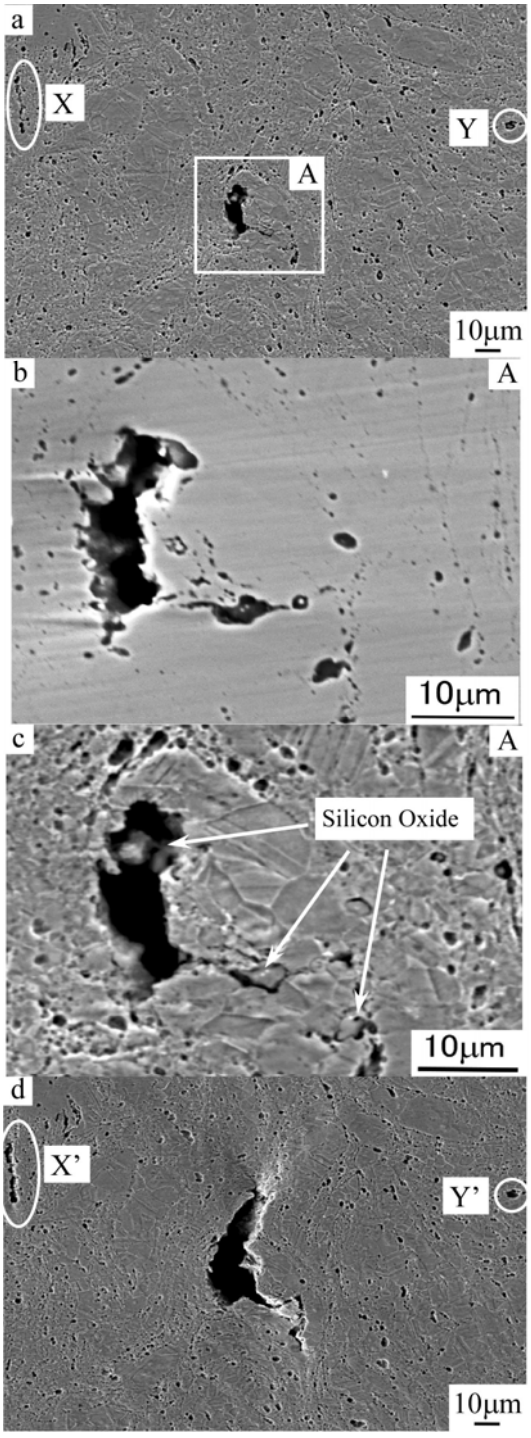

Figure 6.12 Observation of crack propagation in a specimen with bimodal structure.

(The tensile direction is horizontal)

(a) Cracks in stretched specimen (ε=0.2); (b) Large magnification of large crack before etching; (c) Large magnification of large crack after etching; (d) Propagation of the same cracks (ε=0.22).

To get a better understanding of the void nucleation and crack propagation, surfaces perpendicular to the fracture surface were analyzed. Crack propagation in a bimodal structure specimen with silicon oxide particles is revealed in Fig.6.12. Fig.6.12a shows a large crack form in the specimen tensile-stressed to 20% elongation. Fig.6.12b and Fig.6.12c show a large magnification of this crack before and after chemical etching. It appears from Fig.6.12c that cracks form at the UFG/CG interface, where many silicon oxide particles appear. This suggests that silicon oxide particles left in the sintered compact hinder inter-particle bonding, as reflected by the void nucleation. Due to different ductility of UFG and CG regions, the cracks propagate at the UFG/CG interface more easily than in the center of the UFG region for the bimodal structure, although many silicon particles also form there. The crack propagation is possibly impeded by the work-hardening of the coarse-grained structure during the deformation. Next, this specimen was elongated to fracture, and the same crack is shown in Fig.6.12d. It is seen that this crack propagates along UFG/CG interface. Furthermore, there are also many voids nucleated near the silicon oxide particles in stretched specimen, such as the two places with different strains marked by X, Y and X', Y', respectively. Compared with the propagation of the large crack, the remarkable propagation of these voids could not be observed.

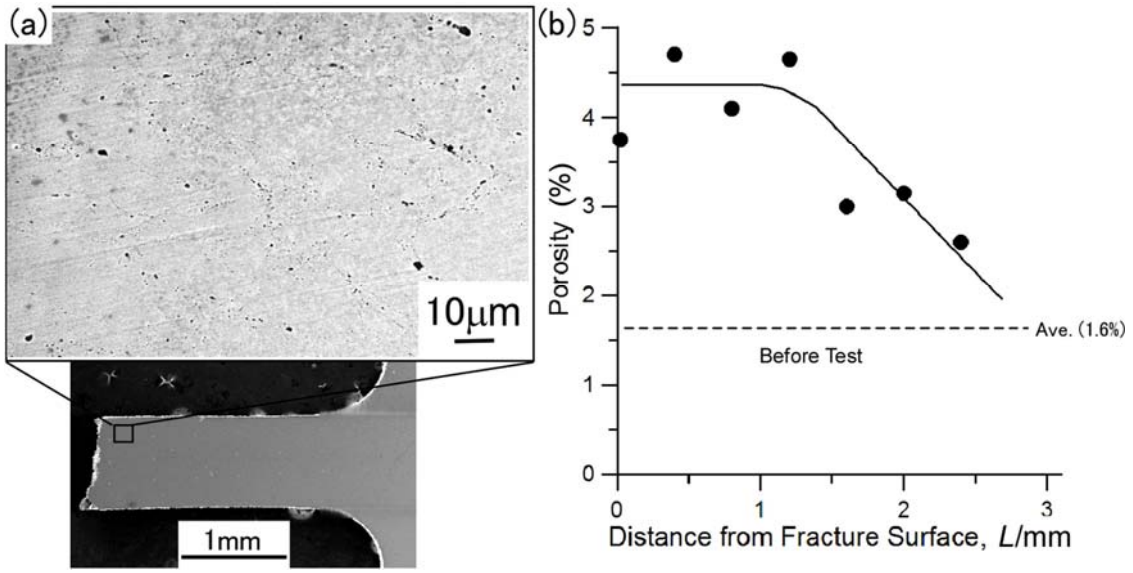

Figure 6.13 Porosity of fractured SUS304L MM36ks-HIP specimen.

(a) Surface perpendicular to the fracture surface; (b) Change of porosity through the gauge area.

Figure 6.13a shows the surface of fractured bimodal structure specimen with silicon oxide particles. It is found that many voids exist in the fractured compacts. It is interesting to note that when the compact fractures, no neck area can be observed near the fracture surface. As shown in Fig.6.14b, the open porosity of the fractured specimen is about 4.5% in the region 1.2mm away from the fracture surface, and it decreases toward the gauge ends.

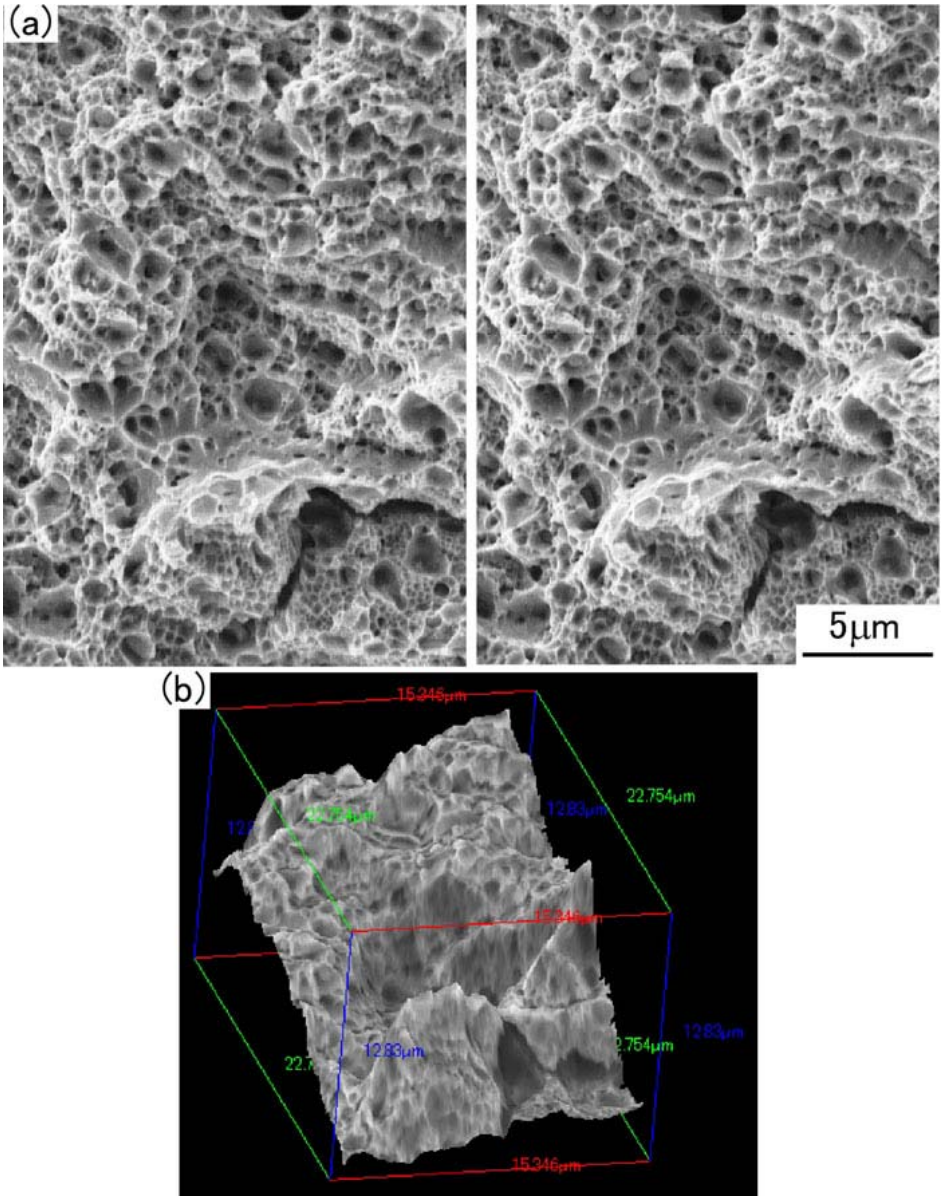

Figure 6.14 Fracture surface of fractured SUS304L MM36ks-HIP specimen.

(a) A pair of stereo micrograph; (b) 3-D reconstruction of the fracture surface.

Figure 6.14a and Figure 6.14b shows a pair of stereo micrographs and a 3-D reconstruction of the fracture surface. The fracture surface is covered by small dimples, indicating a ductile failure mechanism, and the dimple size ranges from 1μm to 3μm.

Silicon oxide particles impairing inter-particle bonding lead to void nucleation near the particles. In the early stage, cracks form at the UFG/CG interface near formed

silicon oxide particles, and many voids distribute uniformly through the gauge area. Next, as deformation continues, the voids expand and advance in a plane close to normal to the tensile direction. The majority of the cracks stop at the UFG/CG interface, but some travel through a minor fraction of the adjacent coarse-grained region. Finally, as several adjacent cracks in the central region of specimen become interconnected, sudden fracture occurs. The lack of an observable neck at the macro level, in spite of a ductile failure mechanism, can be explained by the high density of void nucleation sites represented by the silicon oxide particles. The gauge cross-section area decreases abruptly due to the simultaneous expansion of many voids within a very limited region; this sudden increase in stress cannot be accommodated and leads to failure. Due to the very small amount of elongation from strain localization to failure, a typical neck cannot be observed.

In order to obtain enhanced mechanical properties, the surface silicon oxide particles should be reduced. Sintering in hydrogen and under vacuum with additions of graphite to the powder is an effective way to reduce the surface oxides. Removal of surface oxides should lead to improved inter-particle bonding, which would be reflected in markedly improved dynamic mechanical properties (elongation, impact strength). [4]

6.4 Conclusions

Water-atomized SUS304L powders were mechanical milled, and then MM powders were consolidated by HIP. The microstructure and mechanical properties were analyzed. The following conclusions can be drawn:

(1) Owing to the irregular powder shape, a bimodal structure, including

coarse-grained region and ultrafine-grained region, can be obtained in SUS304L compacts consolidated by MM-HIP process. Martensite transformation and subsequent austenite reversion induces ultrafine grains formation. The ultrafine-grained regions improve the strength and hardness while the coarse-grained regions provide work-hardening to maintain uniform plastic deformation.

(2) Silicon oxide particles are dispersed uniformly on inter-particle boundaries and in ultrafine-grained regions. The silicon oxide particles formed appear as amorphous silica.

(3) Silicon oxide particles lead to impaired inter-particle bonding, as reflected in markedly worsened elongation. To obtain the expected enhancement in mechanical properties, the surface silicon oxide must be reduced.

(4) The propagation of voids is limited by coarse-grained regions in the early stage of tensile deformation, which results in the improvement of ductility during mechanical loading.

References

[1] L. Nyborg, T. Tunberg and P. Wang, Surface product formation during water atomization and sintering of austenitic stainless steel powder, Metal Powder Report, 45 (1990) 750-753.

[2] L. Nyborg and T. Tunberg, Surface reactions during water atomisation and sintering of austenitic stainless steel powder, Powder Metallurgy, 38 (1995), 120-130.

[3] H. Karlsson, L. Nyborg and S. Berg, Surface chemical analysis of prealloyed water

atomised steel powder, Powder Metallurgy, 48 (2005), 51-58.

[4] E. Klar and P. Samal, *Powder metallurgy stainless steels: Processing, microstructures, and properties*, ASM International, Materials Park OH, 2007, 23-38.

[5] Y. Wang and E. Ma, Strain hardening, strain rate sensitivity, and ductility of nanostructured metals, Materials Science and Engineering A, 375-377 (2004) 46-52.

[6] N. Hansen, X. Huang, R. Ueji and N. Tsuji, Structure and strength after large strain deformation, Materials Science and Engineering A, 387-389 (2004) 191-194.

[7] N. Tsuji, N. Kamikawa, R. Ueji, N. Takata, H. Koyama and D. Terada, Managing both strength and ductility in ultrafine grained steels, ISIJ Int. 48 (2008) 1114-1121.

Chapter 7 Conclusions and Future Work

7.1 Overall Conclusions

This dissertation describes the work that has been carried out to obtain a better understanding of the manufacture, mechanical properties, deformation and fracture mechanism of “harmonic structure designed” austenitic stainless steel. The main emphasis of thesis is to fabricate the SUS304L stainless steel having “harmonic structure”, clarify its mechanical properties and understand the role of the three-dimensional continuous network of UFG structure in improving the ductility, in particular uniform elongation in tension. The harmonic-structured SUS304L steels were synthesized by mechanical milling and subsequent spark plasma sintering. The mechanical properties were studied under uniaxial tension and Vicker’s hardness. The deformation and fracture mechanism of harmonic-structured SUS304L steels were revealed qualitatively using SEM, EBSD and TEM in various scale ranges. Detailed conclusions were provided at the end of each chapter, so this section provides overall conclusions from this work.

Plasma rotating electrode process (PREP) steel powders characterized by high purity, spherical particle shape and lower oxygen content are applied to synthesize the harmonic-structured stainless steel. There is a two-step process to synthesize harmonic-structured materials. Firstly, mechanical milling is applied to fabricate the powders having a heterogeneous shell-and-core bimodal structure. Martensite

transformation and subsequent austenite reversion plays an important role on grain refinement in the sintered compacts. The thickness of "shell area" in milled powders, and hence the fraction of UFG structure, is controlled by such parameters of mechanical milling as (i) ball diameter (and hence weight), (ii) ball to powder ratio, (iii) milling time, and (iv) milling speed, temperature and atmosphere. Appropriate selection of these parameters allows to control the process of mechanical milling precisely, and to produce the required gradient of microstructure in the processed powder particles.

Subsequently, a technique and parameters for the sintering of MM powders should be tailored to ensure appropriate compaction and then inter-particle bonding, while minimizing the processes of grain growth in the shell area. These can usually be achieved through the utilization of high hydrostatic pressure, fast heating/cooling rates, and high temperature applied for a short time. A technique perfectly satisfying all these criteria is spark plasma sintering, and therefore it was used in the present investigation. Hot-roll sintering is also an excellent technique for this purpose since in addition to hydrostatic pressure; it imparts shear deformation thus accelerating inter-particle bonding. In both these techniques, the control of holding temperature and time allows to adjust the balance of core/shell fractions, and to minimize the level of residual porosity.

Table 7.1 Quantitative characteristics of mechanical properties of SUS304L steel after different kinds of thermo-mechanical processing.

No.	Processing**	Structure	$\sigma_{0.2}$* [MPa]	σ_{UTS}* [MPa]	ε_u* [%]	ε_t* [%]	Average grain size [μm], (fraction %)	
							bulk or core	shell
1	MM180ks+ SPS1173K	Harmonic bimodal	328	690	61.8	80.1	16.8 (79%)	2.0 (21%)
2	MM360ks+ SPS1173K	Harmonic bimodal	382	744	65.6	80.3	17.6 (59%)	1.5 (41%)
3	IP+MM360ks (1:1)+ SPS1173K	Heterogeneous bimodal	340	694	46.3	56.9	18.4 (80.4%)	1.5 (19.6%)
4	Bulk	Homogeneous CG	250	601	79.4	94.3	35.0 (100%)	---
5	IP+ SPS1173K	Homogeneous CG	260	516	44.6	48.4	19.7 (100%)	---
6	ECAP at 1073K	Homogeneous UFG	580	710	30.0	37.0	0.2-1.0 (100%)	---
7	ECAP at 973K	Homogeneous UFG	1013	1094	3.0	12.0	0.2-0.5 (100%)	---
8	Thermal cycling at 1173-1223K	Homogeneous UFG	902	1082	5.0	16.0	0.2-0.5 (100%)	---

*$\sigma_{0.2}$ stands for 0.2% proof stress; σ_{UTS} for ultimate tensile stress; ε_u for uniform elongation; and ε_t for total elongation.

**MM means mechanical milling of SUS304L powder; IP means initial powders; SPS-spark plasma sintering; and ECAP- equal channel angular pressing.

As summarized in Table 7.1, the harmonic-structured SUS304L steel demonstrates a superior combination of high strength, large uniform elongation, and large total elongation. Compared to the conventional CG products with a homogeneous grain size of ~35μm, the harmonic-structured one possesses slightly inferior ductility, but nearly

30% higher 0.2% proof and ultimate tensile strengths. However, the ductility characteristics of UFG SUS304L steels were so low (the uniform and total elongations down to 3% and 12%, respectively) that further processing as well as potential applications of such materials were largely compromised. Even compacted with conventional bimodal structured SUS304L steels having similar grain sizes and UFG fraction but irregular CG and UFG distribution, the harmonic-structured ones also exceed these ductility characteristics by far (68% and 80%, respectively).

The harmonic-structured SUS304L steels exhibits higher ductility, in particular uniform elongation as compared to the heterogeneous bimodal structured one having irregular CG and UFG spatial distribution. Through comparing the tensile deformation of specimens having different bimodal structure heterogeneity and topology, it is concluded that the three-dimensional continuous connected network of UFG structure is conducive to restraining plastic strain localization during mechanical loading. The suppressed plastic stain localization leads to postpone the plastic strain instability and delay the neck formation. Therefore, the ductility, in particular uniform elongation in tension of harmonic-structured SUS304L steel is superior to that of the heterogeneous bimodal structured one. In other words, the ductility of bimodal structured materials can be improved by the control of CG and UFG spatial locations. The 3D continuous connected network of UFG structure is proposed to be benefit for improving ductility, in particular uniform elongation in tension.

Owing to the periodic and regular distribution of CG and UFG, the mechanical properties of harmonic-structured SUS304L steels exhibit good reproducibility. The exact distributions of the grain size, grain shape, and spatial locations in bimodal structured materials can be controlled and reproduced by the mechanical milling and

powder metallurgy methods. Therefore, “harmonic structure design” is proposed to be an effective strategy to reduce variation of mechanical properties and increase reproducibility of materials response.

Furthermore, there are also some advantages of this manufacture process. Firstly, the selected powder metallurgy based approach for the fabrication of harmonic-structured materials allows the consolidation of mechanically milled powders into final products. This may further reduce the cost of industrial manufacturing processes based on this approach, which makes the proposed concept of material design even more attractive for commercial applications. Moreover, since any other element does not need to enhance the mechanical properties of materials, therefore the composition of harmonic structure designed materials is simple and easy to be recycled.

Based on the microstructure evolution and deformation behavior of water-atomized SUS304L powder compacts produced by the same method, it is considered that although the water-atomized powders have high volume production at low cost, it is difficult to control the UFG and CG distribution in milled powders and sintered compacts due to their irregular powder shape. Moreover, chemical compositions of stainless steel powder are complicate, and the oxygen content near the water-atomized powders in relative high, oxidation contaminations tend to precipitate and they are difficult to remove during powder metallurgy process. Removal of surface oxides should lead to improved inter-particle bonding, which would be reflected in markedly improved dynamic mechanical properties (elongation, impact strength).

7.2 Further work

The concept of "harmonic structure design" has been successfully applied in a variety of metals and metallic alloys. However, there is no investigation of the parameters of harmonic structure that ensure such a mechanical behavior. The microstructural evolution and mechanical properties of bimodal structured SUS304L stainless steels (representative FCC stainless steel) have been discussed. The optimum fabrication conditions and characteristics of bimodal structured materials would be suggested by comparing with other representative metals and alloys.

The knowledge of deformation and fracture mechanism of each component in bulk bimodal microstructure is useful for the concept of this kind of materials. However, in the aforementioned contents, only a few studies were devoted to the deformation and fracture mechanism of bimodal structured materials. Compared with these studies, the bimodal structured SUS304L steels have shown some different deformation mechanism of the two CG and UFG components. Therefore, it would be necessary to investigate the deformation and fracture mechanism of other bimodal structured materials. Moreover, in this thesis, the deformation and fracture behaviour of bimodal structured SUS304L stainless steels with unique grain size and volume fraction have been discussed. It would be of interest to investigate the effects of grain size and fraction of CG and UFG components on deformation and fracture mechanism. The deformation of CG and UFG grains would be observed using TEM under microscale observation.

In this thesis, the tensile deformation of bimodal structured SUS304L steels has been studied under quasistatic loading at room temperature. To reveal the deformation mechanisms in bimodal structured, in particular harmonic-structured metals, the effects

of temperature and strain rate on the flow behavior are proposed to study.

In order to expand the application of harmonic-structured materials in industries, the fatigue, creep and corrosion properties would be studied in the future.

Appendix

Curriculum Vita

Born in March 19, 1983, Shaanxi, China

Education:

1998-2001 High School of Caihong (Xianyang City, Shannxi Province, China) Secondary School Student

2001-2005 School of Chemical Engineering and Technology, Tianjin University, (Tianjin, China) Bachelor Degree of Engineering

2005-2007 Graduate School of Chemical Engineering and Technology, Tianjin University, (Tianjin, China) Master Degree of Engineering

2007-2009 Graduate School of Science and Engineering, Ritsumeikan University, (Kyoto, Japan) Master Degree of Engineering

2010-2014 Graduate School of Science and Engineering, Ritsumeikan University, (Kyoto, Japan) Doctor Degree of Engineering

Work Experience:

2009-2014 Research and Development Center, Dainippon Screen MFG Co. Ltd., (Kyoto, Japan)

Publications during Doctoral Course

Awards:

[1] Kei Ameyama, Hiroshi Fujiwara, Tatsuya Sekiguchi, **Zhe Zhang**, "A Novel Powder Metallurgy Processing Approach by Harmonic Structure Design", 38th Japan Society of Powder and Powder Metallurgy Award for Innovatory Research 2013, 2014.5

[2] **Zhe Zhang,** Dmitry Orlov, Sanjay Kumar Vajpai, Bo Tong, Kei Ameyama, "Improvement of ductility through the control of bimodal structure heterogeneity and topology", the Best Poster Award for 2nd International Symposium: Funtionalization and Applications of Soft/Hard Materials (Soft/Hard2013), Ritsumeikan University, 2013. 11.

Journal papers:

[1] **Z. Zhang**, SK. Vajpai, D. Orlov, K. Ameyama, Improvement of mechanical properties in SUS304L steel through the control of bimodal microstructure characteristics, Materials Science and Engineering A, 598 (2014) 106-113.

[2] **Z. Zhang**, M. Rifai, H. Kobayakawa, OP. Ciuca, H. Fujiwara, A. Ueno, K. Ameyama, Effects of SiO2 particles on deformation of mechanically milled water-atomized SUS304L powder compacts, Materials Transactions 53 (2012) 109-115.

[3] A Ueno, H Fujiwara, M Rifai, **Z. Zhang**, K Ameyama, Fractographical analysis on fracture mechanism of stainless steel having harmonic microstructure, Journal of the Society of Materials Science, Japan 61 (2012) 686-691.

[4] K Ameyama, T Sekiguchi, H Fujiwara, **Z. Zhang**, Microstructure and mechanical properties of hetero-structure metallic materials produced by harmonic structure design, Tetsu to Hagane-ISIJ 98 (2012) 739-744.

Conference papers:

[1] **Zhe ZHANG**, Bo Tong, Octav Paul Ciuca and Kei Ameyama, Microstructure and deformation mechanism of SUS304L compacts with harmonic structure, JSPM, Ritsumeikan university, 2012.11

[2] Bo Tong，**Zhe ZHANG** and Kei AMEYAMA, SPD-PM プロセスによる SUS304L ステンレス鋼のヘテロ組織制御と力学特性，ISIJ，Kanazawa university，2013.9

[3] Bo Tong，**Zhe ZHANG**，Octav Paul CIUCA and Kei AMEYAMA, SUS304L における調和組織制御および力学的特性，材料開発研究会，関西大学千里山キャンパス，2012.12

[4] Muhammad Rifai, **Zhe Zhang**, Hideyuki Tanaka, Hiroshi Fujiwara and Kei Ameyama, Tensile deformation and fracture behavior of SUS316L and SUS304L austenitic stainless steel compacts with harmonic microstructure, ISIJ, 2011.3